Membrane-type acoustic metamaterials for aircraft noise shields

Vom Promotionsausschuss der
Technischen Universität Hamburg
zur Erlangung des akademischen Grades
Doktor-Ingenieur (Dr.-Ing.)
genehmigte Dissertation

von
Felix Langfeldt
aus Bad Segeberg

2018

urn:nbn:de:gbv:830-88223132
https://doi.org/10.15480/882.1780

1. Gutachter: Prof. Dr.-Ing. Otto von Estorff
2. Gutachter: Prof. Dr.-Ing. Wolfgang Gleine

Tag der mündlichen Prüfung: 5. Juli 2018

Für Winnifred.

Acknowledgments

This research has been funded by the Federal Ministry for Economic Affairs and Energy, under the framework of the LuFo IV-4 project Comfortable Cabin for Low-Emission Aircraft (COCLEA), and Airbus S.A.S. Their financial support is gratefully acknowledged.

Furthermore, many helping hands assisted me along my way to finishing this dissertation: I would like to thank my advisor Prof. Gleine from the Hamburg University of Applied Sciences for his commitment, the stimulating discussions, and the guidance when things did not turn out as expected. Also, I am grateful to Prof. von Estorff for giving me the opportunity to do my Ph.D. at the Technical University in Hamburg. The noise shield demonstrator measurements were supported by the acoustics division of Airbus in Hamburg. In particular, I would like to thank Henning Scheel and Martin Wandel for their continuous support of my research.

Also, I want to acknowledge my colleagues and students who assisted me in preparing and conducting the experiments. I am especially grateful to the employees of the Leichtbaulabor, Bernd Schröder, Daniel Sadra, Marcel Opitz, and Matthias Fehling for their assistance. Additionally, I thank Florian Albrecht, Hannah Hoppen, and Hannes Kemsies for their effort and time they put into proofreading my thesis.

My deepest and utmost gratitude, however, goes out to my family. I am indefinitely grateful to my wife Winnifred for her unconditional love, support, and patience – and for our son Otto, one of the greatest gifts in life. Without you, I would have never accomplished this!

Abstract

The reduction of low-frequency noise transmission is a challenging task, especially when mass and size of suitable noise reduction measures are highly constrained. The recently emerged so-called acoustic metamaterials, however, have the potential to provide a solution for this difficulty. This work investigates the applicability of membrane-type acoustic metamaterials (MAMs) in an aircraft noise shield design for the reduction of low-frequency tonal cabin noise generated by counter-rotating open rotor engines. MAMs are thin and lightweight structures which exhibit excellent low-frequency noise reduction properties that cannot be achieved by conventional partitions with equivalent mass. Previous analytical and experimental investigations of MAMs have mostly been performed under greatly simplified conditions, such as normal incidence or small-scale dimensions. Since these conditions are rarely found in practice, the acoustic performance of MAMs needs to be evaluated in more realistic environments.

In this work, computationally efficient analytical models for the prediction of the acoustical properties of MAM unit cells, multi-celled MAM arrays, and multi-layered structures containing MAMs under oblique plane wave excitation are developed. These models are verified and validated using numerical simulations and experiments, respectively. Parameter studies are performed to identify the most important parameters for the design of an aircraft noise shield with MAMs. These results are used in the design of a realistically sized experimental MAM noise shield model attached to an acoustic fuselage demonstrator. This

demonstrator represents a full-scale single aisle aircraft type fuselage section in a rather simplified construction that can be acoustically excited by a loudspeaker array generating realistic engine sound fields.

The analytical results show that the acoustic performance of MAMs under non-orthogonal incidence and within finite-sized multi-celled arrays is not significantly altered as long as the MAM unit cell is smaller than the acoustic wavelength. Furthermore, it is shown that the low-frequency sound transmission through multi-layered structures (e.g. double walls) can be greatly enhanced by integrating MAM layers inside the air gaps. Finally, the noise shield demonstrator measurement results confirm the basic effectiveness of MAMs even in a much more complex and realistic environment. However, these results also reveal that the performance of the MAMs inside the noise shield is greatly affected by airborne flanking sound paths and the spatial characteristics of the excitation sound field.

Contents

Nomenclature

Symbol	Description	Unit
A	Equivalent absorption surface	m^2
$\mathbf{A}$, $\mathbf{B}$	Coefficient matrices	–
$\widetilde{\mathbf{A}}$	Transformed coefficient matrix	–
B	Bending stiffness	N m
$\mathbf{C}$	Membrane stiffness matrix	–
$\widetilde{\mathbf{C}}$	Complex membrane stiffness matrix	–
D	Diameter	m
$\mathbf{D}$	Dynamic stiffness matrix	$\mathrm{N/m}^3$
E	Young's modulus	Pa
$G(x)$	Green's function	$1/[x]$
H	Height	m
I	Number of matching points	–
$I_{mnm'n'}^{(pqp'q')}$	Quadruple integral value	–
$\mathbf{I}$	Identity matrix	–
J	Principal moment of inertia	$\mathrm{kg\ m}^2$
K	Bulk modulus	Pa
$\mathbf{K}$	Modal wave number matrix	–
L	Unit cell edge length	m
L_P	Sound pressure level	dB
L_W	Sound power level	dB
$\mathbf{L}$	Membrane-mass coupling matrix	–
M	Mass	kg

Symbol	Description	Unit
$\bar{\mathbf{M}}$	Effective surface mass density matrix	–
N	Number of membrane eigenmodes	–
N_C	Number of MAM unit cells	–
N_lay	Number of layers	–
N_M	Number of masses	–
$\hat{N}$	Number of eigenmodes	–
$N^{(\varphi)}$	Number of fluid eigenmodes	–
NR	Noise reduction	dB
$\mathcal{N}$	Random number from the standard normal distribution	–
P	Acoustic pressure	$\mathrm{N/m^2}$
$\hat{P}$	Acoustic pressure amplitude	$\mathrm{N/m^2}$
$\mathbf{P}$	Rosenbrock system matrix	–
$\hat{\mathbf{P}}$	Modal Rosenbrock system matrix	–
$\mathbf{Q}$	Mass kinetics matrix	–
R	Distance parameter	m
$\mathbf{R}$	Fluid-structure coupling matrix	–
S	Surface	$\mathrm{m^2}$
$\boldsymbol{\mathcal{S}}$, $\widetilde{\boldsymbol{\mathcal{S}}}$	Transformation matrices	–
T	Prestress resultant	N/m
T_{11}	$(1,1)$-element of transfer matrix	–
T_{12}	$(1,2)$-element of transfer matrix	$\mathrm{Pa\ s/m^3}$
T_{21}	$(2,1)$-element of transfer matrix	$\mathrm{m^3/(Pa\ s)}$
T_{22}	$(2,2)$-element of transfer matrix	–
TL	Transmission loss	dB
$\mathbf{T}$	Transfer matrix	–
$\boldsymbol{\mathcal{U}}$, $\boldsymbol{\mathcal{V}}$	Left- and right-singular vectors matrix	–
V	Volume	$\mathrm{m^3}$
$\mathbf{V}$	Eigenvectors matrix	–

Symbol	Description	Unit
$\hat{\mathbf{V}}$	Reduced eigenvectors matrix	–
W	Sound power	W
$\widetilde{\mathbf{W}}$	Transformed eigenvectors matrix	–
Y	Dimensionless flanking parameter	–
Z	Impedance	Pa s/m^3
$\mathcal{Z}$	Dimensionless impedance	–
a_{rs}	Fluid mode amplitude	–
$\mathbf{a}$	Fluid mode amplitudes vector	–
$\bar{b}$	Surface averaged excitation field	–
b_{mn}	Membrane mode excitation vector elements	–
$\mathbf{b}$	Membrane mode excitation vector	–
$\hat{\mathbf{b}}$	MAM mode excitation vector	–
c	Phase velocity	m/s
c_{mn}	Membrane modal participation factor	–
$\hat{c}_i$	MAM modal participation factor	–
c''	Surface stiffness	N/m^3
$\mathbf{c}$	Membrane modal participation factor vector	–
$\hat{\mathbf{c}}$	MAM modal participation factor vector	–
$\widetilde{\mathbf{c}}$	Normalized membrane modal participation factor vector	–
$\widetilde{\hat{\mathbf{c}}}$	Normalized MAM modal participation factor vector	–
d	Spacing	m
f	Frequency	Hz
f_0	Mass-air-mass resonance frequency	Hz
f_1, f_2, ...	Resonance frequencies	Hz
$f_{\mathrm{P}1}$, $f_{\mathrm{P}2}$, ...	Anti-resonance frequencies	Hz

Symbol	**Description**	**Unit**
$\hat{f}$	Matching point force amplitude	N
$\hat{f}''$	Internal stress amplitude	$\mathrm{N/m^2}$
h	Thickness	m
i	Imaginary unit ($\mathrm{i} = \sqrt{-1}$)	–
i	Mass index	–
j, j'	Matching point indices	–
k	Wave number	rad/m
$\mathbf{k}$	Wave vector	rad/m
l_{mnij}	Membrane-mass coupling matrix elements	–
m, n, m', n'	Membrane mode indices	–
m''	Surface mass density	$\mathrm{kg/m^2}$
p, q	Unit cell indices	–
r_{mnrs}	Fluid-structure coupling matrix elements	–
r, s, r', s'	Fluid mode indices	–
$\tilde{r}$	Reflection factor	–
$\mathbf{r}_{rs}$	Column vector of $\mathbf{R}$-matrix	–
s	Microphone spacing	m
$s_{mm'}(\tilde{u})$	Spatial convolution function	–
t	Time	s
$\tilde{t}$	Transmission factor	–
u	Dimensionless displacement amplitude	–
$\bar{u}$	Dimensionless piston displacement amplitude	–
$\tilde{u}$, $\tilde{v}$	Auxiliary integration coordinates	–
$\mathbf{u}$	Dimensionless displacement vector	–
$\bar{\mathbf{u}}$	Dimensionless piston displacement vector	–
$\tilde{\bar{\mathbf{u}}}$	Normalized piston displacement vector	–
$\hat{v}$	Velocity amplitude	m/s
$\mathbf{v}$	Eigenvector	–

Symbol	Description	Unit
$\widetilde{\mathbf{v}}$, $\widetilde{\mathbf{w}}$	Transformed eigenvectors	–
w	Transversal displacement	m
$\hat{w}$	Transversal displacement amplitude	m
x, y, z	Cartesian coordinates	m
x', y', z'	Cartesian mass coordinates	m
x^*, y^*, z^*	Mass center of gravity coordinates	m
x^*_{pq}, y^*_{pq}	Local MAM unit cell coordinate system origin coordinates	m
$\tilde{x}_{pq}$, $\tilde{y}_{pq}$	Cartesian local MAM unit cell coordinates	m
$\mathbf{x}$	Vector of unknowns	–
$\mathbf{y}$	Right hand side vector	–

Greek letters

$\mathit{\Gamma}$	Attenuation coefficient	rad/m
$\mathit{\Gamma}(x)$	Dimensionless Green's function	–
$\mathit{\Delta}$	Dimensionless distance parameter	–
$\bar{\mathit{\Delta}}_{pqp'q'}$	Dimensionless distance between unit cells	–
Δ	Difference	–
$\Delta\tau$	Dimensionless prestress spread	–
$\mathbf{\Delta\beta}$	Dimensionless pressure difference vector	–
$\mathbf{\Delta\hat{\beta}}$	Modal pressure difference vector	–
$\mathit{\Lambda}$	Unit cell aspect ratio	–
$\mathbf{\Lambda}$	Eigenvalues matrix	–
$\mathbf{\hat{\Lambda}}$	Reduced eigenvalues matrix	–
$\mathit{\Xi}$	Dimensionless bending stiffness	–
$\bar{\mathit{\Xi}}_{pqp'q'}$	Elementary radiation impedance	–
$\mathbf{\Xi}$	Dimensionless radiation impedance matrix	–
$\bar{\mathbf{\Xi}}$	Elementary radiation impedance matrix	–
$\hat{\mathbf{\Xi}}$	Modal radiation impedance matrix	–

Symbol	Description	Unit
$\mathit{\Pi}$	Dimensionless sound power	–
$\boldsymbol{\Sigma}$	Singular values matrix	–
$\mathit{\Phi}_{mn}$	Membrane eigenfunction	–
$\mathit{\Phi}_{mn}^{(ij)}$	Membrane eigenfunction value at matching point location	–
$\mathit{\Psi}_{rs}$	Lateral fluid eigenfunction	–
$\mathit{\Omega}$	Dimensionless frequency	–
$\mathit{\Omega}_1$, $\mathit{\Omega}_2$, ...	Dimensionless resonance frequencies	–
$\mathit{\Omega}_{\mathrm{P}1}$, $\mathit{\Omega}_{\mathrm{P}2}$, ...	Dimensionless anti-resonance frequencies	–
α	Normalized rotational amplitude	°
$\hat{\alpha}$	Rotational amplitude	°
β	Dimensionless pressure amplitude	–
$\bar{\beta}$	Surface averaged dimensionless pressure amplitude	–
β_{mn}	Dimensionless pressure vector elements	–
$\boldsymbol{\beta}$	Dimensionless pressure vector	–
γ	Dimensionless matching point force amplitude	–
γ''	Dimensionless stress amplitude	–
$\boldsymbol{\gamma}$	Dimensionless matching point force vector	–
δ	Dimensionless diameter	–
$\delta(x)$	Dirac delta function	$1/[x]$
ϵ	Eccentricity parameter	–
ε_{pq}	MAM unit cell phase lag	–
$\boldsymbol{\varepsilon}$	MAM unit cell phase lag vector	–
η_{m}	Membrane loss factor	–
θ	Inclination angle	°
θ'	Mass coordinate system orientation angle	°
ϑ	Dimensionless squared radius of gyration	–

Symbol	**Description**	**Unit**
κ	Dimensionless wave number	–
$\kappa_{rsr's'}$	Modal wave number matrix elements	–
$\varkappa_{mn}$	Dimensionless squared membrane eigenfrequencies	–
$\varkappa_{mnm'n'}$	Membrane stiffness matrix elements	–
$\widetilde{\varkappa}_{mn}$	Dimensionless squared membrane eigenfrequencies (without bending stiffness)	–
λ	Wavelength	m
μ	Dimensionless mass	–
μ''	Dimensionless surface mass density	–
ν	Poisson's ratio	–
ξ, η, ζ	Dimensionless Cartesian coordinates	–
ξ_{ij}, η_{ij}	Dimensionless matching point coordinates	–
ξ', η', ζ'	Dimensionless Cartesian mass coordinates	–
ξ^*, η^*, ζ^*	Dimensionless mass center of gravity coordinates	–
$\tilde{\xi}_{pq}$, $\tilde{\eta}_{pq}$	Dimensionless Cartesian local MAM unit cell coordinates	–
ρ	Density	$\mathrm{kg/m^3}$
σ	Specific flow resistivity	$\mathrm{N\,s/m^4}$
σ_τ	Dimensionless prestress standard deviation	–
ς	Dimensionless speed of sound	–
τ	Sound power transmission coefficient	–
τ_{pq}	Dimensionless MAM unit cell prestress resultant	–
ϕ	Azimuth angle	°
ϕ^*	Mass center of gravity polar angle	°
φ	Dimensionless acoustic potential	–
χ	Porosity	–

Symbol	Description	Unit
ψ	Area fraction	–
ω	Angular frequency	rad/s

Subscripts and superscripts

$+$	Transmission side of MAM
$-$	Source side of MAM
$\star$	Convolution coordinate
0	Equilibrium value
0°	Normal incidence
B	Bloch wave
F	Fluid
G	Grid
L	Left side
M	Mass
MAM	Membrane-type acoustic metamaterial
O	Origin
P	Peak
R	Right side
W	Wall
bl	Blocked field
cabin	Cabin
cover	Cover sheet
cr	Critical value
dev	Deviation part
eff	Effective quantity
el	Finite element
eq	Equivalent fluid properties
exc	Excitation
fsl	Fuselage

Symbol	Description	Unit
g	Global system of equations	
high	High value	
i	Incident	
i0	Incident plane wave amplitude	
ix, iy, ix	Cartesian components of incident wave	
limp	Limp porous material	
low	Low value	
m	Membrane	
max	Maximum value	
min	Minimum value	
rad	Acoustic radiation part	
ref	Reference quantity	
rr	Reradiated field	
rubber	Rubber	
shield	Noise shield	
st	Static value	
t	Transmitted	
tot	Total value	
tube	Impedance tube	
vac	In vacuo part	

Miscellaneous

∇^2	Laplace operator
∇^4	Biharmonic operator ($\nabla^4 = \nabla^2\nabla^2$)
$\langle f \rangle$	Spatial average of function f
$\langle f, g \rangle$	L^2-inner product of functions f and g
z^*	Complex conjugate of z
$\mathbf{A}/\mathbf{B}$	Schur complement of the block $\mathbf{B}$ in $\mathbf{A}$
$\mathrm{Re}\{\dots\}$	Real part

Symbol	Description	Unit
diag	Diagonal matrix	
rank	Matrix rank	
sgn	Sign function	

1. Introduction

1.1. Background and motivation

Low-frequency noise is a growing problem in many current transportation technologies. For example, this is the case for aircraft with *counter-rotating open rotor* (CROR) engines, which have been investigated since the 1960s. These engines promise substantial fuel-savings compared to today's turbofan engines while nearly maintaining usual cruise flight speeds achieved with jet engines [26]. The high fuel-efficiency, however, is opposed by the noise from the propellers: Contrary to the relatively broadband noise emitted by turbofan engines, CROR engines exhibit totally different noise characteristics dominated by low-frequency tonal components at the propeller blade passing frequencies (BPFs) and their harmonics. The fundamental BPFs, depending on the rotational speed and the number of propeller blades, typically occur at frequencies around 100 Hz with peak sound pressure levels at the fuselage surface of up to 140 dB [86]. At such low frequencies, the noise reduction along the fuselage side wall – without any specific low-frequency noise treatment – is low and therefore the passengers and crew inside the aircraft cabin are exposed to unacceptably high cabin sound pressure levels. For example, the cabin sound pressure levels within the Tupolev Tu-114 – one of the first commercial airliner powered by CROR engines and still the fastest propeller-driven aircraft in the world – could reach values up to 112 dB [101], which is much larger than today's health and cabin comfort requirements would allow.

Another example for low-frequency noise problems are modern launch vehicles, such as the Falcon 9 by SpaceX, where the payload has to endure sound pressure levels inside the payload fairing of over 120 dB at 160 Hz during the launch sequence [85]. Hence, fragile parts of satellites or other payloads need to be protected from large amplitude acoustic pressure waves to avoid damage.

Both examples require low-frequency noise protection measures with minimal structural mass in order to optimize the efficiency of the system and thus reduce operational cost. There exists a wide range of well-established treatments to reduce noise in the mid- and high-frequency range ($f > 400 \ldots 500$ Hz), where speech intelligibility is an important factor [14]. Low-frequency noise transmission, however, is typically addressed in architectural acoustics using walls and floors with increased mass or stiffness [50]. This approach is infeasible in technological applications where the structural mass of a system is highly constrained. Thus, there is a growing need in the transportation industry for innovative noise protection measures with low structural mass and high acoustic efficiency in the low-frequency regime.

1.2. State of the art

This section provides a brief overview of current technologies for the control of low-frequency noise. In the first subsection, conventional noise protection measures known from architectural and vehicle acoustics are presented and the acoustical performance of these technologies in the low-frequency regime is discussed. The second subsection gives a short introduction into the newly emerged field of acoustic metamaterials and their particular acoustic properties. In the third subsection, recent advances in the development of a specific type of acoustic metamaterial with enhanced efficiency in the low-frequency regime, the so-called *membrane-type acoustic metamaterial*, are presented.

1.2.1. General noise protection measures

To reduce the transmission of sound along an airborne sound path between a noise source and a receiver, structural sound barriers – or partitions – are commonly installed between the source and the receiver [6]. An example is shown in Fig. 1.1 for an aircraft with CROR engines mounted at the rear end of the fuselage. In order to reduce the amount of noise impinging the fuselage, a noise shield acting as a sound barrier can be installed near the engines. The purpose is to block a significant amount of sound energy and thus reduce the noise transmitted into the cabin via the fuselage. In general, the sound power transmitted through a partition is attenuated by a combination of three different physical mechanisms [79]: (1) partial reflection of the incoming sound waves due to sudden changes of acoustic impedance across the partition, (2) absorption of acoustic energy by the dissipative conversion of kinetic energy into heat inside the partition, and (3) redirection of sound as structure-borne sound into flanking parts. In many cases, the latter sound reduction mechanism is undesired, since the redirected structure-borne sound waves can radiate sound at different locations (e.g. into the aircraft cabin in Fig. 1.1). Hence, most noise barrier technologies rely on a combination of sound reflection and absorption [22].

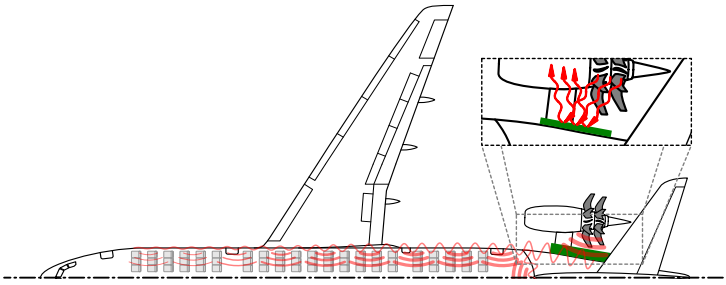

Figure 1.1: Noise shield for an aircraft with CROR engines.

1. Introduction

The sound reduction of a partition is quantified by the *sound power transmission coefficient* τ. In general, τ is a frequency dependent quantity and defined as the ratio of the transmitted sound power W_t to the incident sound power W_i [22]:

$$\tau = \frac{W_\mathrm{t}}{W_\mathrm{i}}. \tag{1.1}$$

Commonly, the sound power transmission coefficient is represented in logarithmic form as the so-called *transmission loss* TL, given by

$$\mathrm{TL} = -10 \lg \tau \tag{1.2}$$

in dB. Apart from the frequency, the sound transmission through a partition also depends on other properties of the incident sound field, e.g. if it is characterized by a single normally or obliquely incident plane wave, a diffuse sound field, or a field incidence sound field [6].

The simplest type of partition is a single homogeneous wall. Assuming a limp unbounded wall (i.e. bending stiffness, boundary conditions, and low-order eigenmodes of the wall are neglected) and the same fluid on both sides of the wall, the normal incidence sound transmission coefficient τ is given by [6]

$$\tau = \left| 1 + \frac{\mathrm{i}\omega m''}{2\rho_0 c_0} \right|^{-2}, \tag{1.3}$$

where $\mathrm{i} = \sqrt{-1}$, $\omega = 2\pi f$ is the angular frequency, m'' is the surface mass density of the wall, and ρ_0 and c_0 are the mass density and the speed of sound of the surrounding fluid, respectively. Consequently, the normal incidence sound transmission loss of the wall is

$$\mathrm{TL} = 20 \lg \left| 1 + \frac{\mathrm{i}\omega m''}{2\rho_0 c_0} \right|, \tag{1.4}$$

which is commonly known as the *mass-law* transmission loss. From Eq. (1.4) it is evident that for a single wall partition with $\omega m'' \gg 2\rho_0 c_0$ the transmission loss increases by 6 dB per doubling of frequency or surface mass density. Consequently, mass-law dominated partitions must be rather heavy in order to provide a reasonable sound reduction in the low-frequency regime.

A common method for increasing the sound transmission loss of a partition is to use a so-called double wall arrangement, as shown in Fig. 1.2(a). In a double wall, two walls with surface mass densities m_1'' and m_2'' are separated by an air gap of height d. The qualitative normal incidence sound transmission loss spectrum of an idealized double wall with two homogeneous unbounded walls and no mechanical connection between these walls is shown for two different cases in Fig. 1.2(b): The solid line represents the TL of a double wall without any further treatment of the air gap between the two walls. The dashed line shows the transmission loss of a double wall with an air gap filled by sound absorbing material (e.g. glass wool) to reduce the acoustic coupling be-

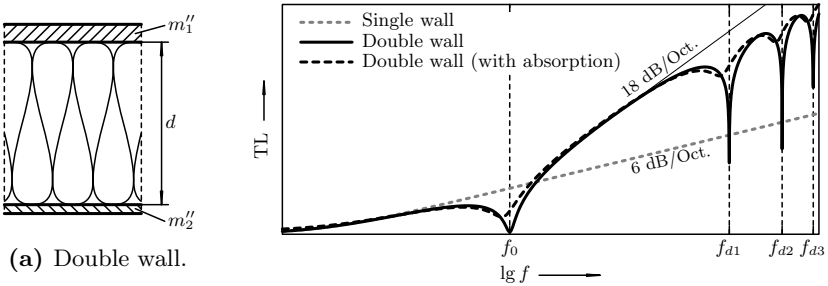

(a) Double wall.

(b) Transmission loss.

Figure 1.2: Typical normal incidence sound transmission loss spectrum of a double wall with and without absorbing material inside the air gap (b), as shown in (a).

tween the two walls. In addition to this, the mass-law transmission loss of a single wall with equal total mass is shown in Fig. 1.2(b) for comparison. For very low frequencies, the transmission loss of the double wall follows the mass-law relationship with the surface mass densities of the two walls combined. At a certain frequency, denoted by f_0 in Fig. 1.2(b), the double wall transmission loss is considerably reduced. This reduction corresponds to the mass-air-mass resonance mode of the double wall system, where the two walls act as masses connected by an air spring. In case of an oblique plane wave with incidence angle θ_i, the mass-air-mass resonance frequency is given by [57]

$$f_0 = \frac{1}{2\pi \cos\theta_\mathrm{i}} \sqrt{\frac{\rho_0 c_0^2}{d} \frac{m_1'' + m_2''}{m_1'' m_2''}}. \tag{1.5}$$

For frequencies greater than f_0, the double wall arrangement exhibits a clear transmission loss improvement over the mass equivalent single wall with TL increasing by up to 18 dB per octave [22]. Thus, the wall spacing d and/or wall masses need to be chosen sufficiently large in order to achieve a benefit over the transmission loss of a single wall with equivalent surface mass density in the low-frequency regime. By this means, the mass-air-mass resonance frequency, as given by Eq. (1.5), is shifted below the lowest frequency of interest. Hence, lightweight double wall constructions for low-frequency noise protection require very large wall spacings, which can be difficult to realize in certain cases where the available installation space for noise protection is strongly limited.

Double walls can be found around the passenger cabins of aircraft, where the fuselage skin with the attached stiffeners and the interior trim panels represent the two walls. The air gap is filled with glass wool for thermal and noise insulation purposes [14, 60, 102]. Typically, the wall spacing is predetermined by the height of the frame stiffeners. Hence, there usually is little to no room for shifting the mass-air-mass resonance frequency to lower frequencies by increasing the wall spacing.

As a result, higher panel masses are required in order to improve the low-frequency noise reduction of aircraft cabin sidewalls in the form of a conventional double wall design, leading to unacceptably high weight penalties for commercial aircraft [78, 103]. There have been several efforts in the past for improving the low-frequency sound transmission loss of double walls without changing the air gap height or panel masses, e.g. by integrating acoustic resonators between the walls [37, 57, 75] or using dynamic vibration absorbers mounted onto the fuselage [91, 102].

The general effect of sound absorbing material added inside the air gap can be seen in Fig. 1.2(b) by comparing the black solid curve (no absorbing material) with the dashed curve (with absorbing material). The absorbing material is most effective at the resonance frequencies, where airborne coupling between the walls is strong. Furthermore, the addition of sound absorbing materials becomes even more beneficial when oblique and diffuse sound fields are propagating through the double wall, because of the increased path length of oblique waves passing through the cavity [22]. Therefore, air gaps inside double walls should be treated with as much absorbing material as possible.

Probably the most widely used sound absorbing materials are porous materials (e.g. melamine foam or glass wool). The primary energy dissipation mechanism in these materials is the conversion of acoustical kinetic energy into heat due to viscous losses. Since viscous forces in linear harmonic dynamic systems are proportional to the frequency f, porous absorbers are particularly efficient at medium to high frequencies, whereas the absorption of these materials at frequencies below $250 \ldots 500$ Hz is rather poor [24]. This, however, can be improved by increasing the thickness of the absorber material or mounting a sheet of absorbing material a 1/4-wavelength apart from a reflecting surface [50]. But since the wavelength of low-frequency acoustic waves in air is typically > 1 m, porous absorbers are rarely used for low-frequency sound absorption.

The low-frequency performance of an acoustic absorber can be improved by increasing the energy density of the system. So-called resonance absorbers combine the significantly increased energy density at the resonance frequency of a dynamic system with a damping mechanism (e.g. internal losses inside a flexing plate). Thus, a greatly improved sound absorption in a frequency band around the resonance frequency can be obtained. Widely used resonance absorbers are, for example, Helmholtz resonators or micro-perforated panels (MPPs) and plate or foil absorbers. The resonant system of Helmholtz resonators and MPPs is composed of the mass of a small air volume in the neck of the resonator and the compliance of a larger air volume enclosed by the resonator. In case of the plate or foil absorbers, the mass of the plate/foil is backed by a compliant air cavity and damping is achieved through the internal losses inside the plate/foil materials [94]. While these absorber types are particularly efficient at low frequencies, their bandwidth is relatively narrow. Only particular tonal components in the noise spectrum can be filtered out unless combinations of resonance absorbers with different properties are employed to achieve a broader sound absorption.

Resonance absorbers have been frequently used in low-frequency noise control problems. As mentioned above, Helmholtz resonators have been used to increase the low-frequency transmission loss of aircraft cabin side walls [37, 57, 75]. Helmholtz resonators have also been employed inside launch vehicle payload fairings in order to protect the payload from excessive low-frequency sound pressure levels during launch [8, 19, 20]. For a similar application, Kidner et al. [33] investigated the enhanced low-frequency noise reduction of poro-elastic layers with randomly embedded masses.

Apart from the passive noise reduction technologies described in this section, numerous active low-frequency noise and vibration control techniques have also been investigated and successfully realized

[14, 17, 25, 76], e.g. in the cabin of the propeller-driven Saab 2000 aircraft [18] or the loadmaster area of the A400M military transporter [34]. While being clearly effective, especially in the low-frequency range, these active technologies require a certain amount of sensors, actuators, control architecture, and cables. This electrical infrastructure can add up to a significant amount of weight and maintenance effort, especially for multi-input and multi-output control systems [25]. Therefore, passive noise protection measures are often preferred by the industry if the acoustic efficiency is comparable. The recently developed so-called *acoustic metamaterials* could provide the basis for new passive noise control technologies with enhanced acoustic performance and lightweight capabilities.

1.2.2. Acoustic metamaterials

The term metamaterial, which first emerged in the late 1990s [5], describes specific structures that have been designed to exhibit – from a classical physics point of view – unusual material properties when subjected to wave propagation phenomena. Despite the name, metamaterials do not represent new kinds of what is typically understood by the term material (such as, for example, metals and metal alloys, natural materials, or fiber-reinforced composites). In fact, metamaterials are composed of conventional materials with the purpose to obtain specific effective material properties when waves are propagating through the material [15].

Veselago [96] was the first to investigate theoretically the electromagnetic properties of metamaterials with simultaneously negative permittivity and permeability. Such – in that time hypothetical – materials, also called *left-handed materials* or *negative-index materials* [47], possess some very remarkable features when subjected to electromagnetic waves, for example a negative refractive index or reversed Doppler effect

[96]. These special properties of left-handed materials can be exploited to create a wide range of structures and devices with previously unseen capabilities [77], such as the so-called perfect lens [71, 111] or even optical cloaks that make the object inside the cloak and the cloak itself invisible to electromagnetic waves [72, 80, 82].

Since light and sound both are fundamentally related by their wave nature, it was not long after the first investigations on electromagnetic metamaterials were published until the first acoustic metamaterials were developed by Liu et al. [48]. The two constituent parameters of acoustic materials – the analogs to the permittivity and permeability of electromagnetic materials – are the mass density ρ_0 and the bulk modulus K_0. These two quantities determine all relevant acoustic material parameters, such as the phase velocity (or speed of sound) $c_0 = \sqrt{K_0/\rho_0}$, the characteristic impedance $Z_0 = \rho_0 c_0 = \sqrt{K_0 \rho_0}$, and the wave number $k_0 = \omega/c_0 = \omega\sqrt{\rho_0/K_0}$ [21]. From these relationships it can be seen that negative values for ρ_0 and K_0 have some remarkable consequences on the acoustical properties of the material. For example, *single-negative acoustic metamaterials*, i.e. acoustic metamaterials with either ρ_0 or K_0 being less than zero, exhibit an imaginary wave number and, consequently, acoustic waves cannot propagate inside an unbounded domain of such a material [49].

The acoustic metamaterial investigated by Liu et al. [48] consisted of small rigid spheres that were coated by a layer of elastic material. Measurement results revealed that the sound transmission through a slab of this composite material can be reduced in small low-frequency bands by at least one order of magnitude compared to the corresponding mass-law transmission. Further theoretical investigations of this new material by Liu et al. [49] attributed the strongly reduced sound transmission to the *effective mass density* of the material becoming negative in these frequency bands.

These first findings on acoustic metamaterials initiated a new re-

search field. Consequently, many new types of acoustic metamaterials have been developed and are still being developed today. These include, for example, single-negative acoustic metamaterials with negative mass density [48, 67, 107] or negative bulk modulus [12, 23, 42] as well as double-negative or *negative-index acoustic metamaterials* [43, 45, 105]. The wide range of proposed acoustic metamaterial realizations provided the groundwork for a variety of applications with acoustic metamaterials, such as perfect acoustic lenses (an analog to the perfect electromagnetic lens) [27, 46, 68], acoustic cloaks [74, 110, 114], broadband absorbing materials [32, 59], and insulation of low-frequency sound [48, 93, 107].

The latter application case is particularly interesting in certain fields in which the insulation of low-frequency noise and lightweight design criteria are two strongly competing requirements. Acoustic metamaterials with negative density have repeatedly been shown to be able to exceed the corresponding mass-law transmission loss by several dB at frequencies well below 1000 Hz [48, 100, 107]. These findings provide a basis for developing new low-frequency noise insulation concepts.

1.2.3. Membrane-type acoustic metamaterials

From the currently available realizations of low-frequency sound insulating acoustic metamaterials, the *membrane-type acoustic metamaterials* (MAMs) – originally proposed by Yang et al. [107, 109] – offer an additional advantage: MAMs are composed of a thin, prestressed membrane layer with one or more small rigid masses attached to it, as shown in Fig. 1.3. Hence, these structures are very compact and, in contrast to the coated spheres proposed by Liu et al. [48], nearly two-dimensional, so that MAMs can be used to cover large surfaces without adding much mass and installation space to the host structure. The qualitative shape of the normal incidence sound transmission loss spectrum of a typical

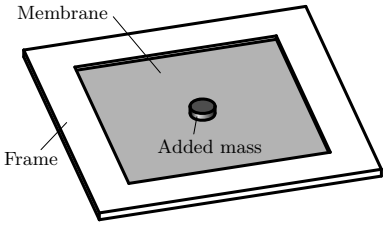

Figure 1.3: Isometric view of a rectangular membrane-type acoustic metamaterial.

MAM structure, as shown in Fig. 1.3, is given in Fig. 1.4(a). Additionally, the corresponding effective density ρ_{eff} of the MAM is shown qualitatively in Fig. 1.4(b). Three characteristic points, denoted by A, B, and C in Fig. 1.4, can be identified in the transmission loss spectrum with the following underlying physical mechanisms [31, 107]:

A: Perfect transmission and consequently zero transmission loss at the eigenfrequency of the first eigenmode of the MAM: The first eigenmode is characterized by large in-phase vibration amplitudes of the added mass and the membrane material. The effective density is zero at this point, changing its sign from negative to positive.

B: Perfect transmission and consequently zero transmission loss at the eigenfrequency of the second eigenmode of the MAM with vanishing effective density: In the second mode, the added mass is nearly at rest while the surrounding membrane material vibrates at large amplitudes. The effective density is zero and undergoes another sign change from negative to positive.

C: Large transmission loss peak and infinite effective density at antiresonance: At this particular frequency, the surface averaged vibrational amplitudes of both eigenmode contributions cancel each

other out and the net vibrational amplitude of the MAM is zero. Consequently, the MAM appears as a nearly impenetrable node to incoming sound waves, as long as the acoustic wavelength is larger than the dimensions of the MAM. The effective density has a pole at this point with an infinitely large absolute value and a sign change from positive to negative.

The experimental and numerical studies by Yang et al. [107] have shown that the first eigenfrequency (point A in Fig. 1.3) and the transmission loss peak (point C) can be tuned during manufacturing of the MAM by choosing appropriate masses. The first eigenfrequency f_1 and the first anti-resonance frequency f_{P1} both are approximately proportional to the inverse of the square root of the added mass magnitude M [53, 63], i.e.

$$f_1 \sim \frac{1}{\sqrt{M}} \quad \text{and} \quad f_{\mathrm{P1}} \sim \frac{1}{\sqrt{M}}. \tag{1.6}$$

Other important parameters for the tuning of MAMs are the prestress resultant of the membrane material T_{m}, which affects both eigenfrequencies and the anti-resonance frequency equally [63], and the size of the area covered by the mass [53, 66].

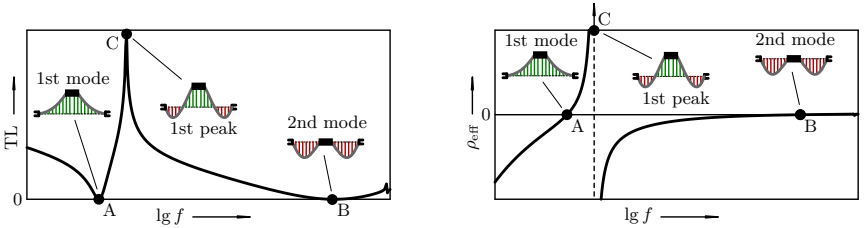

(a) Transmission loss. **(b)** Effective density.

Figure 1.4: Qualitative shape of the normal incidence TL spectrum and effective density ρ_{eff} of a MAM with one added mass in the center.

Based upon the first findings by Yang et al. [107] on small circular MAM test samples, further investigations have emerged in order to better understand and improve the sound insulation performance of MAMs. These include, for example, stacking multiple layers of MAMs [66, 108], using so-called multi-celled panels, where several neighboring MAM cells with different tunings are arranged in parallel [65, 66, 113], off-centered placing of the added mass [59, 112], or attaching multiple masses to one single MAM cell [59, 64]. Apart from the pure reflection of sound waves, MAMs have also been shown to be applicable as an efficient low-frequency broadband absorbing surface [59]. Also, a double-negative acoustic metamaterial with MAMs has been realized by coupling two vertically stacked MAMs with a rigid mechanical connection [105]. Moreover, MAMs have been used as a narrowband acoustic filter around an orifice to reduce the sound propagation inside ducts with air flow at tunable low-frequency bands [55].

1.3. Aim and outline of the work

The recent investigations of MAMs mentioned in the previous section have shown that membrane-type acoustic metamaterials are a very versatile and efficient measure for low-frequency sound insulation, especially when the noise spectrum is dominated by tonal components and lightweight designs are required. There are certain important, yet unanswered questions which are relevant to an application of MAMs in a noise shield design under realistic conditions.

Previous experimental studies of MAMs have focused on impedance tube measurements. Some studies have used small samples fitting inside the tube with a diameter of 100 mm (e.g. [63, 105, 107]). Others have investigated larger samples sandwiched between both parts of the impedance tube in a modified impedance tube setup as proposed by Ho et al. [30] (e.g. [59, 108]). In these impedance tube measurements,

only the propagation of plane acoustic waves is considered, which is rarely found under realistic conditions. Also, numerical and analytical investigations of MAMs have considered solely the transmission of normally incident sound waves (e.g. [10, 112, 113]). Experimental investigations of obliquely incident plane waves on MAMs by Mei et al. [59] have indicated no significant reduction of performance as compared to the normal incidence case. On the other hand, the measurements of a planar metamaterial with a cellular structure similar to a multi-celled MAM panel by Varanasi et al. [93] have revealed a significant influence of a diffuse incident sound field. Hence, there is a need for a better understanding of the sound transmission properties of MAMs under oblique and diffuse incident sound fields.

Furthermore, there have not yet been any investigations of MAMs which are incorporated inside an acoustical enclosure, e.g. between the two walls of a double wall noise shield. All MAM studies available in the current literature address the acoustical performance of bare MAM structures or MAM layers backed by a reflective wall to act as an absorbing metasurface (e.g. [59, 106]). If MAMs are to be placed inside a small enclosure, however, it is possible that the finite air cavities coupled to both sides of the MAM significantly alter their acoustical performance. This has been shown by Yang and Cheng [104] to be the case for microperforated panels (MPPs) inside a small acoustic enclosure. Additionally, there are currently no analytical models for the efficient modeling of such noise shield designs with integrated MAM layers available in the literature.

Finally, noise reduction treatments with MAMs have not yet been investigated at a larger scale and under more practical mounting conditions. The typical characteristic dimensions of a noise shield panel, e.g. mounted on the fuselage of an aircraft, would be in the range of several meters. Because the lateral dimensions of MAMs are required to be smaller than the acoustic wavelength [107], a full-size panel would

be composed of many small MAM unit cells mounted on a large support structure (e.g. a grid). As pointed out by Naify et al. [65], the global compliance of the large-scale support structure and the mutual acoustic coupling of neighboring MAM cells may negatively affect the acoustic performance of the MAMs. The overall size of the 2-by-2 test sample in the impedance tube experiments of Naify et al. [65], however, was much smaller than the acoustic wavelength. Thus, it is still an open question, how noise shielding structures with MAMs perform at a much larger scale and – when applied to the concept of an aircraft noise shield – mounted on top of a realistically sized fuselage.

The aim of the present thesis is to provide answers to these questions using analytical models, laboratory measurements, and numerical simulations in order to provide a basis for the design of efficient low-frequency noise shields using MAMs. In summary, the research questions which will be covered in the following chapters of the present thesis are as follows:

- How do realistic sound fields (i.e. non-orthogonal incidence) and the large-scale dimensions affect the sound transmission loss performance of multi-celled MAM panels compared to the normal incidence sound transmission loss of a single MAM unit cell?
- How can sound barriers with incorporated MAM layers be efficiently and accurately modeled to support the preliminary design process of such structures?
- Is it possible to increase the low-frequency sound transmission loss of multi-layered panels (e.g. a double wall) by introducing additional layers of MAMs?
- Can MAMs be employed in a similar manner to efficiently improve the low-frequency sound transmission loss of a noise shield mounted on top of a realistically sized aircraft fuselage?

The thesis is structured as follows: In Chapter 2, a comprehensive analytical framework for the transmission loss prediction of MAM unit cells and large-scale multi-celled MAM panels under normal and oblique plane wave incidence is derived. Approximate relationships are provided for the common case of sub-wavelength dimensions of the metamaterial unit cells in order to efficiently perform the calculations in the low-frequency range. The analytical models are verified and validated using numerical simulations and measurements, respectively. With these results, the influence of finite dimensions and oblique incidence sound fields on the acoustic performance of MAMs are discussed. Finally, parameter studies are performed to identify important design parameters and their influence on the sound transmission characteristics of MAMs and multi-celled MAM panels. In Chapter 3, an analytical model for predicting the acoustic properties of multi-layered panels containing MAMs is presented. Like in the previous chapter, the model is verified and validated by simulations and experiments, respectively. Parameter studies are performed to investigate the impact of the specific layering arrangement on the sound reduction capabilities of such multi-layered systems. Based upon these findings, a full-scale noise shield demonstrator for the experimental characterization on a realistically sized aircraft fuselage structure is designed in Chapter 4. The experimental results are presented and discussed in this chapter. Finally, the conclusions of the present work are summarized in Chapter 5. The thesis is closed with an outlook for further research activities within the field of membrane-type acoustic metamaterials, especially regarding the application of these metamaterials within a noise shield design.

2. Modeling of MAMs

2.1. Analytical model for MAM unit cells

There have been a number of analytical investigations of MAM structures in order to provide a deeper understanding of the underlying physical mechanisms responsible for the extraordinary low-frequency sound reduction performance of MAMs. The first analytical models for MAM-like structures have been developed already in the 1950s by Kornhauser and Mintzer [35] and Cohen and Handelman [13], who analyzed the free vibrations of circular membranes with a rigid circular mass concentrically attached to the membrane. These studies were later pursued by Wang [98, 99] and Pinto [73] to provide additional insights into the modal characteristics of such structures. Zhang et al. [112] and Tian et al. [89] were the first to propose analytical models specifically tailored for the calculation of the normal incidence sound transmission loss of rectangular MAMs with rectangular added masses and circular MAMs with concentric ring masses, respectively. Those analytical models are able to reproduce most experimental and numerical observations. Furthermore, they provide some additional knowledge regarding the influence of certain parameters, such as the membrane material tension and surface mass density or the offset of the added mass. They do, however, not consider the relatively large stiffness of the added masses, which has been shown by previous investigators to be significant for the dynamic behavior of MAMs [13, 35, 98]. Also, these analytical MAM unit cell models exhibit convergence problems when too many mem-

brane modes are considered in the expansion of the MAM displacement. Subsequently, Chen et al. [10, 11] have published extensive analytical models for circular and rectangular MAMs. These models consider the added masses as rigid bodies and full vibro-acoustic coupling for the calculation of normal incidence sound transmission through the MAMs. Hence, their models provide the most accurate results from the current available analytical models for MAMs. The computational effort of these models, however, is much larger than in the simpler models by Zhang et al. [112] and Tian et al. [89]. This is because Chen et al. use the so-called point-matching approach [62] to couple the edges of the added masses with the edges of the membrane layer. The displacement of the MAM is then expanded in the eigenfunctions of the coupled membrane-mass system. This results in a nonlinear eigenvalue problem to be solved for the eigenmodes of the MAM. This, however, is computationally much more challenging than the standard linear algebra operations necessary in the models by Zhang et al. [112] and Tian et al. [89].

The purpose of the present section is the derivation of a new analytical model for the sound transmission loss calculation of a MAM unit cell loaded with an arbitrarily shaped rigid mass. It should be noted that only one added mass is considered here, because most MAM configurations investigated in the present thesis involve only a single added mass. However, as explained in Appendix A, the model can be readily extended to allow for multiple masses per unit cell. Such MAM designs can be useful to introduce multiple anti-resonances and thus increase the bandwidth of the MAM unit cell [59, 64].

The aim of the model is to combine the computational efficiency of the analytical models by Zhang et al. [112] and Tian et al. [89] with Chen et al.'s accurate representation of the mass stiffness [10, 11], yielding a versatile and efficient method for predicting the sound transmission loss through MAMs. In the first subsection, the governing

equations for the MAM are derived and the resulting linear system of equations for the vibrational response of the MAM under an acoustic pressure load is presented. Section 2.1.2 discusses the method for extracting the in vacuo eigenmodes of the MAM, which can be used to reduce the order of the governing system of equations considerably. Then, in Section 2.1.3, the vibro-acoustic coupling is introduced to obtain the oblique incidence sound transmission coefficient of an infinite array of MAM unit cells. Finally, in Section 2.1.4 this approach is significantly simplified for sub-wavelength sized MAM unit cells leading to the effective surface mass density approximation for MAMs.

2.1.1. Governing equations

A schematic drawing of the single rectangular membrane-type acoustic metamaterial cell considered in this work is shown in Fig. 2.1. A cell consists of a rectangular sheet of a prestressed membrane material with length L_x and width L_y. Without loss of generality, it is assumed that L_x corresponds to the longer edge if the unit cell is not a square. The membrane material has a surface mass density m''_{m} and a uniform prestress resultant T_{m}. The Young's modulus and Poisson's ratio of the membrane material are denoted by E_{m} and ν_{m}, respectively, and the membrane thickness is given by h_{m}. Thus, the bending stiffness of the membrane material is $B_{\mathrm{m}} = E_{\mathrm{m}} h_{\mathrm{m}}^3/(12(1-\nu_{\mathrm{m}}^2))$ [44, p. 1]. A right-handed Cartesian coordinate system (x, y, z) is defined at one cor-

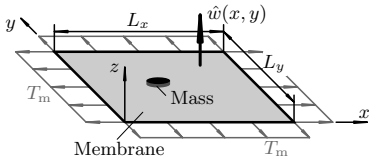

Figure 2.1: Schematic drawing of a single rectangular MAM unit cell.

ner of the membrane, with the x- and y-axis pointing in the L_x- and L_y-direction, respectively, and the z-axis being perpendicular to the membrane plane.

The dynamic transversal displacement of the membrane $w(x, y, t)$ is assumed to have a harmonic time dependence with

$$w(x, y, t) = \mathrm{Re}\left\{\hat{w}(x, y)\mathrm{e}^{\mathrm{i}\omega t}\right\}, \tag{2.1}$$

where Re{} denotes the real part of a complex quantity and $\hat{w}(x, y)$ is the (complex) transversal displacement amplitude of the membrane. The governing equation for the membrane vibration amplitude $\hat{w}$ resulting from a harmonic pressure difference $\Delta P(x, y, t) = \Delta\hat{P}(x, y)\mathrm{e}^{\mathrm{i}\omega t}$ between both sides of the MAM is given by

$$-m''_{\mathrm{m}}\omega^2\hat{w} - T_{\mathrm{m}}\nabla^2\hat{w} + B_{\mathrm{m}}\nabla^4\hat{w} = \Delta\hat{P} + \hat{f}''_{\mathrm{M}}, \tag{2.2}$$

which represents the instantaneous equilibrium of forces per unit area acting on the membrane [44, p. 267]. In Eq. (2.2), $\nabla^2 = \frac{\partial^2}{\partial x^2} + \frac{\partial^2}{\partial y^2}$ is the Laplace operator in Cartesian coordinates, $\nabla^4 = \nabla^2\nabla^2$, $\Delta\hat{P}(x, y)$ is the complex pressure amplitude difference, and $\hat{f}''_{\mathrm{M}}$ represents the transversal internal stress amplitude between the membrane and the attached mass. This stress accounts for the inertia and the rigidity of the added mass and is, in general, a continuous function over the common interface area of the membrane and the mass (see Fig. 2.2).

In order to identify the relevant parameters for the acoustical properties of a MAM unit cell, Eq. (2.2) is transformed into a dimensionless

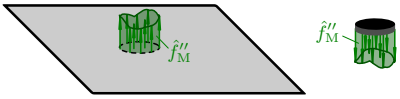

Figure 2.2: Illustration of the internal stress amplitude $\hat{f}''_{\mathrm{M}}$ acting between the membrane and the attached mass.

form with the dimensionless coordinates $\xi = x/L_x$, $\eta = y/L_y$, and $\zeta = z/L_x$, the dimensionless displacement amplitude $u = \hat{w}/L_x$, the dimensionless frequency $\Omega = \omega/\omega_{\mathrm{ref}}$, the reference frequency $\omega_{\mathrm{ref}} = \sqrt{T_{\mathrm{m}}/m''_{\mathrm{m}}}/L_x$, the aspect ratio $\Lambda = L_x/L_y \geq 1$ (because, as mentioned above, L_x is assigned to the longer edge of the MAM unit cell), the dimensionless bending stiffness $\Xi = B_{\mathrm{m}}/(T_{\mathrm{m}}L_x^2)$, the dimensionless pressure amplitude difference $\Delta\beta = \Delta\hat{P}L_x/T_{\mathrm{m}}$, and the dimensionless membrane-mass interaction stress amplitude $\gamma'' = \hat{f}''_{\mathrm{M}}L_x/T_{\mathrm{m}}$. This yields:

$$-\Omega^2 u - u_{,\xi\xi} - \Lambda^2 u_{,\eta\eta} + \Xi\left(u_{,\xi\xi\xi\xi} + 2\Lambda^2 u_{,\xi\xi\eta\eta} + \Lambda^4 u_{,\eta\eta\eta\eta}\right) = \Delta\beta + \gamma'', \tag{2.3}$$

where indices behind a comma denote partial derivatives with respect to the given coordinates.

In order to find a weak solution of Eq. (2.3), the Galerkin method of weighted residuals is employed by expanding the dimensionless membrane displacement amplitude u in terms of the eigenfunctions Φ_{mn} of the unloaded membrane. Assuming the membrane edges to be simply supported, the membrane eigenfunctions are given by [44]

$$\Phi_{mn} = 2\sin(m\pi\xi)\sin(n\pi\eta), \tag{2.4}$$

which, without loss of generality, have been normalized such that

$$\langle \Phi_{mn}, \Phi_{m'n'} \rangle = \begin{cases} 1 & \text{for } m = m' \wedge n = n' \\ 0 & \text{else,} \end{cases} \tag{2.5}$$

where $\langle f, g \rangle = \int_0^1 \int_0^1 fg \,\mathrm{d}\eta \,\mathrm{d}\xi$ denotes the L^2-inner product of two functions f and g along the surface of the membrane. The expansion is truncated after $N = N_x N_y$ membrane eigenmodes, where N_x and N_y

are the maximum indices of the modes in the x- and y-direction, respectively. Thus, the following approximate expression for u results:

$$u \approx \sum_{m=1}^{N_x} \sum_{n=1}^{N_y} c_{mn} \Phi_{mn} = \sum_{mn} c_{mn} \Phi_{mn}, \tag{2.6}$$

with the membrane modal participation factor c_{mn}. Basically, Eq. (2.6) is a Fourier series representation of u, which becomes more accurate the more number of terms N are included in the expansion. Section 2.3 provides a typical choice for N to obtain an approximation of u using Eq. (2.6) with reasonable accuracy.

Inserting Eq. (2.6) into the governing equation (2.3) and following the Galerkin approach by using the membrane eigenfunctions $\Phi_{m'n'}$ as weighting functions yields the following algebraic equation for c_{mn} after integrating over the membrane surface:

$$\left(\varkappa_{mn} - \Omega^2\right) c_{mn} = \langle \Phi_{mn}, \Delta\beta \rangle + \left\langle \Phi_{mn}, \gamma'' \right\rangle, \tag{2.7}$$

where $\varkappa_{mn} = \widetilde{\varkappa}_{mn} + \Xi \widetilde{\varkappa}_{mn}^2$ are the squared nondimensional eigenfrequencies of the unloaded membrane with $\widetilde{\varkappa}_{mn} = \pi^2 \left(m^2 + \Lambda^2 n^2\right)$.

As illustrated in Fig. 2.3(a), the added mass is provided with a local Cartesian coordinate system (x', y', z'). The origin is placed in the center of gravity of the mass, with the z'-axis being parallel to the z-axis of the global membrane coordinate system and the x'- and y'-axes corresponding to the principal axes of inertia of the mass. The rotation of the local coordinate system around the z'-axis with respect to the global membrane coordinate system is given by θ' and the coordinates of the mass center of gravity in the membrane coordinate system are denoted by x^*, y^*, and z^*. It is assumed that the rigidity of the mass is much higher than the stiffness of the underlying membrane material. Also, only the out-of-plane vibration of the membrane is considered here. Hence, the dynamic motion of the mass is fully determined by

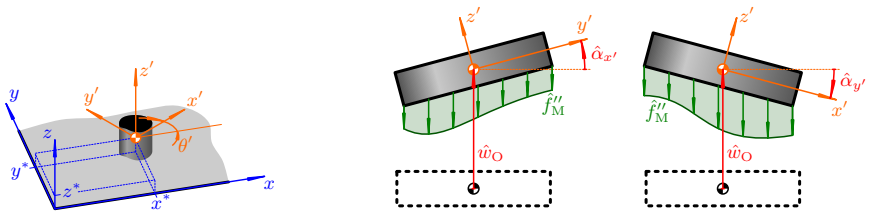

(a) Local coordinate system of the mass.

(b) Mass motion due to the membrane-mass interaction stress $\hat{f}''_{\mathrm{M}}$.

Figure 2.3: Definitions for the local coordinate system and rigid body motion of the attached mass.

the rigid body motion in z'-direction (translation) and around the x'- and y'-axes (rotation) due to the membrane-mass interaction stress $\hat{f}''_{\mathrm{M}}$ acting upon the mass (see Fig. 2.3(b)). Thus, the vertical displacement amplitude of the mass center of gravity $\hat{w}_{\mathrm{O}}$ is governed by Newton's second law of motion

$$-M\omega^2\hat{w}_{\mathrm{O}} = -\iint_{S_{\mathrm{M}}} \hat{f}''_{\mathrm{M}}(x',y')\,\mathrm{d}y'\,\mathrm{d}x', \tag{2.8}$$

where M is the mass magnitude and S_{M} denotes the common surface of the mass and the membrane. The rotational amplitudes $\hat{\alpha}_{x'}$ and $\hat{\alpha}_{y'}$ follow the linearized Euler equations as

$$-J_{x'}\omega^2\hat{\alpha}_{x'} = -\iint_{S_{\mathrm{M}}} \hat{f}''_{\mathrm{M}}(x',y')y'\,\mathrm{d}y'\,\mathrm{d}x' \tag{2.9}$$

and

$$-J_{y'}\omega^2\hat{\alpha}_{y'} = \iint_{S_{\mathrm{M}}} \hat{f}''_{\mathrm{M}}(x',y')x'\,\mathrm{d}y'\,\mathrm{d}x', \tag{2.10}$$

where $J_{x'}$ and $J_{y'}$ are the principal moments of inertia of the mass about the x'- and y'-axis, respectively.

Eqs. (2.8) to (2.10) are rewritten in dimensionless form and solved for the three degrees of freedom of the mass $u_\mathrm{O} = \hat{w}_\mathrm{O}/L_x$, $\alpha_{\xi'} = \hat{\alpha}_{x'}$, and $\alpha_{\eta'} = \hat{\alpha}_{y'}$:

$$u_\mathrm{O} = \frac{1}{\Lambda\mu\Omega^2} \iint\limits_{S_\mathrm{M}} \gamma''(\xi', \eta') \,\mathrm{d}\eta' \,\mathrm{d}\xi', \tag{2.11a}$$

$$\alpha_{\xi'} = \frac{1}{\Lambda\mu\Omega^2} \frac{1}{\Lambda\vartheta_{\xi'}} \iint\limits_{S_\mathrm{M}} \gamma''(\xi', \eta')\eta' \,\mathrm{d}\eta' \,\mathrm{d}\xi', \quad \text{and} \tag{2.11b}$$

$$\alpha_{\eta'} = -\frac{1}{\Lambda\mu\Omega^2} \frac{1}{\vartheta_{\eta'}} \iint\limits_{S_\mathrm{M}} \gamma''(\xi', \eta')\xi' \,\mathrm{d}\eta' \,\mathrm{d}\xi', \tag{2.11c}$$

where $\xi' = x'/L_x$ and $\eta' = y'/L_y$ are the dimensionless forms of the local mass coordinate system, $\mu = M/(m''_\mathrm{m} L_x^2)$ is the dimensionless added mass magnitude, and $\vartheta_{\xi'} = J_{x'}/(ML_x^2)$ and $\vartheta_{\eta'} = J_{y'}/(ML_x^2)$ are the dimensionless squared radii of gyration. The kinematic relationship for the dimensionless displacement of the mass u_M at a specific local coordinate pair (ξ', η') is given by

$$u_\mathrm{M}(\xi', \eta') = u_\mathrm{O} - \alpha_{\eta'}\xi' + \frac{1}{\Lambda}\alpha_{\xi'}\eta'. \tag{2.12}$$

The mass is assumed to be rigidly coupled to the membrane layer. Hence, the displacement amplitudes of the membrane and the mass must be continuous along the common surface S_M:

$$u(\xi, \eta) \stackrel{!}{=} u_\mathrm{M}(\xi', \eta') \quad \text{for } (\xi, \eta) \in S_\mathrm{M}, \tag{2.13}$$

with the following relationship between the global coordinate system

(ξ, η, ζ) and the local mass coordinate system (ξ', η', ζ'):

$$\xi = \xi^* + \cos\theta'\,\xi' - \sin\theta'\,\eta'/\Lambda, \tag{2.14a}$$
$$\eta = \eta^* + \Lambda\sin\theta'\,\xi' + \cos\theta'\,\eta', \quad \text{and} \tag{2.14b}$$
$$\zeta = \zeta^* + \zeta'. \tag{2.14c}$$

So far, the physical problem of the MAM unit cell with a mass attached to the membrane is only expressed in mathematical terms. The distribution of the dimensionless membrane-mass interaction stress γ'' in Eqs. (2.3) and (2.11) is generally not known a-priori. Hence, solving these equations for the membrane and mass displacements taking into account the continuity condition in Eq. (2.13) poses a nontrivial problem for general MAM configurations. As mentioned in the introduction of this section, different approaches have been employed by other authors to simplify this problem. Zhang et al. [112], on the one hand, modeled the added mass as a limp body and Chen et al. [10, 11], on the other hand, used the point matching approach to couple only the mass edges to the membrane using discrete point forces, which results in a nonlinear eigenvalue problem. The present analytical model, however, provides a new modeling approach for the coupling between the mass and the membrane which accounts for the rigidity of the mass and results in a linear system of equations that can be solved efficiently. This is achieved by approximating the membrane-mass interaction stress $\hat{f}''_{\mathrm{M}}$ with discrete point forces distributed across the whole common surface of the membrane and mass (see Fig. 2.4):

$$\hat{f}''_{\mathrm{M}} \approx \sum_{j=1}^{I} \hat{f}_{\mathrm{M},j}\,\delta(x - x_j)\,\delta(y - y_j)\,, \tag{2.15}$$

where I is the number of matching points, δ is the Dirac delta function, $\hat{f}_{\mathrm{M},j}$ is the (complex) point force amplitude, and x_j and y_j are the global

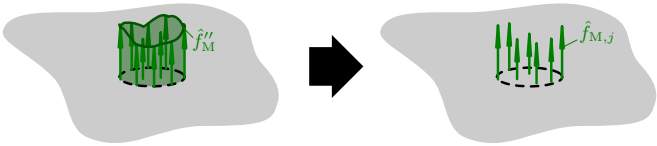

Figure 2.4: Illustration of the point matching approach, where the continuous membrane-mass interaction stress $\hat{f}''_{\mathrm{M}}$ is replaced by a finite set of point forces $\hat{f}_{\mathrm{M},j}$ distributed along the common surface of the membrane and mass.

coordinates of the j-th matching point. Eq. (2.15) is expressed in terms of the dimensionless membrane-mass interaction stress γ'' as

$$\gamma'' \approx \sum_j \gamma_j \delta(\xi - \xi_j)\, \delta(\eta - \eta_j)\,, \tag{2.16}$$

where $\gamma_j = \hat{f}_{\mathrm{M},j}/(T_{\mathrm{m}} L_x)$ is the dimensionless point force of the j-th matching point. Substituting this approximation into the governing equations for the mass motion, Eq. (2.11), yields

$$u_{\mathrm{O}} = \frac{1}{\Lambda\mu\Omega^2} \sum_j \gamma_j, \tag{2.17a}$$

$$\alpha_{\xi'} = \frac{1}{\Lambda\mu\Omega^2} \frac{1}{\Lambda\vartheta_{\xi'}} \sum_j \eta'_j \gamma_j, \quad \text{and} \tag{2.17b}$$

$$\alpha_{\eta'} = -\frac{1}{\Lambda\mu\Omega^2} \frac{1}{\vartheta_{\eta'}} \sum_j \xi'_j \gamma_j. \tag{2.17c}$$

This can be written in matrix form as follows:

$$\Omega^2 \mathbf{u}_{\mathrm{M}} = \mathbf{Q}\boldsymbol{\gamma}, \tag{2.18}$$

where

$$\mathbf{u}_{\mathrm{M}} = \sqrt{\Lambda\mu} \begin{bmatrix} 1 & 0 & 0 \\ 0 & \sqrt{\vartheta_{\xi'}} & 0 \\ 0 & 0 & \sqrt{\vartheta_{\eta'}} \end{bmatrix} \begin{pmatrix} u_{\mathrm{O}} \\ \alpha_{\xi'} \\ \alpha_{\eta'} \end{pmatrix} \in \mathbb{C}^3 \tag{2.19}$$

contains the scaled mass degrees of freedom, $\boldsymbol{\gamma} = (\gamma_j) \in \mathbb{C}^I$ consists of the matching point forces of the mass, and

$$\mathbf{Q} = \frac{1}{\sqrt{\Lambda\mu}} \begin{bmatrix} 1 & 0 & 0 \\ 0 & \Lambda\sqrt{\vartheta_{\xi'}} & 0 \\ 0 & 0 & -\sqrt{\vartheta_{\eta'}} \end{bmatrix}^{-1} \begin{bmatrix} 1 & \cdots & 1 \\ \eta'_1 & \cdots & \eta'_I \\ \xi'_1 & \cdots & \xi'_I \end{bmatrix} \in \mathbb{R}^{3\times I} \tag{2.20}$$

defines the dynamic relationship between the scaled mass degrees of freedom and the matching point forces according to Eq. (2.17).

The continuity condition for the membrane and mass displacements in Eq. (2.13) is enforced only at the matching point locations so that Eq. (2.13) can be rewritten using Eqs. (2.6) and (2.12) as

$$\sum_{mn} c_{mn} \Phi_{mn}^{(j')} \stackrel{!}{=} u_{\mathrm{O}} - \alpha_{\eta'} \xi'_{j'} + \frac{1}{\Lambda} \alpha_{\xi'} \eta'_{j'}, \tag{2.21}$$

where $\Phi_{mn}^{(j')} = 2\sin(m\pi\xi_{j'})\sin(n\pi\eta_{j'})$ corresponds to the value of the membrane mode eigenfunction Φ_{mn} at the location of the j'-th matching point in the global coordinate system. With the matrix notation introduced in Eq. (2.18), this yields the system of equations

$$\mathbf{L}^{\mathrm{T}}\mathbf{c} = \mathbf{Q}^{\mathrm{T}}\mathbf{u}_{\mathrm{M}}. \tag{2.22}$$

$\mathbf{L}^{\mathrm{T}}$ denotes the transpose of $\mathbf{L} = (l_{mnj}) \in \mathbb{R}^{N\times I}$ which is, in general, a fully populated rectangular matrix representing the coupling between the membrane and mass with

$$l_{mnj} = \Phi_{mn}^{(j)} = 2\sin(m\pi\xi_j)\sin(n\pi\eta_j). \tag{2.23}$$

The vector $\mathbf{c} \in \mathbb{C}^N$ contains the membrane modal participation factors c_{mn}.

Additionally, the matching point approximation for γ'' in Eq. (2.16) is inserted into the algebraic equation (2.7) to yield

$$\left(\varkappa_{mn} - \Omega^2\right) c_{mn} = \langle \Phi_{mn}, \Delta\beta \rangle + \sum_j \Phi_{mn}^{(j)} \gamma_j. \tag{2.24}$$

This results in a linear system of equations, which can also be written in matrix form such that

$$\left(\mathbf{C} - \Omega^2\mathbf{I}\right)\mathbf{c} = \boldsymbol{\Delta\beta} + \mathbf{L}\boldsymbol{\gamma}, \tag{2.25}$$

where the stiffness matrix $\mathbf{C} = (\varkappa_{mnm'n'}) \in \mathbb{R}^{N\times N}$ is diagonal with

$$\varkappa_{mnm'n'} = \begin{cases} \widetilde{\varkappa}_{mn} + \Xi\widetilde{\varkappa}_{mn}^2 & \text{if } m = m' \wedge n = n' \\ 0 & \text{else} \end{cases} \tag{2.26}$$

and $\mathbf{I}$ is the identity matrix with compatible dimensions. On the right hand side, the elements of the acoustic pressure difference vector $\boldsymbol{\Delta\beta} \in \mathbb{C}^N$ are, in the general case, given by $\Delta\beta_{mn} = \langle \Phi_{mn}, \Delta\beta\rangle$.

Eqs. (2.18), (2.22), and (2.25) form a coupled linear system of equations for the membrane modal participation factors $\mathbf{c}$, the scaled mass degrees of freedom $\mathbf{u}_\mathrm{M}$, and the matching point forces $\boldsymbol{\gamma}$ given by

$$\begin{bmatrix} \mathbf{C} - \Omega^2\mathbf{I} & \mathbf{0} & -\mathbf{L} \\ \mathbf{0} & -\Omega^2\mathbf{I} & \mathbf{Q} \\ -\mathbf{L}^\mathrm{T} & \mathbf{Q}^\mathrm{T} & \mathbf{0} \end{bmatrix} \begin{pmatrix} \mathbf{c} \\ \mathbf{u}_\mathrm{M} \\ \boldsymbol{\gamma} \end{pmatrix} = \begin{pmatrix} \boldsymbol{\Delta\beta} \\ \mathbf{0} \\ \mathbf{0} \end{pmatrix}. \tag{2.27}$$

If structural damping of the membrane material needs to be considered, the stiffness matrix $\mathbf{C}$ in Eq. (2.27) can be replaced by the complex stiffness matrix $\widetilde{\mathbf{C}} = (1 + \mathrm{i}\eta_\mathrm{m})\mathbf{C}$ with the structural loss factor of the membrane material η_m.

The acoustic pressure difference vector $\boldsymbol{\Delta\beta}$ in Eq. (2.27) depends on the fluid surroundings coupled to the vibration of the MAM. Before the vibro-acoustical coupling of the MAM unit cell is discussed, the following subsection will cover the extraction of the in vacuo eigenmodes of the MAM unit cell from Eq. (2.27).

2.1.2. Eigenmode extraction

In order to find the squared dimensionless in vacuo eigenfrequencies Ω_i^2 and eigenvectors $\mathbf{v}_i$ of the MAM, the homogeneous form of the

governing linear system of equations (2.27) can be written in the form of a generalized eigenvalue problem as

$$\underbrace{\begin{bmatrix} \mathbf{C} & \mathbf{0} & -\mathbf{L} \\ \mathbf{0} & \mathbf{0} & \mathbf{Q} \\ -\mathbf{L}^{\mathrm{T}} & \mathbf{Q}^{\mathrm{T}} & \mathbf{0} \end{bmatrix}}_{\mathbf{A}} \underbrace{\begin{pmatrix} \mathbf{v}_{i,c} \\ \mathbf{v}_{i,u_{\mathrm{M}}} \\ \mathbf{v}_{i,\gamma} \end{pmatrix}}_{\mathbf{v}_i} = \Omega_i^2 \underbrace{\begin{bmatrix} \mathbf{I} & \mathbf{0} & \mathbf{0} \\ \mathbf{0} & \mathbf{I} & \mathbf{0} \\ \mathbf{0} & \mathbf{0} & \mathbf{0} \end{bmatrix}}_{\mathbf{B}} \underbrace{\begin{pmatrix} \mathbf{v}_{i,c} \\ \mathbf{v}_{i,u_{\mathrm{M}}} \\ \mathbf{v}_{i,\gamma} \end{pmatrix}}_{\mathbf{v}_i}, \tag{2.28}$$

where $\mathbf{v}_{i,c}$, $\mathbf{v}_{i,u_{\mathrm{M}}}$, and $\mathbf{v}_{i,\gamma}$ are the parts of the eigenvector $\mathbf{v}_i$ assigned to $\mathbf{c}$, $\mathbf{u}_{\mathrm{M}}$, and $\boldsymbol{\gamma}$, respectively. With the coefficient matrices $\mathbf{A}$ and $\mathbf{B}$ defined as indicated in Eq. (2.28), the generalized eigenvalue problem takes the form

$$\mathbf{A}\mathbf{v}_i = \Omega_i^2 \mathbf{B}\mathbf{v}_i. \tag{2.29}$$

From Eq. (2.28) it is obvious that $\mathbf{B}$ is symmetric positive-semidefinite with $\operatorname{rank}\mathbf{B} = N + 3$. $\mathbf{A}$, on the other hand, is nonsingular, since $\mathbf{C}$ is symmetric positive-definite and the Schur complement

$$\mathbf{A}/\mathbf{C} = \begin{bmatrix} \mathbf{0} & \mathbf{Q} \\ \mathbf{Q}^{\mathrm{T}} & -\mathbf{L}^{\mathrm{T}}\mathbf{C}^{-1}\mathbf{L} \end{bmatrix} \tag{2.30}$$

is also invertible, presuming that $N \geq I \geq 3$ and both $\mathbf{L}$ and $\mathbf{Q}$ are full rank matrices. Thus, the generalized eigenvalue problem (2.29) yields $N + 3$ finite squared eigenfrequencies Ω_i^2 and I solutions with $1/\Omega_i^2 = 0$, i.e. $\Omega_i^2 \to \infty$. The latter eigenmodes are of no practical interest. Therefore, the so-called Fix–Heiberger reduction method [69] can be applied to Eq. (2.29). As shown in Appendix B, this procedure reduces the size of the eigenvalue problem so that it includes just the $N + 3$ finite eigenvalues of the system.

In practice, only the $\hat{N}$ lowest eigenfrequencies Ω_i and corresponding eigenvectors $\mathbf{v}_i$ are of interest for the acoustic properties of the MAM unit cell. As a general rule of thumb, $\hat{N}$ should be selected such that all eigenmodes below at least twice the largest excitation frequency are

considered [92]. The corresponding eigenvectors can be used to assemble a reduced eigenvector matrix $\hat{\mathbf{V}} = (\mathbf{v}_1, \ldots, \mathbf{v}_{\hat{N}})$. Appendix B shows that this set of eigenvectors simultaneously diagonalizes the system matrices $\mathbf{A}$ and $\mathbf{B}$ in Eq. (2.29), so that $\hat{\mathbf{V}}^{\mathrm{T}}\mathbf{A}\hat{\mathbf{V}} = \hat{\mathbf{\Lambda}}$, where $\hat{\mathbf{\Lambda}}$ is diagonal containing the first $\hat{N}$ squared eigenfrequencies Ω_i^2, and $\hat{\mathbf{V}}^{\mathrm{T}}\mathbf{B}\hat{\mathbf{V}} = \mathbf{I}$. The vectors $\mathbf{c}$, $\mathbf{u}_{\mathrm{M}}$, and $\boldsymbol{\gamma}$ in Eq. (2.27) can be expanded in terms of the eigenvectors as

$$\mathbf{c} \approx \sum_{i=1}^{\hat{N}} \hat{c}_i \mathbf{v}_{i,c} = \hat{\mathbf{V}}_c \hat{\mathbf{c}}, \tag{2.31a}$$

$$\mathbf{u}_{\mathrm{M}} \approx \sum_{i=1}^{\hat{N}} \hat{c}_i \mathbf{v}_{i,u_{\mathrm{M}}} = \hat{\mathbf{V}}_{u_{\mathrm{M}}} \hat{\mathbf{c}}, \quad \text{and} \tag{2.31b}$$

$$\boldsymbol{\gamma} \approx \sum_{i=1}^{\hat{N}} \hat{c}_i \mathbf{v}_{i,\gamma} = \hat{\mathbf{V}}_{\gamma} \hat{\mathbf{c}}, \tag{2.31c}$$

respectively. This can be inserted into the system of equations (2.27) to yield after left-multiplication with $\hat{\mathbf{V}}^{\mathrm{T}} = [\hat{\mathbf{V}}_c^{\mathrm{T}}, \hat{\mathbf{V}}_{u_{\mathrm{M}}}^{\mathrm{T}}, \hat{\mathbf{V}}_{\gamma}^{\mathrm{T}}]$ the reduced modal form of Eq. (2.27)

$$\left(\hat{\mathbf{\Lambda}} - \Omega^2 \mathbf{I}\right) \hat{\mathbf{c}} = \boldsymbol{\Delta}\hat{\boldsymbol{\beta}}, \tag{2.32}$$

where $\boldsymbol{\Delta}\hat{\boldsymbol{\beta}} = \hat{\mathbf{V}}_c^{\mathrm{T}} \boldsymbol{\Delta}\boldsymbol{\beta}$.

2.1.3. Fluid-structure coupling

For the fully coupled fluid-structure interaction model, the MAM unit cell from Fig. 2.1 is considered to be part of an infinite planar array of this unit cell, as indicated in Fig. 2.5. Each MAM cell is uniquely identified with the indices $p \in \{\ldots, -2, -1, 0, 1, 2, \ldots\}$ and $q \in \{\ldots, -2,$

$-1, 0, 1, 2, \ldots\}$. The index pair (p, q) refers to the MAM unit cell ranging over $pL_x < x < (p+1)L_x$ and $qL_y < y < (q+1)L_y$. A fluid half space with density ρ_0 and speed of sound c_0 is coupled to each side of the MAM array, extending to $z \to -\infty$ and $z \to +\infty$, respectively. The acoustic pressure fields in those half spaces are given by $\hat{P}^-(x, y, z)$, for the source side of the MAM at $z < 0$, and $\hat{P}^+(x, y, z)$, for the transmission side of the MAM at $z > 0$. The MAM is acoustically excited by an obliquely incident plane wave with pressure amplitude $\hat{P}_{\mathrm{i}0}$ and wave vector

$$\mathbf{k}_{\mathrm{i}} = \begin{pmatrix} k_{\mathrm{i}x} \\ k_{\mathrm{i}y} \\ k_{\mathrm{i}z} \end{pmatrix} = k_0 \begin{pmatrix} \sin\theta_{\mathrm{i}} \cos\phi_{\mathrm{i}} \\ \sin\theta_{\mathrm{i}} \sin\phi_{\mathrm{i}} \\ \cos\theta_{\mathrm{i}} \end{pmatrix}, \tag{2.33}$$

where θ_{i} is the incidence angle and ϕ_{i} is the azimuth of the plane wave (see Fig. 2.5). After introducing the nondimensionalized incident pressure field as $\beta_{\mathrm{i}} = \hat{P}_{\mathrm{i}} L_x / T_{\mathrm{m}}$, the dimensionless pressure field of the incident sound wave in the source side fluid half space is given by

$$\beta_{\mathrm{i}}(\xi, \eta, \zeta) = \beta_{\mathrm{i}0} \mathrm{e}^{-\mathrm{i}\left(\kappa_\xi \xi + \kappa_\eta \eta + \kappa_\zeta \zeta\right)}, \tag{2.34}$$

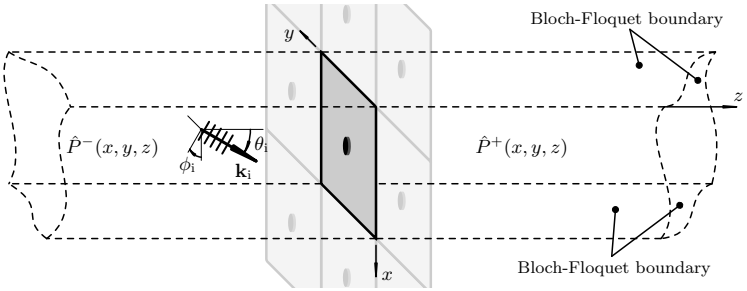

Figure 2.5: Setup for the fluid-structure interaction model between the MAM unit cell and the adjacent fluid half spaces with Bloch-Floquet periodic boundaries.

where $\kappa_\xi = k_{\mathrm{i}x} L_x$, $\kappa_\eta = k_{\mathrm{i}y} L_y$, and $\kappa_\zeta = k_{\mathrm{i}z} L_x$ are the dimensionless forms of the Cartesian incident wave number components. The nondimensional acoustic pressure field $\beta^- = \hat{P}^- L_x / T_\mathrm{m}$ can be decomposed into a blocked pressure part β_bl, given by

$$\begin{aligned} \beta_\mathrm{bl}(\xi,\eta,\zeta) &= \beta_\mathrm{i}(\xi,\eta,\zeta) + \beta_\mathrm{i}(\xi,\eta,-\zeta) \\ &= \beta_{\mathrm{i}0} \mathrm{e}^{-\mathrm{i}\left(\kappa_\xi \xi + \kappa_\eta \eta\right)} \left(\mathrm{e}^{-\mathrm{i}\kappa_\zeta \zeta} + \mathrm{e}^{\mathrm{i}\kappa_\zeta \zeta}\right), \end{aligned} \tag{2.35}$$

and a reradiated pressure part β_rr, resulting from the radiation of sound on both sides of the MAM [14, p. 97]. Thus, the source side pressure field can be expressed as $\beta^- = \beta_\mathrm{bl} - \beta_\mathrm{rr}$. The pressure field on the other side of the MAM $\beta^+ = \hat{P}^+ L_x / T_\mathrm{m}$ is equal only to β_rr, because no external sound field is present on this side and the MAM is many orders of magnitude thinner than the acoustic wavelength. Thus, the nondimensional acoustic pressure amplitude difference on the MAM surface $\Delta\beta$ is

$$\begin{aligned} \Delta\beta(\xi,\eta) &= \beta^-(\xi,\eta,0) - \beta^+(\xi,\eta,0) \\ &= 2\beta_{\mathrm{i}0} \mathrm{e}^{-\mathrm{i}\left(\kappa_\xi \xi + \kappa_\eta \eta\right)} - 2\beta_\mathrm{rr}(\xi,\eta,0). \end{aligned} \tag{2.36}$$

Consequently, the acoustic pressure difference vector $\boldsymbol{\Delta\beta}$ in the system of equations (2.27) can be written as

$$\boldsymbol{\Delta\beta} = 2\beta_{\mathrm{i}0}\mathbf{b} - 2\boldsymbol{\beta}_\mathrm{rr}, \tag{2.37}$$

where $\mathbf{b} = (b_{mn}) \in \mathbb{C}^N$ is the membrane mode excitation vector depending only on the properties of the incident sound field with

$$b_{mn} = 2mn\pi^2 \frac{(-1)^m \mathrm{e}^{-\mathrm{i}\kappa_\xi} - 1}{\kappa_\xi^2 - m^2\pi^2} \frac{(-1)^n \mathrm{e}^{-\mathrm{i}\kappa_\eta} - 1}{\kappa_\eta^2 - n^2\pi^2} \tag{2.38}$$

and $\boldsymbol{\beta}_\mathrm{rr}$ is obtained from the reradiated sound pressure field, which in general is a function of the membrane displacement amplitude u.

From the nature of the incident plane wave it follows that each MAM unit cell is excited by a pressure field, which differs from the pressure excitation field of any other unit cell only by a constant phase shift. Thus, the incident sound pressure field can be expressed in the form of a Bloch-Floquet wave as [29]

$$\beta_{\mathrm{i}}(\xi + p, \eta + q, \zeta) = \beta_{\mathrm{i}}(\xi, \eta, \zeta)\mathrm{e}^{-\mathrm{i}\left(\kappa_\xi p + \kappa_\eta q\right)}. \tag{2.39}$$

Eq. (2.39) indicates that the incident sound field is – apart from a phase difference factor of $\mathrm{e}^{-\mathrm{i}(\kappa_\xi p + \kappa_\eta q)}$ – periodic at the unit cell edges. This periodicity also applies to the vibrational response of the MAM unit cells and it is therefore sufficient to consider only a single unit cell of the MAM and the coupled fluid half spaces with the Bloch-Floquet boundary conditions as shown in Fig. 2.5. Following the nondimensionalization procedure for the structural MAM model from Section 2.1.1, the reradiated acoustic field in both half-spaces is expressed in terms of the nondimensional acoustic potential function φ_{rr}, which is governed by the Helmholtz equation

$$\varphi_{\mathrm{rr},\xi\xi} + \Lambda^2\varphi_{\mathrm{rr},\eta\eta} + \varphi_{\mathrm{rr},\zeta\zeta} + \kappa_0^2\varphi_{\mathrm{rr}} = 0 \tag{2.40}$$

with the periodic boundary conditions

$$\varphi_{\mathrm{rr}}(\xi + p, \eta + q, \zeta) = \varphi_{\mathrm{rr}}(\xi, \eta, \zeta)\mathrm{e}^{-\mathrm{i}\left(\kappa_\xi p + \kappa_\eta q\right)}. \tag{2.41}$$

In Eq. (2.40), $\kappa_0 = k_0 L_x$ is the dimensionless acoustic wave number, which is related to the dimensionless speed of sound $\varsigma_0 = c_0/\sqrt{T_{\mathrm{m}}/m''_{\mathrm{m}}}$ by $\kappa_0 = \Omega/\varsigma_0$. The general solution of Eq. (2.40) under the periodic boundary conditions specified in Eq. (2.41) consists of the superposition of the fluid cavity modes, each given by the product of a lateral mode function

$$\Psi_{rs} = \mathrm{e}^{-\mathrm{i}(\kappa_r\xi + \kappa_s\eta)}, \tag{2.42}$$

where $\kappa_r = \kappa_\xi + 2\pi r$, $r = \ldots, -1, 0, 1, \ldots$, and $\kappa_s = \kappa_\eta + 2\pi s$, $s = \ldots, -1, 0, 1, \ldots$, and a plane wave propagating in positive ζ-direction. Thus, the reradiated acoustic potential function is approximated by truncating the superposition of the fluid cavity modes, i.e.

$$\begin{aligned}\varphi_{\mathrm{rr}}(\xi, \eta, \zeta) &\approx \sum_{r=-N_x^{(\varphi)}}^{N_x^{(\varphi)}} \sum_{s=-N_y^{(\varphi)}}^{N_y^{(\varphi)}} a_{rs} \Psi_{rs} \mathrm{e}^{-\mathrm{i}\kappa_{rs}\zeta} \\ &= \sum_{rs} a_{rs} \Psi_{rs} \mathrm{e}^{-\mathrm{i}\kappa_{rs}\zeta}.\end{aligned} \tag{2.43}$$

Like the expansion for u in Eq. (2.6), the approximate relationship in Eq. (2.43) becomes more accurate for higher values of $N_x^{(\varphi)}$ and $N_y^{(\varphi)}$. In most cases it is sufficient to consider only fluid modes up to an order of ten, because the higher-order fluid modes are strongly evanescent and do not contribute much to the sound radiation of MAMs. It follows from the dispersion relation that the ζ-component of the dimensionless wave number in Eq. (2.43) is given by

$$\kappa_{rs} = \pm\sqrt{\kappa_0^2 - \kappa_r^2 - \Lambda^2 \kappa_s^2}, \tag{2.44}$$

with the positive sign for positive radicands (i.e. real κ_{rs}) and the negative sign for negative radicands (i.e. imaginary κ_{rs}) such that only physically reasonable solutions for the reradiated acoustic field are obtained.

The unknown constants a_{rs} in Eq. (2.43) have to be determined from the vibro-acoustic coupling condition between the MAM and the fluid. For this, the nondimensional particle displacement amplitude vector field $\mathbf{u}_{\mathrm{rr}}$ inside the fluid half space adjacent to the MAM follows from

the gradient of the potential function φ_{rr}, i.e.

$$\mathbf{u}_{\mathrm{rr}} = \begin{pmatrix} u_{\xi,\mathrm{rr}} \\ u_{\eta,\mathrm{rr}} \\ u_{\zeta,\mathrm{rr}} \end{pmatrix} = \frac{1}{\mathrm{i}\Omega} \begin{pmatrix} \varphi_{\mathrm{rr},\xi} \\ \Lambda\varphi_{\mathrm{rr},\eta} \\ \varphi_{\mathrm{rr},\zeta} \end{pmatrix}. \tag{2.45}$$

The continuity condition requires the MAM displacement amplitude u and the ζ-component of the fluid particle displacement $u_{\zeta,\mathrm{rr}}$ to be equal at the MAM-fluid interface. With the series representations of u and φ_{rr} given in Eqs. (2.6) and (2.43), respectively, the following equation for the determination of the constants a_{rs} results:

$$\sum_{mn} c_{mn}\Phi_{mn} = -\frac{1}{\Omega}\sum_{rs} \kappa_{rs}a_{rs}\Psi_{rs}. \tag{2.46}$$

A weak form of Eq. (2.46) is obtained by employing the Galerkin method with the complex conjugates of the lateral fluid mode functions $\Psi^*_{r's'}$ as weighting functions. After surface integration over the MAM, the resulting approximate relationship is given by

$$\sum_{mn} \langle \Psi^*_{rs}, \Phi_{mn} \rangle \, c_{mn} = -\frac{1}{\Omega}\kappa_{rs}a_{rs}. \tag{2.47}$$

This can be rewritten using matrix notation as

$$\mathbf{a} = -\Omega\mathbf{K}^{-1}\mathbf{R}^{\mathrm{H}}\mathbf{c}, \tag{2.48}$$

where the elements of the vector $\mathbf{a} \in \mathbb{C}^{N^{(\varphi)}}$ correspond to the modal amplitudes a_{rs} of the reradiated acoustic field with $N^{(\varphi)} = (1+2N_x^{(\varphi)}) \cdot (1 + 2N_y^{(\varphi)})$ being the total number of acoustic modes considered in the series representation in Eq. (2.43). $\mathbf{K} = (\kappa_{rsr's'}) \in \mathbb{C}^{N^{(\varphi)}\times N^{(\varphi)}}$ is a diagonal matrix containing the ζ-components of the modal wave numbers, i.e.

$$\kappa_{rsr's'} = \begin{cases} \pm\sqrt{\kappa_0^2 - \kappa_r^2 - \Lambda^2\kappa_s^2} & \text{if } r = r' \wedge s = s' \\ 0 & \text{else,} \end{cases} \tag{2.49}$$

and $\mathbf{R}^{\mathrm{H}}$ denotes the conjugate transpose of $\mathbf{R} = (r_{mnrs}) \in \mathbb{C}^{N \times N^{(\varphi)}}$, which is given by

$$r_{mnrs} = 2mn\pi^2 \frac{(-1)^m \mathrm{e}^{-\mathrm{i}\kappa_\xi} - 1}{\kappa_r^2 - m^2\pi^2} \frac{(-1)^n \mathrm{e}^{-\mathrm{i}\kappa_\eta} - 1}{\kappa_s^2 - n^2\pi^2}. \tag{2.50}$$

The nondimensional reradiated acoustic pressure field is derived from the potential function φ_{rr} via

$$\beta_{\mathrm{rr}} = -\mathrm{i}\kappa_0 \mathcal{Z}_0 \varphi_{\mathrm{rr}}, \tag{2.51}$$

with the nondimensional characteristic impedance defined as $\mathcal{Z}_0 = Z_0 L_x / \sqrt{m''_{\mathrm{m}} T_{\mathrm{m}}}$. Since the elements of the reradiated pressure vector $\boldsymbol{\beta}_{\mathrm{rr}} = (\beta_{\mathrm{rr},mn}) \in \mathbb{C}^N$ in Eq. (2.37) are given by

$$\beta_{\mathrm{rr},mn} = \langle \Phi_{mn}, \beta_{\mathrm{rr}}(\xi, \eta, 0) \rangle \,, \tag{2.52}$$

the substitution of the series representation of φ_{rr} in Eq. (2.43) into Eq. (2.51) yields

$$\beta_{\mathrm{rr},mn} = -\mathrm{i}\kappa_0 \mathcal{Z}_0 \sum_{rs} \langle \Phi_{mn}, \Psi_{rs} \rangle \, a_{rs}, \tag{2.53}$$

which can be written as

$$\boldsymbol{\beta}_{\mathrm{rr}} = -\mathrm{i}\kappa_0 \mathcal{Z}_0 \mathbf{R}\mathbf{a}. \tag{2.54}$$

Substituting Eq. (2.48) for $\mathbf{a}$ finally yields the following expression for $\boldsymbol{\beta}_{\mathrm{rr}}$, which is independent of the fluid modes amplitude vector $\mathbf{a}$:

$$\boldsymbol{\beta}_{\mathrm{rr}} = \mathrm{i}\Omega\kappa_0 \mathcal{Z}_0 \mathbf{R}\mathbf{K}^{-1}\mathbf{R}^{\mathrm{H}}\mathbf{c}. \tag{2.55}$$

Inserting this expression into Eq. (2.37) and rearranging the system of equations (2.27) results in a system of equations for the fully coupled vibro-acoustic problem:

$$\begin{bmatrix} \mathbf{C} + \mathrm{i}\Omega\boldsymbol{\Xi} - \Omega^2\mathbf{I} & \mathbf{0} & -\mathbf{L} \\ \mathbf{0} & -\Omega^2\mathbf{I} & \mathbf{Q} \\ -\mathbf{L}^{\mathrm{T}} & \mathbf{Q}^{\mathrm{T}} & \mathbf{0} \end{bmatrix} \begin{pmatrix} \mathbf{c} \\ \mathbf{u}_{\mathrm{M}} \\ \boldsymbol{\gamma} \end{pmatrix} = 2\beta_{\mathrm{i}0} \begin{pmatrix} \mathbf{b} \\ \mathbf{0} \\ \mathbf{0} \end{pmatrix}, \tag{2.56}$$

where the dimensionless radiation impedance matrix of the MAM unit cell

$$\mathbf{\Xi} = 2\kappa_0 \mathcal{Z}_0 \mathbf{R}\mathbf{K}^{-1}\mathbf{R}^{\mathrm{H}} \tag{2.57}$$

has been introduced. In terms of the modal formulation from Section 2.1.2, the modal system of equations (2.32) is thus given by

$$\left(\hat{\mathbf{\Lambda}} + \mathrm{i}\Omega\hat{\mathbf{\Xi}} - \Omega^2\mathbf{I}\right)\hat{\mathbf{c}} = 2\beta_{\mathrm{i}0}\hat{\mathbf{b}}, \tag{2.58}$$

where $\hat{\mathbf{\Xi}} = \hat{\mathbf{V}}_c^{\mathrm{T}}\mathbf{\Xi}\hat{\mathbf{V}}_c$ is the modal radiation impedance matrix and $\hat{\mathbf{b}} = \hat{\mathbf{V}}_c^{\mathrm{T}}\mathbf{b}$.

In order to obtain the transmission coefficient τ from Eq. (1.1), the incident and transmitted sound powers W_{i} and W_{t} have to be calculated. Since the incident sound field is a plane acoustic wave with amplitude $\hat{P}_{\mathrm{i}0}$ and incidence angle θ_{i}, the former is given by

$$W_{\mathrm{i}} = \frac{L_x L_y}{2Z_0}\hat{P}_{\mathrm{i}0}^2 \cos\theta_{\mathrm{i}} \tag{2.59}$$

or, written in nondimensional form, by

$$\Pi_{\mathrm{i}} = \frac{W_{\mathrm{i}}}{\sqrt{T_{\mathrm{m}}^3/m''_{\mathrm{m}}}L_x} = \frac{\beta_{\mathrm{i}0}^2}{2\Lambda\mathcal{Z}_0}\cos\theta_{\mathrm{i}}. \tag{2.60}$$

The transmitted sound power, on the other hand, is equal to the reradiated sound power, which can be obtained from

$$W_{\mathrm{t}} = \frac{1}{2}\iint_S \mathrm{Re}\left\{\hat{v}^*(x,y)\hat{P}_{\mathrm{rr}}(x,y,0)\right\}\,\mathrm{d}y\,\mathrm{d}x, \tag{2.61}$$

where $\hat{v}^* = -\mathrm{i}\omega\hat{w}^*$ is the complex conjugate of the MAM velocity amplitude and $\hat{P}_{\mathrm{rr}}$ is the reradiated acoustic pressure amplitude field

[22, p. 10]. Using the nondimensionalizations introduced above, this can be rewritten as

$$\mathit{\Pi}_\mathrm{t} = \frac{W_\mathrm{t}}{\sqrt{T_\mathrm{m}^3/m_\mathrm{m}''}L_x} = \frac{\mathit{\Omega}}{2\mathit{\Lambda}} \int_0^1 \int_0^1 \mathrm{Im}\left\{u^*(\xi,\eta)\beta_\mathrm{rr}(\xi,\eta,0)\right\} \,\mathrm{d}\eta\,\mathrm{d}\xi. \quad (2.62)$$

With Eqs. (2.6) and (2.51) as well as the series expansion of φ_rr in Eq. (2.43), this becomes

$$\begin{aligned} \mathit{\Pi}_\mathrm{t} &= -\frac{\mathit{\Omega}\kappa_0\mathcal{Z}_0}{2\mathit{\Lambda}} \mathrm{Re}\left\{\sum_{mn} c_{mn}^* \sum_{rs} \langle \mathit{\Phi}_{mn}, \mathit{\Psi}_{rs}\rangle \, a_{rs}\right\} \\ &= -\frac{\mathit{\Omega}\kappa_0\mathcal{Z}_0}{2\mathit{\Lambda}} \mathrm{Re}\left\{\mathbf{c}^\mathrm{H}\mathbf{R}\mathbf{a}\right\}. \end{aligned} \quad (2.63)$$

Using the solution for the coefficient vector $\mathbf{a}$ in Eq. (2.48) and the definition of the nondimensional radiation impedance matrix $\mathbf{\Xi}$ from Eq. (2.57), the final expression for the radiated power is obtained as

$$\mathit{\Pi}_\mathrm{t} = \frac{\mathit{\Omega}^2\kappa_0\mathcal{Z}_0}{2\mathit{\Lambda}} \mathrm{Re}\left\{\mathbf{c}^\mathrm{H}\mathbf{R}\mathbf{K}^{-1}\mathbf{R}^\mathrm{H}\mathbf{c}\right\} = \frac{\mathit{\Omega}^2}{4\mathit{\Lambda}}\mathbf{c}^\mathrm{H}\mathrm{Re}\left\{\mathbf{\Xi}\right\}\mathbf{c}. \quad (2.64)$$

Thus, using Eqs. (2.60) and (2.64), the transmission coefficient τ_{θ_i} of the MAM unit cell is given by

$$\tau_{\theta_\mathrm{i}} = \frac{\mathit{\Pi}_\mathrm{t}}{\mathit{\Pi}_\mathrm{i}} = \frac{\mathit{\Omega}^2\mathcal{Z}_0}{2\cos\theta_\mathrm{i}} \frac{\mathbf{c}^\mathrm{H}\mathrm{Re}\left\{\mathbf{\Xi}\right\}\mathbf{c}}{\beta_{\mathrm{i}0}^2} = \frac{2\mathit{\Omega}^2\mathcal{Z}_0}{\cos\theta_\mathrm{i}} \widetilde{\mathbf{c}}^\mathrm{H}\mathrm{Re}\left\{\mathbf{\Xi}\right\}\widetilde{\mathbf{c}}, \quad (2.65)$$

where $\widetilde{\mathbf{c}} = \mathbf{c}/(2\beta_{\mathrm{i}0})$ contains the membrane modal participation factors normalized by the excitation amplitude. Expressed in terms of the normalized MAM modal participation factors $\widetilde{\hat{\mathbf{c}}} = \hat{\mathbf{c}}/(2\beta_{\mathrm{i}0})$, Eq. (2.65) is given by

$$\tau_{\theta_\mathrm{i}} = \frac{2\mathit{\Omega}^2\mathcal{Z}_0}{\cos\theta_\mathrm{i}} \widetilde{\hat{\mathbf{c}}}^\mathrm{H}\mathrm{Re}\left\{\hat{\mathbf{\Xi}}\right\}\widetilde{\hat{\mathbf{c}}}. \quad (2.66)$$

2.1.4. Low-frequency approximation

At low frequencies, the acoustic wavelength is significantly larger than the lateral dimensions L_x and L_y of the MAM so that the dimensionless wave number κ_0 is much smaller than unity ($\kappa_0 = k_0 L_x \ll 1$). Therefore, the ζ-components of the modal wave numbers in the reradiated acoustic field κ_{rs}, as given in Eq. (2.44), are purely imaginary with $\kappa_{rs} \approx -\mathrm{i}2\pi\sqrt{r^2 + \Lambda^2 s^2}$ except in case of the zero-order or plane wave mode, where $r = s = 0$. The wave number of this particular mode is given by $\kappa_{00} = \kappa_0 \cos\theta_\mathrm{i}$, which corresponds to the ζ-component of the incident plane wave number κ_ζ. This means that in such cases only a plane wave is radiated by the MAM unit cell into the far field and the higher-order modes are evanescent waves, which do not contribute to the radiated sound power. Therefore, the sound transmission through the MAM unit cell can be quantified using a complex plane wave acoustic transmission factor $\tilde{t}_{\theta_\mathrm{i}} = \hat{P}_\mathrm{t}/\hat{P}_\mathrm{i0}$, which relates the complex amplitude of the transmitted plane wave $\hat{P}_\mathrm{t}$ to the amplitude of the incident plane wave $\hat{P}_\mathrm{i0}$. With Eqs. (2.43) and (2.51), the nondimensional pressure amplitude of the reradiated plane acoustic wave is given by $\beta_\mathrm{t} = -\mathrm{i}\kappa_0 \mathcal{Z}_0 a_{00}$. a_{00} can be obtained from Eq. (2.48) as $a_{00} = -\Omega \mathbf{r}_{00}^\mathrm{H}\mathbf{c}/(\kappa_0 \cos\theta_\mathrm{i})$, where $\mathbf{r}_{00}$ is the corresponding column of $\mathbf{R}$ with $r = s = 0$. Comparing $\mathbf{r}_{00}$, as defined in Eq. (2.50), and the definition of the excitation vector $\mathbf{b}$ in Eq. (2.38) reveals that $\mathbf{r}_{00} = \mathbf{b}$. Thus, the transmission factor $\tilde{t}_{\theta_\mathrm{i}}$ is given by

$$\tilde{t}_{\theta_\mathrm{i}} = \frac{\beta_\mathrm{t}}{\beta_\mathrm{i0}} = -\mathrm{i}\kappa_0 \mathcal{Z}_0 \frac{a_{00}}{\beta_\mathrm{i0}} = \frac{2\mathcal{Z}_0 \mathrm{i}\Omega}{\cos\theta_\mathrm{i}} \mathbf{b}^\mathrm{H} \widetilde{\mathbf{c}}. \tag{2.67}$$

The transmission coefficient τ_{θ_i} follows from the squared magnitude of the transmission factor, i.e.

$$\tau_{\theta_\mathrm{i}} = \tilde{t}_{\theta_\mathrm{i}} \tilde{t}^*_{\theta_\mathrm{i}} = \frac{4\mathcal{Z}_0^2 \Omega^2}{\cos^2\theta_\mathrm{i}} \widetilde{\mathbf{c}}^\mathrm{H} \mathbf{b}\mathbf{b}^\mathrm{H} \widetilde{\mathbf{c}}, \tag{2.68}$$

which reduces to Eq. (2.65) considering that, for $\kappa_0 \ll 1$, the real part of $\boldsymbol{\Xi}$ is given by

$$\mathrm{Re}\left\{\boldsymbol{\Xi}\right\} = \frac{2\mathcal{Z}_0}{\cos\theta_\mathrm{i}}\mathbf{r}_{00}\mathbf{r}_{00}^\mathrm{H} = \frac{2\mathcal{Z}_0}{\cos\theta_\mathrm{i}}\mathbf{b}\mathbf{b}^\mathrm{H}. \tag{2.69}$$

A considerably simplified expression for the transmission factor $\tilde{t}_{\theta_\mathrm{i}}$ in the low-frequency limit can be derived from Eq. (2.67). As shown in Appendix C, $\tilde{t}_{\theta_\mathrm{i}}$ can be expressed in analogy to the mass-law as

$$\tilde{t}_{\theta_\mathrm{i}} \approx \frac{1}{1 + \frac{\mathrm{i}\Omega\cos\theta_\mathrm{i}}{2\mathcal{Z}_0}\mu''_\mathrm{eff}}, \tag{2.70}$$

where μ''_eff is the nondimensional effective surface mass density of the unit cell. This quantity is defined as

$$\mu''_\mathrm{eff} \approx \frac{1}{-\Omega^2\mathbf{b}_{0^\circ}^\mathrm{T}\widetilde{\mathbf{c}}_{0^\circ,\mathrm{vac}}}, \tag{2.71}$$

where $\mathbf{b}_{0^\circ}$ and $\widetilde{\mathbf{c}}_{0^\circ,\mathrm{vac}}$ are the vectors $\mathbf{b}$ and $\widetilde{\mathbf{c}}$, respectively, calculated for normal incidence (see Eq. (C.16)) and considering only the in vacuo response of the MAM unit cell (i.e. setting $\boldsymbol{\Xi} = \mathbf{0}$ in Eq. (2.56)).

Eq. (2.71) shows that, as long as the condition $\kappa_0 \ll 1$ is fulfilled, the effective surface mass density of the MAM unit cell is independent of the incidence angle θ_i and can be readily obtained from the MAM response under spatially uniform pressure excitation, e.g. in an experimental setup with an impedance tube [3]. Furthermore, Eq. (2.71) also follows from the definition of the effective surface mass density originally proposed by Yang et al. [107]. This definition is deduced from Newton's second law as

$$\mu''_\mathrm{eff} = \frac{1}{m''_\mathrm{m}}\frac{\langle\hat{P}_\mathrm{i}\rangle}{-\omega^2\langle\hat{w}\rangle}, \tag{2.72}$$

where $\langle \hat{P}_\mathrm{i} \rangle$ and $\langle \hat{w} \rangle$ denote the average of the incident pressure field and MAM displacement along the MAM surface, respectively. For normal incidence $\hat{P}_\mathrm{i} = \hat{P}_\mathrm{i0} = \text{const.}$ and using the dimensionless quantities introduced above, Eq. (2.72) yields

$$\mu''_\mathrm{eff} = \frac{\beta_\mathrm{i0}}{-\Omega^2 \sum\limits_{mn} c_{0^\circ,mn} \langle \Phi_{mn} \rangle}, \tag{2.73}$$

which reduces to Eq. (2.71) considering that the surface average of the membrane eigenfunctions Φ_{mn} is equal to $\langle \Phi_{mn} \rangle = b_{0^\circ,mn}$.

The results in Eqs. (2.70) and (2.71) imply some important facts about the acoustic performance of MAMs in the long wavelength limit: First, the nondimensional effective surface mass density μ''_eff of the MAM is independent of the direction of the incident plane acoustic wave. An explanation for this is that at long wavelengths with $\kappa_0 \ll 1$, even for grazing incidence (i.e. $\theta_\mathrm{i} = 90°$) the pressure distribution over the MAM surface is approximately uniform. Secondly, only the piston-like part of the vibrational MAM response (i.e. the surface average of the MAM displacement amplitude $\langle \hat{w} \rangle$) couples to the plane waves which are reradiated into the far field. Thus, if $\langle \hat{w} \rangle = \mathbf{b}_{0^\circ}^\mathrm{T} \widetilde{\mathbf{c}}_{0^\circ,\mathrm{vac}} = 0$ for a certain frequency Ω_P, then the effective surface mass density of the MAM becomes infinitely large and no sound is transmitted through the MAM. These transmission loss peak frequencies correspond to the frequencies Ω_P for which the rank of the Rosenbrock system matrix

$$\mathbf{P}(\Omega_\mathrm{P}) = \begin{bmatrix} \mathbf{A}_\mathrm{vac} & -\mathbf{y}_{0^\circ} \\ -\mathbf{y}_{0^\circ}^\mathrm{T} & 0 \end{bmatrix} \tag{2.74}$$

drops from its normal value (the quantities $\mathbf{A}_\mathrm{vac}$ and $\mathbf{y}_{0^\circ}$ are defined in Appendix C). Using the modal form in Eq. (2.58), the Rosenbrock system matrix can be transformed into modal coordinates as

$$\hat{\mathbf{P}}(\Omega_\mathrm{P}) = \begin{bmatrix} \hat{\mathbf{\Lambda}} - \Omega_\mathrm{P}^2 \mathbf{I} & -\hat{\mathbf{b}}_{0^\circ} \\ -\hat{\mathbf{b}}_{0^\circ}^\mathrm{T} & 0 \end{bmatrix}. \tag{2.75}$$

The derivation of the low-frequency approximation in this section shows that the well-known acoustic properties of MAMs in the special case of normal incidence (see Fig. 1.4) can also be straightforwardly adapted to the oblique incidence case. This means that the eigenfrequencies and transmission loss peak frequencies of the MAM are not affected by the incident sound field, as long as the acoustic wavelength is significantly larger than the MAM unit cell. The magnitude of the transmission loss TL, however, depends on the incident sound field. The $\cos\theta_\mathrm{i}$-term in Eq. (2.70) indicates that higher angles of incidence reduce the TL of the MAM. For example, at $\theta_\mathrm{i} = 60°$ the transmission loss is reduced by $10\lg(\cos^2 60°) \approx -6$ dB, assuming that $\mathrm{i}\Omega\mu''_\mathrm{eff} \gg 2\mathcal{Z}_0$. This dependence is the same as for thin partitions with a constant surface mass density of m'' [61].

Concerning the computational modeling of MAMs, the low-frequency approximation provides a much more efficient method for calculating the sound transmission through MAMs. The effective surface mass density μ''_eff needs to be calculated only once per frequency using Eq. (2.71), which requires the solution of either the sparse system of equations (2.56) or the modal form in Eq. (2.58) with $\boldsymbol{\Xi}$ set to zero and $\theta_\mathrm{i} = 0°$. The transmission coefficient τ_{θ_i} can then be calculated for any incidence angle θ_i using the transmission factor with the simple relation in Eq. (2.70). If the low-frequency approximation cannot be used, then Eqs. (2.56) or (2.58) need to be solved with the (fully populated) radiation impedance matrix $\boldsymbol{\Xi}$ and the excitation vector $\mathbf{b}$ recalculated for each frequency Ω and angle of incidence θ_i.

When comparing the properties of the proposed MAM unit cell model to the two different types of existing analytical MAM models (Zhang et al. [112] and Chen et al. [10, 11]), it can be seen that the proposed model offers certain advantages: First, the MAM model in this work takes into account the rigidity of the added masses, which the model by Zhang et al. [112] does not. Due to the coupling between

the membrane and the masses, this comes at the cost of a larger system of equations (2.56). But since Eq. (2.56) still is a linear system of equations, there are many methods available to efficiently compute the solution. Furthermore, the model by Zhang et al. [112] considers only rectangular shaped added masses and does not exhibit asymptotic convergence for large number of membrane eigenmodes in the expansion of the MAM displacement field. This makes it difficult to apply the model by Zhang et al. [112] to MAM unit cells for which the TL-curves are not known a-priori. Secondly, the MAM model by Chen et al. [10, 11], like the analytical model in this work, does take into account the mass rigidity and allows for arbitrarily shaped masses. However, implementing and solving the resulting non-linear eigenvalue problem is more difficult than solving the well-known linear eigenvalue problem in Eq. (2.28). Particular care needs to be taken in the model by Chen et al. [10, 11] to identify all relevant eigenfrequencies within the frequency range of interest. Furthermore, the vibro-acoustic coupling in [10, 11] relies on computationally expensive numerical integrations involving Green's functions. The radiation impedance matrix in this work can be obtained directly using Eq. (2.57) and no numerical integrations are required. In summary, this comparison shows that the proposed analytical model for MAM unit cells indeed combines the strengths of the MAM models by Zhang et al. [112] and Chen et al. [10, 11], as claimed in the beginning of this section. In the following section it will be shown, that the proposed MAM unit cell model can be further developed to enable the efficient calculation of the sound transmission properties of panels consisting of multiple MAM unit cells.

2.2. Analytical model for MAM arrays

The analytical model in the previous section has been derived for a MAM unit cell as part of an infinitely extending grid of MAMs with

equal properties. However, it can be expected that a MAM array with finite dimensions (e.g. several square meters) behaves differently than the infinite array. This is particularly possible for varying MAM unit cell properties, either by design or because of tolerances in manufacturing.

In the literature, most investigations of MAMs have been performed on individual MAM unit cells under normal incidence (e.g. [52, 63, 64, 107]). In principle, this setup is equivalent to the infinite array considered in the previous section. Multi-celled panels with MAMs have been primarily investigated using the modified impedance tube technique [30]. However, with this experimental method only a small area much smaller than the acoustic wavelength is acoustically excited instead of the whole panel surface (e.g. [59, 108]). Some investigations have considered multi-celled MAM arrays with the whole structure subjected to the incident sound field [65, 66, 113]. The investigated test samples, however, were 2-by-2 MAM arrays with dimensions that were still much smaller than the acoustic wavelength. Blevins [7] investigated the normal incidence sound transmission loss of baffled MAM arrays using an impedance-mobility model. This model, however, is based upon the simplified model by Zhang et al. [112] that does not take into account the rigidity of the added mass, which has previously been shown to be important to accurately predict the resonance frequencies of MAMs [13, 35, 98]. Furthermore, the analytical model by Zhang et al. [112] is restricted to MAMs with a single rectangular shaped mass, which reduces the applicability of the model. In addition to that, the MAM unit cells in the MAM array model in [7] are not acoustically coupled to each other. This, however, has been shown to be important for certain MAM array configurations [65]. Accurate analytical investigations of finite MAM arrays with total dimensions that are comparable or even exceed the acoustic wavelength are currently not available in the literature. Thus, for practical applications, the analytical model developed

in the previous section should be extended to account for the finite dimensions of a multi-celled MAM panel with possibly varying MAM unit cell properties.

The present section is structured as follows: The first subsection provides the governing equations for the vibrations of a finite array of different MAM unit cells. The fluid-structure coupling of the baffled MAM array is introduced in the subsequent subsection. Finally, Section 2.2.3 provides a low-frequency approximation based upon the effective surface mass density of the MAM unit cells to calculate the transmission loss of the array in the long wavelength limit.

2.2.1. Governing equations

For the analytical modeling of the finite multi-celled MAM array, the panel, as shown in Fig. 2.6, is assumed to be planar and part of an infinite rigid baffle separating two fluid half spaces. A global Cartesian coordinate system (x, y, z) is defined with the origin in one corner of the array and the x- and y-axes pointing along the edges of the panel. Similar to the numbering scheme introduced in Section 2.1.3, each MAM unit cell inside the array is uniquely identified by two indices $p = 1, \ldots, N_{\mathrm{C}x}$ and $q = 1, \ldots, N_{\mathrm{C}y}$, where $N_{\mathrm{C}x}$ and $N_{\mathrm{C}y}$ denote the number of MAM cells in x- and y-direction, respectively. Thus, the total number of MAM unit cells is given by $N_{\mathrm{C}} = N_{\mathrm{C}x} N_{\mathrm{C}y}$. The properties of each cell correspond to the definitions illustrated in Fig. 2.1 for the single unit cell. It is assumed that all cells have equal dimensions with the edge lengths L_x and L_y so that the overall length and width of the array are given by $N_{\mathrm{C}x} L_x$ and $N_{\mathrm{C}y} L_y$, respectively. All MAM cell edges (i.e. the outer and interior edges) are assumed to be simply supported.

As indicated in Fig. 2.6, each cell is provided with a local coordinate system $(\tilde{x}_{pq}, \tilde{y}_{pq}, z)$ with the axes being parallel to the axes of the global

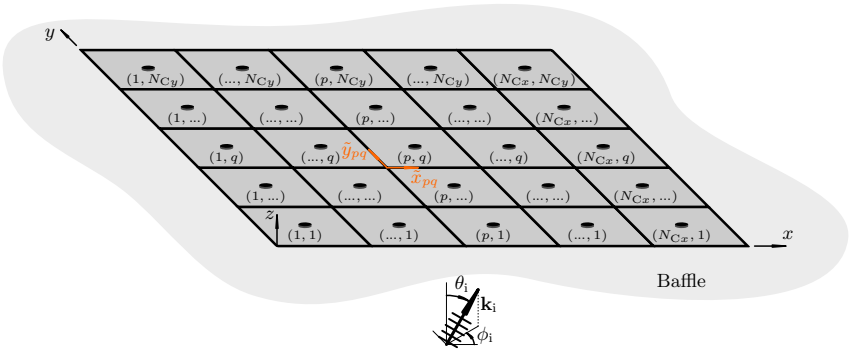

Figure 2.6: Basic definitions for the baffled MAM array under the acoustic excitation of a plane wave.

coordinate system axes and the origin located at (in global coordinates) $x^*_{pq} = (p-1)L_x$ and $y^*_{pq} = (q-1)L_y$. The local and global coordinate systems are related by

$$x = (p-1)L_x + \tilde{x}_{pq} \quad \text{and} \tag{2.76a}$$

$$y = (q-1)L_y + \tilde{y}_{pq}. \tag{2.76b}$$

Thus, in terms of the local coordinate system, each individual MAM unit cell is governed by Eq. (2.2). The edges of the MAMs are assumed to be decoupled from each other and, therefore, the only coupling between the unit cells occurs from the acoustic pressure amplitude difference $\Delta\hat{P}$ due to the reradiated sound fields of the metamaterials. Apart from that, each cell is completely uncoupled and can be analyzed in the same way as the single cell in Section 2.1.1 using the point matching approach and membrane mode series expansion. The membrane material is assumed to be the same for each unit cell, except for the membrane prestress resultant $T_{\mathrm{m},pq}$, which is allowed to vary between cells, for example to account for stress variations due to man-

ufacturing tolerances. In the nondimensionalization of the governing equations, a reference stress resultant $T_{\mathrm{m,ref}}$ is used instead of $T_{\mathrm{m},pq}$ to obtain consistent dimensionless parameters for all cells. Thus, adhering to the same derivation process as in Section 2.1.1, the following system of equations is obtained:

$$\begin{bmatrix} \mathbf{C}_{pq} - \Omega^2\mathbf{I} & \mathbf{0} & -\mathbf{L}_{pq} \\ \mathbf{0} & -\Omega^2\mathbf{I} & \mathbf{Q}_{pq} \\ -\mathbf{L}_{pq}^{\mathrm{T}} & \mathbf{Q}_{pq}^{\mathrm{T}} & \mathbf{0} \end{bmatrix} \begin{pmatrix} \mathbf{c}_{pq} \\ \mathbf{u}_{\mathrm{M},pq} \\ \boldsymbol{\gamma}_{pq} \end{pmatrix} = \begin{pmatrix} \boldsymbol{\Delta}\boldsymbol{\beta}_{pq} \\ \mathbf{0} \\ \mathbf{0} \end{pmatrix}, \tag{2.77}$$

where the double index pq denotes that the corresponding matrices and vectors are attributed to the MAM unit cell (p, q). Eq. (2.77) is a $(N_{pq} + 3 + I_{pq})$ by $(N_{pq} + 3 + I_{pq})$ system of equations, where N_{pq} and I_{pq} denote that the number of membrane modes and matching points, respectively, can be chosen differently for each unit cell. The elements of the membrane stiffness matrix $\mathbf{C}_{pq} = (\varkappa^{(pq)}_{mnm'n'}) \in \mathbb{R}^{N_{pq}\times N_{pq}}$ are given by

$$\varkappa^{(pq)}_{mnm'n'} = \begin{cases} \tau_{pq}\widetilde{\varkappa}_{mn} + \Xi\widetilde{\varkappa}^2_{mn} & \text{if } m = m' \wedge n = n' \\ 0 & \text{else,} \end{cases} \tag{2.78}$$

where $\tau_{pq} = T_{\mathrm{m},pq}/T_{\mathrm{m,ref}}$ is the nondimensional cell prestress resultant of the unit cell. The matrices $\mathbf{Q}_{pq}$ and $\mathbf{L}_{pq}$ are obtained using Eqs. (2.20) and (2.23) with the specified matching point coordinates.

The eigenmode extraction procedure described in Section 2.1.2 can be performed for each MAM unit cell (p, q) separately. In this way it is possible to obtain the reduced modal form of Eq. (2.77) given by

$$\left(\hat{\boldsymbol{\Lambda}}_{pq} - \Omega^2\mathbf{I}\right)\hat{\mathbf{c}}_{pq} = \boldsymbol{\Delta}\hat{\boldsymbol{\beta}}_{pq}, \tag{2.79}$$

which is the analog of Eq. (2.32) for each MAM unit cell of the array.

2.2.2. Fluid-structure coupling

As shown in Fig. 2.6, the MAM array is excited by an obliquely incident plane wave with pressure amplitude $\hat{P}_{\mathrm{i}0}$ and wave vector $\mathbf{k}_{\mathrm{i}}$ given in Eq. (2.33). The nondimensional form of the acoustic pressure amplitude difference $\Delta\beta$ acting on the whole array can again be separated into a blocked pressure part β_{bl} and a reradiated pressure part β_{rr}, as given in Eq. (2.36). In terms of the nondimensional local coordinate system $(\tilde{\xi}_{pq}, \tilde{\eta}_{pq}, \zeta)$ following the coordinate transformation in Eq. (2.76), Eq. (2.36) can be expressed as

$$\Delta\beta(\tilde{\xi}_{pq}, \tilde{\eta}_{pq}) = 2\beta_{\mathrm{i}0}\varepsilon_{pq}\mathrm{e}^{-\mathrm{i}\left(\kappa_\xi\tilde{\xi}_{pq}+\kappa_\eta\tilde{\eta}_{pq}\right)} - 2\beta_{\mathrm{rr}}(\tilde{\xi}_{pq}, \tilde{\eta}_{pq}, 0), \tag{2.80}$$

where $\varepsilon_{pq} = \mathrm{e}^{-\mathrm{i}(p-1)\kappa_\xi}\mathrm{e}^{-\mathrm{i}(q-1)\kappa_\eta}$ corresponds to the phase lag of the incident sound field in the cell (p, q) relative to the cell $(1, 1)$. Consequently, the vector $\boldsymbol{\Delta\beta}_{pq}$ in Eq. (2.77) is given by

$$\boldsymbol{\Delta\beta}_{pq} = 2\beta_{\mathrm{i}0}\varepsilon_{pq}\mathbf{b} - 2\boldsymbol{\beta}_{\mathrm{rr},pq}, \tag{2.81}$$

with the elements of $\mathbf{b}$ obtained from Eq. (2.38).

The reradiated pressure vector $\boldsymbol{\beta}_{\mathrm{rr},pq} = (\beta^{(pq)}_{\mathrm{rr},mn}) \in \mathbb{C}^{N_{pq}}$, on the other hand, is calculated using the surface integral of the membrane eigenfunctions $\Phi^{(pq)}_{mn}$ and the reradiated pressure field β_{rr} over the unit cell surface:

$$\begin{aligned}\beta^{(pq)}_{\mathrm{rr},mn} &= \left\langle \Phi^{(pq)}_{mn}, \beta_{\mathrm{rr}} \right\rangle \\ &= \int_0^1\int_0^1 \Phi_{mn}(\tilde{\xi}_{pq}, \tilde{\eta}_{pq})\beta_{\mathrm{rr}}(\tilde{\xi}_{pq}, \tilde{\eta}_{pq}, 0)\,\mathrm{d}\tilde{\eta}_{pq}\,\mathrm{d}\tilde{\xi}_{pq}.\end{aligned} \tag{2.82}$$

Since the MAM array is planar and part of an infinite baffle, the reradiated pressure amplitude field $\hat{P}_{\mathrm{rr}}$ can be obtained from the MAM

displacement amplitudes $\hat{w}$ using the Rayleigh integral equation [14, p. 89]

$$\hat{P}_{\mathrm{rr}}(x,y,z) = -\rho_0\omega^2 \int_0^{N_{\mathrm{C}x}L_x} \int_0^{N_{\mathrm{C}y}L_y} w(x^\star,y^\star)G(R)\,\mathrm{d}y^\star\,\mathrm{d}x^\star, \tag{2.83}$$

with the Green's function

$$G(R) = \frac{\mathrm{e}^{-\mathrm{i}k_0R}}{2\pi R} \tag{2.84}$$

and $R = \sqrt{(x^\star-x)^2+(y^\star-y)^2+z^2}$. Using the nondimensional variables introduced above, Eq. (2.83) can be rewritten as

$$\beta_{\mathrm{rr}}(\xi,\eta,\zeta) = -\frac{\mathcal{Z}_0\kappa_0\Omega}{2\pi\Lambda} \int_0^{N_{\mathrm{C}x}} \int_0^{N_{\mathrm{C}y}} u(\xi^\star,\eta^\star)\Gamma(\Delta)\,\mathrm{d}\eta^\star\,\mathrm{d}\xi^\star, \tag{2.85}$$

where the nondimensional Green's function has been defined as $\Gamma(\Delta) = \mathrm{e}^{-\mathrm{i}\kappa_0\Delta}/\Delta$ and $\Delta = \sqrt{(\xi^\star-\xi)^2+(\eta^\star-\eta)^2/\Lambda^2+\zeta^2}$. The surface integral in Eq. (2.85) can be split up into a summation of N_{C} surface integrals over each MAM unit cell surface. Transforming the global coordinates into the local coordinate systems using Eq. (2.76), letting $\zeta = 0$, and omitting the function arguments inside the integrand yields

$$\beta_{\mathrm{rr}}(\tilde{\xi}_{pq},\tilde{\eta}_{pq},0) = -\frac{\mathcal{Z}_0\kappa_0\Omega}{2\pi\Lambda} \sum_{p'q'} \int_0^1 \int_0^1 u_{p'q'}\Gamma_{pqp'q'}\,\mathrm{d}\tilde{\eta}^\star_{p'q'}\,\mathrm{d}\tilde{\xi}^\star_{p'q'}, \tag{2.86}$$

where $u_{p'q'}$ denotes the local nondimensional vibration amplitude of the MAM unit cell (p',q'), $\Gamma_{pqp'q'} = \Gamma(\Delta_{pqp'q'})$, and

$$\Delta_{pqp'q'} = \sqrt{(\tilde{\xi}^\star_{p'q'}-\tilde{\xi}_{pq}+p'-p)^2+(\tilde{\eta}^\star_{p'q'}-\tilde{\eta}_{pq}+q'-q)^2/\Lambda^2}. \tag{2.87}$$

Inserting Eq. (2.86) into Eq. (2.82) and taking into account that the MAM vibration amplitude $u_{p'q'}$ is expanded into the membrane eigenfunctions $\Phi_{m'n'}^{(p'q')}$ as given in Eq. (2.6), results in an expression for the elements of $\boldsymbol{\beta}_{\mathrm{rr},pq}$:

$$\beta_{\mathrm{rr},mn}^{(pq)} = -\frac{\mathcal{Z}_0 \kappa_0 \Omega}{2\pi\Lambda} \sum_{p'q'} \sum_{m'n'} c_{m'n'}^{(p'q')} I_{mnm'n'}^{(pqp'q')}, \tag{2.88}$$

where $c_{m'n'}^{(p'q')}$ represents the elements of $\mathbf{c}_{p'q'}$ and $I_{mnm'n'}^{(pqp'q')}$ is a quadruple integral given by

$$I_{mnm'n'}^{(pqp'q')} = \int_0^1 \int_0^1 \int_0^1 \int_0^1 \Phi_{mn}^{(pq)} \Gamma_{pqp'q'} \Phi_{m'n'}^{(p'q')} \,\mathrm{d}\tilde{\eta}_{p'q'}^{\star} \,\mathrm{d}\tilde{\xi}_{p'q'}^{\star} \,\mathrm{d}\tilde{\eta}_{pq} \,\mathrm{d}\tilde{\xi}_{pq}. \tag{2.89}$$

A nondimensional radiation impedance matrix $\boldsymbol{\Xi}_{pqp'q'} = (\Xi_{mnm'n'}^{(pqp'q')}) \in \mathbb{C}^{N_{pq} \times N_{p'q'}}$ for the vibro-acoustic influence of the unit cell (p', q') on the unit cell (p, q) can be introduced by

$$\Xi_{mnm'n'}^{(pqp'q')} = \mathrm{i} \frac{\mathcal{Z}_0 \kappa_0}{\pi\Lambda} I_{mnm'n'}^{(pqp'q')}. \tag{2.90}$$

Thus, the vector $\boldsymbol{\beta}_{\mathrm{rr},pq}$ is finally given as

$$\boldsymbol{\beta}_{\mathrm{rr},pq} = \frac{\mathrm{i}\Omega}{2} \sum_{p'q'} \boldsymbol{\Xi}_{pqp'q'} \mathbf{c}_{p'q'}. \tag{2.91}$$

By switching the primed and unprimed indices in Eq. (2.87) it can be shown that $\Delta_{p'q'pq} = \Delta_{pqp'q'}$ and, following from the properties of the quadruple integral in Eq. (2.89), $I_{m'n'mn}^{(p'q'pq)} = I_{mnm'n'}^{(pqp'q')}$. Consequently, the nondimensional radiation impedance matrices follow the acoustic reciprocity principle with $\boldsymbol{\Xi}_{p'q'pq} = \boldsymbol{\Xi}_{pqp'q'}^{\mathrm{T}}$. The evaluation of the quadruple

integral in Eq. (2.89) has to be performed using numerical integration techniques, because currently no closed form solution to this integral exists in the literature. Despite the fact that the symmetry properties of the radiation impedance matrices can be exploited to reduce the amount of required integrations, the quadruple integral (2.89) has to be evaluated many times, especially when a high number of membrane modes, MAM unit cells, and/or frequencies are considered in the calculations. To reduce the computational effort necessary for the assembly of the radiation impedance matrices, the order of integration can be reduced using suitable coordinate transformations. For example, the method proposed by Sha et al. [81] yields a double integral for the evaluation of $I_{mnm'n'}^{(pqp'q')}$ instead of the quadruple integral in Eq. (2.89):

$$I_{mnm'n'}^{(pqp'q')} = \int_{-1}^{1}\int_{-1}^{1} s_{mm'}(\tilde{u}) s_{m'}(\tilde{v}) \mathit{\Gamma}_{pqp'q'}(\tilde{u},\tilde{v})\,\mathrm{d}\tilde{v}\,\mathrm{d}\tilde{u}, \tag{2.92}$$

with the spatial convolution function

$$s_{mm'}(\tilde{u}) = 2(\operatorname{sgn}\tilde{u})^{m+m'} \frac{m\sin(m'\pi|\tilde{u}|) - m'(-1)^{m+m'}\sin(m\pi|\tilde{u}|)}{\pi\left(m^2 - m'^2\right)}, \tag{2.93}$$

the transformed nondimensional Green's function

$$\mathit{\Gamma}_{pqp'q'}(\tilde{u},\tilde{v}) = \frac{\mathrm{e}^{-\mathrm{i}\kappa_0 \mathit{\Delta}_{pqp'q'}(\tilde{u},\tilde{v})}}{\mathit{\Delta}_{pqp'q'}(\tilde{u},\tilde{v})}, \tag{2.94}$$

and $\mathit{\Delta}_{pqp'q'}(\tilde{u},\tilde{v}) = \sqrt{(\tilde{u}+p'-p)^2 + (\tilde{v}+q'-q)^2/\mathit{\Lambda}^2}$.

Inserting Eq. (2.91) into Eq. (2.81) and assembling the system of equations (2.77) for every cell of the array from $(1,1)$ to $(N_{\mathrm{C}x}, N_{\mathrm{C}y})$ results in the fully coupled global system of equations of the array

$$\begin{bmatrix} \mathbf{C}_\mathrm{g} + \mathrm{i}\mathit{\Omega}\mathbf{\Xi}_\mathrm{g} - \mathit{\Omega}^2\mathbf{I} & \mathbf{0} & -\mathbf{L}_\mathrm{g} \\ \mathbf{0} & -\mathit{\Omega}^2\mathbf{I} & \mathbf{Q}_\mathrm{g} \\ -\mathbf{L}_\mathrm{g}^\mathrm{T} & \mathbf{Q}_\mathrm{g}^\mathrm{T} & \mathbf{0} \end{bmatrix} \begin{pmatrix} \mathbf{c}_\mathrm{g} \\ \mathbf{u}_{\mathrm{M,g}} \\ \boldsymbol{\gamma}_\mathrm{g} \end{pmatrix} = 2\beta_{\mathrm{i}0} \begin{pmatrix} \mathbf{b}_\mathrm{g} \\ \mathbf{0} \\ \mathbf{0} \end{pmatrix}, \tag{2.95}$$

with the global membrane stiffness matrix

$$\mathbf{C}_{\mathrm{g}} = \begin{bmatrix} \mathbf{C}_{11} & & \mathbf{0} \\ & \ddots & \\ \mathbf{0} & & \mathbf{C}_{N_{\mathrm{C}x}N_{\mathrm{C}y}} \end{bmatrix}, \tag{2.96}$$

the global radiation impedance matrix

$$\boldsymbol{\Xi}_{\mathrm{g}} = \boldsymbol{\Xi}_{\mathrm{g}}^{\mathrm{T}} = \begin{bmatrix} \boldsymbol{\Xi}_{1111} & \cdots & \boldsymbol{\Xi}_{11N_{\mathrm{C}x}N_{\mathrm{C}y}} \\ \vdots & \ddots & \vdots \\ \boldsymbol{\Xi}_{11N_{\mathrm{C}x}N_{\mathrm{C}y}}^{\mathrm{T}} & \cdots & \boldsymbol{\Xi}_{N_{\mathrm{C}x}N_{\mathrm{C}y}N_{\mathrm{C}x}N_{\mathrm{C}y}} \end{bmatrix}, \tag{2.97}$$

as well as

$$\mathbf{L}_{\mathrm{g}} = \begin{bmatrix} \mathbf{L}_{11} & & \mathbf{0} \\ & \ddots & \\ \mathbf{0} & & \mathbf{L}_{N_{\mathrm{C}x}N_{\mathrm{C}y}} \end{bmatrix} \text{ and } \mathbf{Q}_{\mathrm{g}} = \begin{bmatrix} \mathbf{Q}_{11} & & \mathbf{0} \\ & \ddots & \\ \mathbf{0} & & \mathbf{Q}_{N_{\mathrm{C}x}N_{\mathrm{C}y}} \end{bmatrix}. \tag{2.98}$$

The column vectors $\mathbf{c}_{\mathrm{g}}$, $\mathbf{u}_{\mathrm{M,g}}$, $\boldsymbol{\gamma}_{\mathrm{g}}$, and $\mathbf{b}_{\mathrm{g}}$ are assembled from the vectors $\mathbf{c}_{pq}$, $\mathbf{u}_{\mathrm{M},pq}$, $\boldsymbol{\gamma}_{pq}$, and $\varepsilon_{pq}\mathbf{b}$ for each individual MAM unit cell. Using the eigenpairs of each cell, Eq. (2.95) can be transformed into the following reduced order modal form

$$\left(\hat{\boldsymbol{\Lambda}}_{\mathrm{g}} + \mathrm{i}\Omega\hat{\boldsymbol{\Xi}}_{\mathrm{g}} - \Omega^2\mathbf{I}\right)\hat{\mathbf{c}}_{\mathrm{g}} = 2\beta_{\mathrm{i}0}\hat{\mathbf{b}}_{\mathrm{g}}. \tag{2.99}$$

The global matrices in the system of equations Eq. (2.95) (or in the reduced form in Eq. (2.99)) have some important properties which are relevant for the physical interpretation and the computational treatment of these equations: All global system matrices are block diagonal matrices, except for the global radiation impedance matrix $\boldsymbol{\Xi}_{\mathrm{g}}$, which is symmetric (due to the acoustic reciprocity principle, as discussed above) and fully populated. This means physically that the in vacuo

response of the MAM array (i.e. $\boldsymbol{\Xi}_\mathrm{g} = \mathbf{0}$) consists of the independent in vacuo responses of every single MAM unit cell. In the most general case, where each unit cell is assumed to have different properties, this corresponds computationally to the solution of N_C independent systems of equations with each $N_{pq} + 3 + I_{pq}$ unknowns. The acoustic coupling of the MAM cells via the reradiated pressure field is established by the radiation impedance matrix $\boldsymbol{\Xi}_\mathrm{g}$. The diagonal blocks of $\boldsymbol{\Xi}_\mathrm{g}$ correspond to the self-radiation impedance, i.e. the vibro-acoustic influence of the response of a cell on its own vibration. The off-diagonal blocks represent the mutual radiation impedance, which characterizes the vibro-acoustic influence of the response of one cell on the vibration of a different MAM cell.

The nondimensional radiated power $\mathit{\Pi}_\mathrm{t}$ of the array is obtained by performing the integration in Eq. (2.64) over the whole array surface. The nondimensional incident power $\mathit{\Pi}_\mathrm{i}$ is calculated by summing up Eq. (2.60) N_C times. Thus, the transmission coefficient τ_{θ_i} of the MAM array is finally given by

$$\tau_{\theta_\mathrm{i}} = \frac{\mathit{\Pi}_\mathrm{t}}{\mathit{\Pi}_\mathrm{i}} = \frac{2\Omega^2 \mathcal{Z}_0}{N_\mathrm{C} \cos\theta_\mathrm{i}} \widetilde{\mathbf{c}}_\mathrm{g}^\mathrm{H} \mathrm{Re}\left\{\boldsymbol{\Xi}_\mathrm{g}\right\} \widetilde{\mathbf{c}}_\mathrm{g}, \tag{2.100}$$

with $\widetilde{\mathbf{c}}_\mathrm{g} = \mathbf{c}_\mathrm{g}/(2\beta_{\mathrm{i}0})$, or, in terms of the modal form in Eq. (2.99), by

$$\tau_{\theta_\mathrm{i}} = \frac{2\Omega^2 \mathcal{Z}_0}{N_\mathrm{C} \cos\theta_\mathrm{i}} \widetilde{\hat{\mathbf{c}}}_\mathrm{g}^\mathrm{H} \mathrm{Re}\left\{\hat{\boldsymbol{\Xi}}_\mathrm{g}\right\} \widetilde{\hat{\mathbf{c}}}_\mathrm{g}, \tag{2.101}$$

with $\widetilde{\hat{\mathbf{c}}}_\mathrm{g} = \hat{\mathbf{c}}_\mathrm{g}/(2\beta_{\mathrm{i}0})$.

2.2.3. Low-frequency approximation

The computational effort for assembling and solving the global system of equations (2.95) is rather high, even when some beneficial properties of the involved matrices are exploited. In Section 2.1.4 it has been

shown that the sound transmission through a MAM unit cell can be simplified in the low-frequency range with $\kappa_0 \ll 1$ by computing the nondimensional effective surface mass density μ''_{eff} of the MAM and using the mass-law relationship in Eq. (2.70) to obtain the sound transmission factor $\tilde{t}_{\theta_\mathrm{i}}$. Therefore, it seems reasonable to apply a similar simplification to the multi-celled array using the effective surface mass densities of each cell $\mu''_{\mathrm{eff},pq}$.

In the proposed simplified MAM array model, each MAM unit cell shown in Fig. 2.6 is replaced by a rectangular rigid plate with the same length L_x and width L_y as the unit cell, but with a frequency-dependent effective surface mass density $\mu''_{\mathrm{eff},pq}$ obtained from the relationship in Eq. (2.71). The unit plates are assumed to act as elementary radiators with a piston displacement amplitude of $\bar{u}_{pq}$ resulting from the surface averaged pressure difference $\Delta\bar{\beta}_{pq}$ on the MAM cell [16]. Thus, the equation of motion of each elementary radiator is given by

$$-\Omega^2\mu''_{\mathrm{eff},pq}\bar{u}_{pq} = \Delta\bar{\beta}_{pq}. \tag{2.102}$$

Following the decomposition of the pressure difference into a blocked and reradiated pressure part (see Eq. (2.80)), this can be rewritten as

$$-\Omega^2\mu''_{\mathrm{eff},pq}\bar{u}_{pq} = 2\beta_{\mathrm{i}0}\varepsilon_{pq}\bar{b} - 2\bar{\beta}_{\mathrm{rr},pq}, \tag{2.103}$$

where $\bar{b} = -(\mathrm{e}^{-\mathrm{i}\kappa_\xi}-1)(\mathrm{e}^{-\mathrm{i}\kappa_\eta}-1)/(\kappa_\xi\kappa_\eta)$ after carrying out the surface averaging of the blocked pressure field. The averaged reradiated pressure $\bar{\beta}_{\mathrm{rr},pq}$ acting on the unit cell (p,q) is a superposition of the reradiated pressure fields of all surrounding elementary radiators. These reradiated pressure components can be obtained from the elementary radiation impedance $\bar{\Xi}_{pqp'q'} = 2\bar{\beta}_{\mathrm{rr},pq}/(\mathrm{i}\Omega\bar{u}_{p'q'})$, defined here as the ratio of twice the averaged reradiated pressure field on cell (p,q) to the piston velocity of the elementary radiator (p',q'). Thus, Eq. (2.103) can

be written as

$$-\Omega^2\mu''_{\mathrm{eff},pq}\bar{u}_{pq}+\mathrm{i}\Omega\sum_{p'q'}\bar{\Xi}_{pqp'q'}\bar{u}_{p'q'}=2\beta_{\mathrm{i}0}\varepsilon_{pq}\bar{b}. \tag{2.104}$$

By setting up Eq. (2.104) for every unit cell, the resulting system of equations, written in matrix form, becomes

$$\left(\mathrm{i}\Omega\bar{\boldsymbol{\Xi}}-\Omega^2\bar{\mathbf{M}}\right)\bar{\mathbf{u}}=2\beta_{\mathrm{i}0}\bar{b}\boldsymbol{\varepsilon}, \tag{2.105}$$

where $\bar{\boldsymbol{\Xi}}=\bar{\boldsymbol{\Xi}}^{\mathrm{T}}=(\bar{\Xi}_{pqp'q'})\in\mathbb{C}^{N_{\mathrm{C}}\times N_{\mathrm{C}}}$ is the elementary radiation impedance matrix, $\bar{\mathbf{M}}=\mathrm{diag}(\mu''_{\mathrm{eff},11},\ldots,\mu''_{\mathrm{eff},N_{\mathrm{C}x}N_{\mathrm{C}y}})\in\mathbb{C}^{N_{\mathrm{C}}\times N_{\mathrm{C}}}$ contains the frequency-dependent nondimensional effective surface mass densities of the MAM cells, $\bar{\mathbf{u}}=(\bar{u}_{11},\ldots,\bar{u}_{N_{\mathrm{C}x}N_{\mathrm{C}y}})^{\mathrm{T}}$ is the vector of unit cell piston displacements, and $\boldsymbol{\varepsilon}=(\varepsilon_{11},\ldots,\varepsilon_{N_{\mathrm{C}x}N_{\mathrm{C}y}})^{\mathrm{T}}$. The calculation of the elementary radiation impedance matrix $\bar{\boldsymbol{\Xi}}$ can be performed rather efficiently using analytical equations available in the literature. As proposed by Bai and Tsao [4], the elements of the radiation impedance matrix can be obtained with

$$\bar{\Xi}_{pqp'q'}=\bar{\Xi}_{p'q'pq}=\mathrm{i}\frac{\mathcal{Z}_0\kappa_0}{\pi\Lambda}\begin{cases}\frac{16}{3}\sqrt{\Lambda/\pi}-\mathrm{i}\kappa_0 & \text{for } p=p'\wedge q=q'\\ \Gamma(\bar{\Delta}_{pqp'q'}) & \text{else,}\end{cases} \tag{2.106}$$

where $\bar{\Delta}_{pqp'q'}=\sqrt{(p'-p)^2+(q'-q)^2/\Lambda^2}$ is the nondimensional distance between the unit cell centroids.

The system of equations (2.105) can be solved for the vector $\bar{\mathbf{u}}$ to obtain the displacement amplitudes of the elementary radiators. Similar to Eq. (2.100), the transmission coefficient $\tau_{\theta_{\mathrm{i}}}$ of the MAM array is then given by

$$\tau_{\theta_{\mathrm{i}}}=\frac{2\Omega^2\mathcal{Z}_0}{N_{\mathrm{C}}\cos\theta_{\mathrm{i}}}\widetilde{\bar{\mathbf{u}}}^{\mathrm{H}}\mathrm{Re}\left\{\bar{\boldsymbol{\Xi}}\right\}\widetilde{\bar{\mathbf{u}}}, \tag{2.107}$$

with $\widetilde{\bar{\mathbf{u}}}=\bar{\mathbf{u}}/(2\beta_{\mathrm{i}0})$.

2.3. Numerical verification

In order to verify the correct derivation of the analytical models for MAMs in Sections 2.1 and 2.2, numerical simulations using the finite element method (FEM) have been performed on selected configurations of MAM unit cells and MAM arrays. Section 2.3.1 discusses the results for the MAM unit cell model. The verification of the MAM array model is presented in Section 2.3.2.

2.3.1. Verification of the unit cell model

The numerical model for the verification of the analytical MAM unit cell model, as illustrated in Fig. 2.7, was created to closely match the setup shown in Fig. 2.5. It consists of a rectangular MAM unit cell with edge lengths L_x and L_y. The membrane part of the MAM is discretized using second order shell elements with the outer edges simply supported. The added mass is modeled with three dimensional second order solid elements that are coupled to the membrane displacement at coincident nodes. The prismatic fluid domains on both sides of the MAM are also discretized using second order solid elements. In order

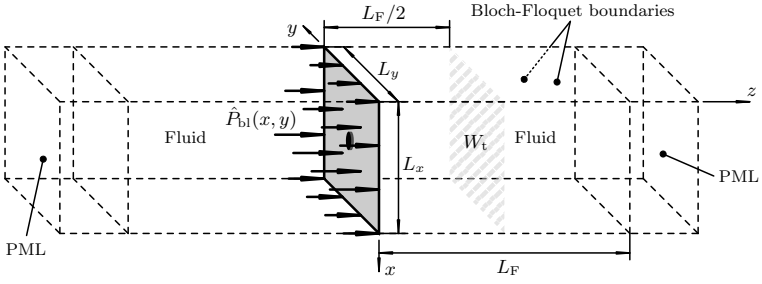

Figure 2.7: Basic setup of the numerical model used for the validation of the analytical MAM unit cell model (not to scale).

to resolve the vibrational field of the MAM and the acoustic pressure fields, the maximum element size is given by $d_{\mathrm{el}} = \min(\lambda_{\min}, L_x, L_y)/6$, where $\lambda_{\min} = c_0/f_{\max}$ is the smallest acoustic wavelength within the simulated range of frequencies. Thus, at least six elements per wavelength and MAM edge length are present in the discretized model. The side surfaces of the fluid domains are defined as Bloch-Floquet periodic boundaries with the Bloch wave vector $\mathbf{k}_{\mathrm{B}}$ equal to the wave vector of the incident plane wave $\mathbf{k}_{\mathrm{i}}$. The fluid domains are truncated in z-direction after a distance of $L_{\mathrm{F}} = L_x$ from the membrane plane. Therefore, perfectly matched layers (PML) discretized with six elements in z-direction are attached to the free end surfaces of the domains in order to reduce reflections of the scattered sound waves even at large angles of incidence θ_{i}. At the common surfaces between the MAM and the fluid domains, full fluid-structure coupling is achieved at coincident nodes. For this purpose, the MAM vibrational velocity is coupled to the particle velocity of the fluid and, in the other direction, the sound pressure is coupled to the force per unit area acting on the MAM surface.

The acoustic excitation of the MAM is provided by the blocked pressure amplitude field $\hat{P}_{\mathrm{bl}}$ of the incident plane acoustic wave given by

$$\hat{P}_{\mathrm{bl}}(x, y) = 2\hat{P}_{\mathrm{i0}} \mathrm{e}^{-\mathrm{i}\left(k_{\mathrm{i}x}x + k_{\mathrm{i}y}y\right)}. \tag{2.108}$$

The discretization of the governing equations for the acoustic and structural domains as well as the excitation and boundary conditions yields a coupled linear system of equations that is solved in the frequency domain using a direct solver. From the computed results, the transmitted sound power W_{t} is obtained by integrating the z-component of the acoustic intensity vector across a surface parallel to the membrane and $L_{\mathrm{F}}/2$ away from the membrane (see Fig. 2.7). The determination of the sound power passing through the lateral boundaries of the enveloping surface is not necessary due to the periodic boundary conditions im-

posed on the sides of the fluid domains. With the incident sound power W_i given by Eq. (2.59), the transmission coefficient τ_{θ_i} of the MAM follows from its definition in Eq. (1.1).

The basic nondimensional parameters of the MAM unit cell configuration VV1, which is considered in the verification simulations, are provided in Table 2.1. A single cylindrical mass is added to the membrane with a nondimensional mass diameter given by $\delta_\mathrm{M} = D_\mathrm{M}/L_x$, where D_M is the true diameter of the mass, and $\vartheta_{\xi'} = \vartheta_{\eta'} = \vartheta = (D_\mathrm{M}^2/16 + h_\mathrm{M}^2/12)/L_x^2$, where h_M is the mass thickness. The position of the mass center of gravity, denoted by the coordinates ξ^* and η^*, is chosen off-centered in order to verify the analytical model in case of an asymmetric setup.

For the given configuration, $N_x = N_y = 160$ membrane modes and $N_x^{(\varphi)} = N_y^{(\varphi)} = 5$ higher order fluid modes were found to yield sufficiently accurate results in the calculation of the MAM unit cell transmission loss using the analytical models given in Section 2.1. The coupling between the membrane and the mass is established using $I = 88$ matching points distributed evenly across the common surface between the membrane and the mass.

In Fig. 2.8, the analytical and numerical results are shown for two different values of the nondimensional speed of sound ς_0 at normal inci-

Table 2.1: Nondimensional parameters of the investigated basic MAM unit cell configurations with a single cylindrical added mass.

	Membrane			Cylindrical mass					Fluid	
Conf.	Λ	Ξ	η_m	δ_M	μ	ϑ	ξ^*	η^*	$\mathcal{Z}_0$	ς_0
VV1	1.5	10^{-5}	10^{-2}	0.1	1.0	10^{-3}	0.6	0.7	4	10
VV2	1.0	1.3×10^{-5}	10^{-3}	0.13	2.26	1.2×10^{-3}	0.5	0.5	4.3	7.4
VV3	1.0	1.3×10^{-5}	10^{-3}	0.30	2.31	5.8×10^{-3}	0.5	0.5	4.3	7.4
PAR1	1.0	0	0	0.1	1.0	10^{-3}	0.5	0.5	4	10

dence ($\theta_\mathrm{i} = 0°$) while keeping all other parameters constant according to Table 2.1. The motivation for using two different values of ς_0 is that the low-frequency approximation described in Section 2.1.4 was derived under the assumption that $\kappa_0 = \Omega/\varsigma_0 \ll 1$. Therefore, the accuracy of the proposed low-frequency approximation should be evaluated for different values of the non-dimensional wave number κ_0. In order to keep the non-dimensional frequencies Ω as well es the characteristic (anti-)resonances the same in both cases for better comparison, ς_0 is varied to achieve different values of κ_0 in Figs. 2.8(a) and 2.8(b). Fig. 2.8(a) represents the long wavelength case with $\varsigma_0 = 10$ and the nondimensional wave number $\kappa_0 \leq 1$ within the calculated nondimensional frequency range $\Omega = 1$ to 10. In Fig. 2.8(b), however, $\varsigma_0 = 1$ and, consequently, $\kappa_0 = 1$ to 10 so that the acoustic wavelength is comparable to the MAM edge length L_x. Arrows on the frequency axis indicate the cut-on frequencies of the higher-order fluid modes where the modal wave numbers κ_{rs} become real, i.e. the radicand in Eq. (2.44)

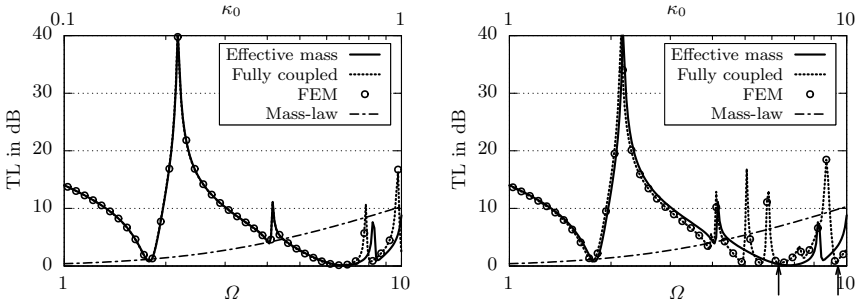

(a) $\varsigma_0 = 10$. **(b)** $\varsigma_0 = 1$.

Figure 2.8: Normal incidence sound transmission loss of the MAM unit cell configuration VV1 given in Table 2.1 as obtained from the analytical model and the FEM simulations. Cut-on frequencies of higher-order fluid modes are indicated with arrows on the frequency axis.

is zero. In both plots, the solid lines represent the results from the effective mass approximation using Eqs. (2.71) and (2.70), while the dotted lines have been obtained from the fully coupled MAM unit cell model in Section 2.1.3. The circles correspond to the results from the FEM simulations. For comparison, the equivalent mass-law transmission loss of the MAM unit cell is included in Fig. 2.8, as obtained from Eq. (2.70) with the effective nondimensional surface mass density of the MAM replaced by the static value $\mu''_{\mathrm{st}} = 1 + \Lambda\mu$.

Qualitatively, the transmission loss spectrum in Fig. 2.8(a) exhibits the typical characteristics for a MAM with an eccentrically placed mass: At $\Omega = 1.8$, the first MAM resonance appears as a local minimum with TL ≈ 0. This mode is characterized by a predominant translational motion of the added mass. The first TL peak occurs at $\Omega = 2.2$, where the surface averaged displacement amplitude of the MAM approaches zero. The maximum transmission loss at this peak is approximately 40 dB, which is substantially higher than the corresponding mass-law value at this frequency (≈ 1.7 dB). At higher frequencies, a second peak with TL ≈ 10 dB appears at $\Omega = 4.1$, which is associated to the rotational motion of the eccentrically placed mass [10]. Finally, at $\Omega = 6.7$, another resonance can be observed with a strongly reduced TL over a relatively broad frequency band. This resonance corresponds to the first annular-type resonance of the MAM, where the mass is mostly at rest (see point B in Fig. 1.4(a)). At the end of the frequency spectrum, additional peaks and resonances appear, which can be attributed to the vibrational characteristics of the annular membrane. However, as indicated by the dash-dotted curve, the mass-law typically is quite effective at these frequencies and therefore these higher-order peaks usually are of no practical relevance.

An excellent agreement between both analytical models and the simulations can be observed for the most part of the investigated frequency range in Fig. 2.8(a). Only for $\Omega > 7$ (corresponding to $\kappa_0 > 0.7$), the

effective mass approximation diverges from the other results. The fully coupled model, however, is in close agreement with the simulations over the whole frequency range, which indicates that the influence of higher-order fluid modes is significant for $\kappa_0 > 0.7$. A closer inspection of the results in Fig. 2.8(a) at higher frequencies reveals that the higher-order TL maxima and minima in the fully coupled model and numerical simulations are shifted to lower frequencies, compared to the prediction by the effective mass approximation. This can be explained by the added fluid mass of the evanescent fluid modes coupled to the MAM. Since evanescent waves are purely reactive, they induce an additional inertia to the MAM structure, which leads to a reduction of the MAM eigenfrequencies compared to the in vacuo values [22]. The effective surface mass density of the MAM, however, is obtained from the in vacuo response (see Eq. (2.71)) so that this approximation does not account for the fluid loading effects of the higher-order modes. The imaginary part of the radiation impedance matrix $\boldsymbol{\Xi}$, also called the radiation reactance, is associated with the inertial fluid loading effects. In Eq. (C.8) it can be seen that the imaginary part of $\boldsymbol{\Xi}$ is proportional to κ_0. Hence, for small nondimensional wave numbers the fluid loading effects are negligible. This explains the excellent agreement between the effective mass approximation and the fully coupled model at lower frequencies in Fig. 2.8(a). For $\kappa_0 \approx 1$ and higher, however, the radiation reactance becomes more important and therefore the approximate results deviate from the fully coupled results in Fig. 2.8(a) at higher frequencies.

For $\varsigma_0 = 10$, no cut-on frequencies are present within the investigated range of frequencies in Fig. 2.8(a). Therefore, the acoustic far field radiated by the MAM is governed only by a plane acoustic wave. In Fig. 2.8(b), the nondimensional speed of sound is decreased to $\varsigma_0 = 1$ and the first cut-on frequency consequently occurs at $\Omega = 2\pi$ for normal incidence, as indicated by the arrows in Fig. 2.8(b). The transmis-

sion loss obtained using the effective surface mass density approximation is independent of ς_0. Thus, the solid curve in Fig. 2.8(b) is identical to that in Fig. 2.8(a). However, since in this case κ_0 lies between 1 and 10, the fluid loading effects are much more important. This is indicated by the results from the fully coupled analytical model and the numerical simulation both being shifted to lower frequencies compared to the effective mass model, even around the first transmission loss peak. Nevertheless, the qualitative agreement between the effective mass approximation and the fully coupled calculations is still rather good, as long as frequencies much lower than the first cut-on frequency are concerned.

Above the first cut-on frequency, the differences between the fully coupled models and the approximate solution become much more evident. Thus, when non-plane waves are contributing to the far field acoustic radiation of the MAM, the simplified model in Eq. (2.70) using the effective surface mass density of the MAM provides inaccurate results and the fully coupled model from Section 2.1.3 should be used instead. This advanced analytical model exhibits an excellent agreement with the numerical data in Fig. 2.8(b), even at high frequencies where multiple higher-order fluid modes occur. Therefore, this model can be used to accurately predict the sound transmission loss of a MAM unit cell when fluid loading effects and the radiation of non-plane acoustic waves become significant.

The influence of the incidence angle θ_i is illustrated in Fig. 2.9, where the same results as in Fig. 2.8 are shown for an obliquely incident plane wave with an incidence angle of $\theta_\mathrm{i} = 60°$ and an azimuth angle of $\phi_\mathrm{i} = 30°$. In the long wavelength case shown in Fig. 2.9(a), the effect of the incidence angle is as expected from the approximate relationship in Eq. (2.70): The qualitative shape of the TL curve remains unchanged and only the TL magnitude is reduced by $10\,\mathrm{lg}(\cos^2 60°) \approx -6$ dB (except for small values of TL, where this effect is diminished due to

the damping effect of the fluid). Therefore, the performance of sub-wavelength sized MAMs is not impaired by obliquely incident plane acoustic waves, except for the typical $\cos\theta_\mathrm{i}$ influence. In the case of smaller wavelengths, as shown in Fig. 2.9(b), the influence of the oblique incidence is similar. However, since in this case the first cut-on frequency occurs already at $\Omega \approx 4.16$, the deviation between the effective mass approximation and the fully coupled models is much more significant over the whole frequency range as in Fig. 2.9(a).

Still, the agreement between the FEM simulations and the fully coupled analytical model is very good in Fig. 2.9. Thus, this model can be regarded as verified by the numerical simulations. The approximate model using the effective surface mass density is accurate only in the long wavelength limit with $\kappa_0 \ll 1$ (as discussed above). Nevertheless, it also delivers good estimates below the first cut-on frequency with a slight overprediction of the resonance and peak frequencies due to the neglected fluid loading effect of higher-order modes.

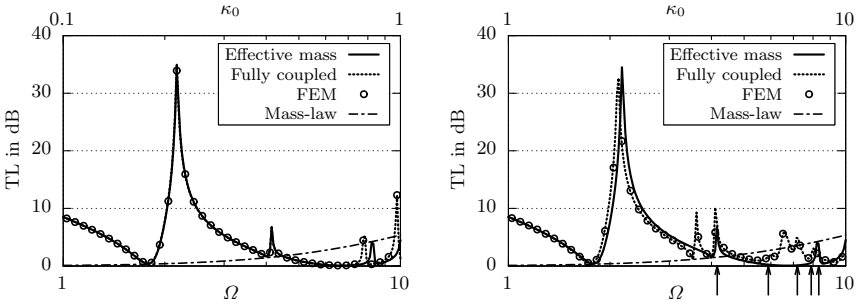

(a) $\varsigma_0 = 10$. **(b)** $\varsigma_0 = 1$.

Figure 2.9: Oblique incidence ($\theta_\mathrm{i} = 60°$, $\phi_\mathrm{i} = 30°$) sound transmission loss of the MAM unit cell configuration VV1 given in Table 2.1 as obtained from the analytical model and the FEM simulations. Cut-on frequencies of higher-order fluid modes are indicated with arrows on the frequency axis.

2.3.2. Verification of the MAM array model

Fig. 2.10 illustrates the setup for the numerical simulation of a planar MAM array using the finite element method. The simulation model consists of N_C MAM unit cells located in the xy-plane, which are modeled with the same element types and boundary conditions as in the unit cell simulations in Section 2.3.1. The MAM array is surrounded by a rigid baffle, where the z-component of the particle velocity is set to zero. On both sides of the baffle, a box-shaped fluid domain is coupled to the MAM array. The fluid domains are L_F high and extend to the sides of the MAM array by L_F. In order to reduce the element count, the discretization and geometry are automatically updated for each evaluated frequency f: The maximum element size of

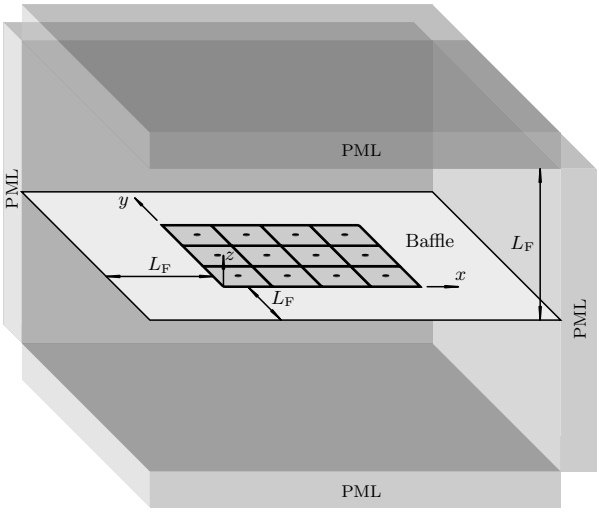

Figure 2.10: Basic setup of the numerical model used for the verification of the analytical MAM array model (not to scale).

the tetrahedral second order fluid elements is adjusted to correspond to $d_{\mathrm{el,F}} = \lambda_0/6$ and the MAMs are discretized with a maximum element size of $d_{\mathrm{el,m}} = \min(\lambda_0, L_x, L_y)/6$. The length L_{F} is set to be equal to four fluid element edge lengths, i.e. $L_{\mathrm{F}} = 4d_{\mathrm{el,F}}$. For the minimization of reflections at the fluid boundaries, six PML elements are added to the free boundaries of the fluid domains.

As in the unit cell FEM model, full fluid-structure coupling is established between the MAMs and the surrounding fluid domains. The blocked pressure amplitude field in Eq. (2.108) is used for the excitation of the MAMs. The transmitted sound power W_{t} is evaluated by integrating the surface normal component of the sound intensity across the boundaries of the upper fluid domain spanning the MAM array. The incident sound power, on the other hand, is given by the excitation pressure amplitude $\hat{P}_{\mathrm{i}0}$ using Eq. (2.59), with the MAM unit cell surface L_xL_y replaced by the total surface of the MAM array $N_{\mathrm{C}}L_xL_y$.

The properties of the investigated MAM array are given in Table 2.2, denoted by configuration A-VV1. The MAM unit cells all have the same properties corresponding to the configuration VV1 in Table 2.1. The array is composed of $N_{\mathrm{C}x} = 4$ unit cells in x-direction and $N_{\mathrm{C}y} = 3$ unit cells in y-direction, resulting in an overall number of unit cells of $N_{\mathrm{C}} = 12$, with a uniform prestress distribution. For the analytical models, the same setup as in Section 2.3.1 is used. In order to reduce the

Table 2.2: Nondimensional parameters of the investigated basic MAM array configurations.

Conf.	Unit cell conf. (see Table 2.1)	Number of cells $N_{\mathrm{C}x}$	$N_{\mathrm{C}y}$	Prestress τ_{pq}
A-VV1	VV1	4	3	1
A-PAR1	PAR1	4	4	1

computational effort for solving the coupled global system of equations (2.95), the modal formulation in Eq. (2.99) is used with the first $\hat{N} = 12$ unit cell eigenpairs. The effective surface mass densities of the MAM unit cells for the simplified MAM array model from Section 2.2.3 are obtained by a direct solution algorithm.

The normal incidence sound transmission loss results of the 4×3 MAM array obtained using the analytical and numerical models are shown in Fig. 2.11. As in Fig. 2.8, two different nondimensional speed of sounds have been considered: Fig. 2.11(a) represents the long wavelength limit with $\varsigma_0 = 10$, while in Fig. 2.11(b) $\varsigma_0 = 1$ and the wavelength becomes comparable to the MAM unit cell edge lengths. In both figures, solid lines represent the results from the elementary radiator model with the effective surface mass densities of the MAM unit cells (see Section 2.2.3). The dotted lines have been obtained from the fully coupled model in Section 2.2.2. The FEM results are denoted by circles in Fig. 2.11.

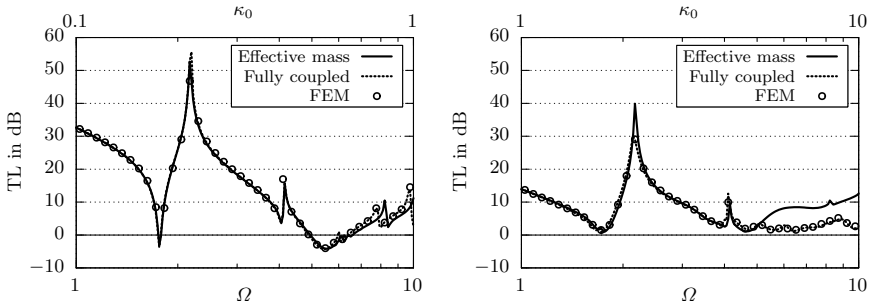

(a) $\varsigma_0 = 10$. **(b)** $\varsigma_0 = 1$.

Figure 2.11: Normal incidence sound transmission loss of the baffled 4×3 multi-celled MAM panel as obtained from the analytical model and the FEM simulations.

Qualitatively, the sound transmission loss of the MAM array shown in Fig. 2.11(a) is very similar to the MAM unit cell TL in Fig. 2.8(a). In fact, the first resonance minimum as well as the first two transmission loss peaks occur at the same frequencies as in the unit cell model. Quantitatively, however, the transmission loss of the array is augmented considerably compared to the infinite array investigated in the previous section. This is a consequence of the "windowing" effect by the aperture of the baffle. As explained by Fahy and Gardonio [22, pp. 296–299], this effect limits the number of forced wavelengths from the incident sound field that fit between the edges of the panel. This leads to a reduction of the forced-wave sound transmission and an improved low-frequency sound transmission loss of small sized panels. Also, negative TL values can be observed at the resonances of the MAM array. These are caused by the definition of the sound power transmission coefficient τ in Eq. (1.1), which does not account for the scattering effects that occur in the vicinity of finite panels at the resonance frequencies when normalizing the transmitted sound power with the incident sound power [88].

The comparison of both analytical models and the FEM results in Fig. 2.11(a) shows that in the long wavelength case all three models are in excellent agreement with each other, except for frequencies $\Omega > 7$, where the elementary radiator model deviates from the other two results. This has already been observed in Fig. 2.8(a) for the unit cell model, where the higher-order fluid mode loading on the MAMs becomes significant, which is not taken into account in the effective surface mass density models.

In Fig. 2.8(b), the acoustic wavelength is comparable to the MAM array dimensions for most of the investigated frequency range. Therefore, the TL curve much more resembles the infinite unit cell array results in Fig. 2.8(b), except for the higher order peaks, which do not appear in Fig. 2.11(b) above $\Omega = 5$. More importantly, it can be seen

in this diagram that the first resonance and first peak of the MAM array occur at the same frequencies as calculated with the unit cell model in Fig. 2.8(b). Thus, the unit cell model delivers a good estimate of the sound transmission loss characteristics of a MAM array, when the acoustic wavelength is in the order of the total dimensions of the array. The TL-spectrum predicted by the elementary radiator model is in good agreement with the other results up to $\Omega = 5$. Above this frequency, the acoustic wavelength is comparable to the unit cell dimensions and the elementary radiator assumption breaks down, similar to what has been observed for the unit cell model in Fig. 2.8(b). Also, it can be seen that the effective mass model overpredicts the first TL maximum by 10 dB. A possible explanation for this is that at shorter wavelengths the sound radiation by the MAM displacement near the outer edges of the array becomes more significant [22]. Since the elementary radiator model only takes into account the spatially averaged displacement amplitude and the effective surface mass density of the MAMs is very large at anti-resonance, the MAM displacement at the edges of the array is near-zero in case of the simplified model. For the fully coupled model, however, the deviatoric part of the MAM vibration amplitude can become quite large (even when the surface averaged value is near-zero), so that sound can be radiated at the edges of the array. This is indicated by the reduced TL maximum as compared to the effective mass model. Overall, it can be seen in Fig. 2.8(b) that the fully coupled model yields a very good reproduction of the simulated results over the whole investigated frequency range.

Fig. 2.12 shows the transmission loss of the baffled 4×3-array under oblique incidence with $\theta_\mathrm{i} = 60°$ and $\phi_\mathrm{i} = 30°$. In Fig. 2.12(a) it can be seen that in the long wavelength case with $\varsigma_0 = 10$ there is no significant qualitative difference between the normal incidence TL, as shown in Fig. 2.11(a), and the oblique incidence TL. This is similar to what has been observed in Section 2.3.1 for the MAM unit cell models.

Consequently, the accuracy of the two analytical models exhibits the same characteristics as in the normal incidence case with the effective mass model slightly overpredicting the higher-order resonance and TL-peak frequencies when κ_0 approaches unity. Otherwise, a very good agreement between the analytical models and the FEM simulations can be observed.

For the smaller wavelength case shown in Fig. 2.12(b), the influence of the obliquely incident plane wave is more obvious, especially in case of the elementary radiator model: For $\Omega > 3$, the simplified model diverges from the other results and leads to unrealistically high TL values in the higher frequency range. As already explained for the normal incidence MAM array TL, this is because the elementary radiator assumption is not accurate when the wavelength is comparable to the size of the unit cells. Since the fully coupled analytical model does not rely on such an assumption, the agreement between this model and the FEM results is, again, very good over the whole range of frequencies

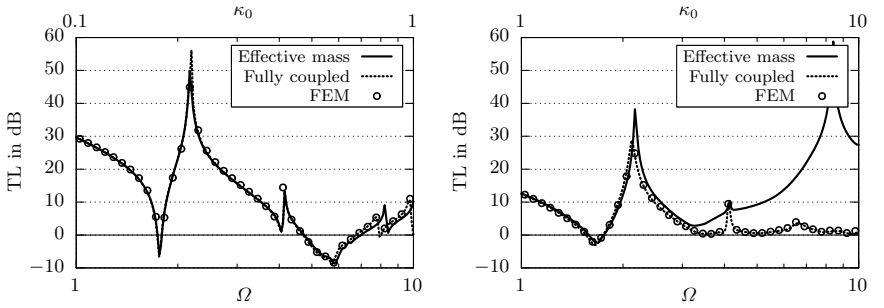

(a) $\varsigma_0 = 10$. **(b)** $\varsigma_0 = 1$.

Figure 2.12: Oblique incidence ($\theta_\mathrm{i} = 60°$, $\phi_\mathrm{i} = 30°$) sound transmission loss of the baffled 4×3 multi-celled MAM panel as obtained from the analytical model and the FEM simulations.

examined in Fig. 2.12(b).

Based upon the results presented in this subsection, the MAM array model from Section 2.2.2 is verified using the numerical simulations, even for large values of κ_0. The simplified elementary radiator model using the effective surface mass density of the MAM unit cells, on the other hand, has been shown to be valid only for $\kappa_0 \ll 1$ due to the required long wavelength limit. However, similar to the unit cell model, the effective mass model yields reasonable estimates for the transmission loss of the MAM array even when $\kappa_0 \approx 1$. For $\kappa_0 > 3$, this model becomes very inaccurate (especially when oblique incidence is considered) and the fully coupled model should be used instead.

In terms of computational efficiency, both MAM array models offer improved calculation times over the FEM simulations: On average, the finite element model required 59 s of CPU time per frequency step in the long wavelength case (not even including the considerable amount of time spent for pre- and post-processing of the model). The fully coupled model, on the other hand, required 38 s per frequency, which corresponds to a reduction of computation times by 36 %. The effective mass model is even more efficient with only 0.06 s of CPU time per frequency, which is a reduction of computation time by nearly a factor of 1000 compared to the FEM simulation. This shows that the proposed analytical models offer an advantage over conventional FEM simulations of baffled MAM arrays. In particular, the high computational efficiency of the effective surface mass density model enables the rapid evaluation of different MAM array designs, as will be shown in Section 2.5.2.

2.4. Experimental validation of the unit cell model

For the validation of the MAM unit cell model, a square unit cell test sample was built to be experimentally evaluated within an impedance

tube setup according to the test method ASTM E2611-09 [3]. A schematic overview of the test setup is given in Fig. 2.13. This method employs the so-called four-microphone technique, where two microphones on each side of the test sample are used to obtain the amplitudes of the back and forth traveling plane acoustic waves in front of the sample and behind it. These wave amplitudes can then be used to calculate the acoustic transfer matrix $\mathbf{T} \in \mathbb{C}^{2\times 2}$ of the test sample. In general, a transfer matrix $\mathbf{T}$ relates the amplitudes of the acoustic pressure $\hat{P}$ and particle velocity $\hat{v}$ on both sides of a planar acoustic element (denoted as the left side, index "L", and right side, index "R") with thickness d in the following way [2]:

$$\begin{pmatrix} \hat{P}_\mathrm{L} \\ \hat{v}_\mathrm{L} \end{pmatrix} = \underbrace{\begin{bmatrix} T_{11} & T_{12} \\ T_{21} & T_{22} \end{bmatrix}}_{\mathbf{T}} \begin{pmatrix} \hat{P}_\mathrm{R} \\ \hat{v}_\mathrm{R} \end{pmatrix}. \tag{2.109}$$

The elements of $\mathbf{T}$ allow the calculation of several acoustic properties of the sample, such as the normal incidence transmission factor $\tilde{t}$ according to

$$\tilde{t} = \frac{2}{T_{11} + T_{12}/Z_0 + T_{21}Z_0 + T_{22}}. \tag{2.110}$$

In the present experimental setup, a type 4206-T impedance tube from Brüel & Kjær with a diameter of $D_\mathrm{tube} = 100\,\mathrm{mm}$ and four

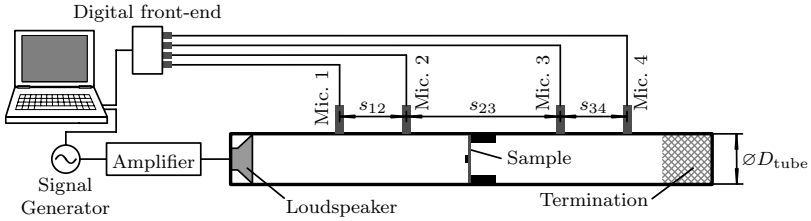

Figure 2.13: Experimental setup for the impedance tube measurements.

type 4187 1/4" pressure microphones are used. The microphone spacings of the impedance tube, as indicated in Fig. 2.13, are given by $s_{12} = s_{34} = 100$ mm and $s_{23} = 350$ mm, so that the measurement frequency range of the impedance tube is $f = 50$ to 1600 Hz [3]. A signal generator is connected via a signal amplifier to the loudspeaker within the tube in order to generate a white noise sound field. The resulting microphone signals are acquired by a digital front-end which routes the measured data to a personal computer for the calculation of the microphone transfer functions using a fast Fourier transform (FFT) algorithm. According to the two-load method described in ASTM E2611-09 [3], for each measured test sample it is necessary to perform the measurement procedure under two different termination conditions of the tube. In the present measurements, these two termination conditions are the closed tube, as shown in Fig. 2.13, and the open tube with the rigid back wall removed.

The investigated MAM unit cell geometry is a square with edge lengths of $L_x = L_y = 46$ mm. The membrane material is a commercially available self-adhesive polyester film labeled *Orastick* which was glued on a fiberboard support frame and prestressed using a hot air blower. The surface mass density and thickness of the film are provided by the manufacturer as $m''_{\mathrm{m}} = 92\,\mathrm{g/m^2}$ and $h_{\mathrm{m}} = 23\,\mu\mathrm{m}$, respectively [40, 41]. The other mechanical properties of the membrane material are estimated based upon typical values for polyester materials, i.e. $E_{\mathrm{m}} = 4700$ MPa, $\nu_{\mathrm{m}} = 0.4$, and $\eta_{\mathrm{m}} = 10^{-3}$ [58]. The prestress resultant of the membrane $T_{\mathrm{m}} = 200\,\mathrm{N/m}$ is obtained by measuring the first resonance frequency of the membrane without attached mass and calculating T_{m} from this result. Two unit cell test samples with different added mass geometries are investigated: In the first sample, a cylindrical steel mass with a diameter of $D_{\mathrm{M}} = 6$ mm and thickness of $h_{\mathrm{M}} = 2$ mm was glued onto the center of the membrane unit cell, which results in an added mass magnitude of $M = 440$ mg. The

second sample employs an aluminum mass with a larger diameter of $D_{\mathrm{M}} = 14$ mm, smaller thickness of $h_{\mathrm{M}} = 1.1$ mm, and a similar resulting added mass of $M = 450$ mg. For the ambient fluid, $\rho_0 = 1.18$ kg/m^3 and $c_0 = 343$ m/s are obtained from the ambient pressure and temperature recorded during the measurements.

The square shaped MAM unit cell test samples are fitted inside the circular tube using a massive steel adapter, which is shown in Fig. 2.14(a). The thickness and mass of the adapter are given by 19 mm and approximately 500 g, respectively. Additionally, the circumference of the adapter is carefully sealed using sealing rings and sealing tape in order to minimize acoustic leakage effects around the adapter. Since the MAM unit cell covers the cross-section of the impedance tube only partially, the measured transfer matrix $\mathbf{T}$ (MAM + adapter) has to be corrected in order to account for the smaller size of the MAM and obtain the actual transfer matrix $\mathbf{T}^{(\mathrm{MAM})}$ of the MAM. This correction is done by assuming the adapter to be rigid and treating the MAM +

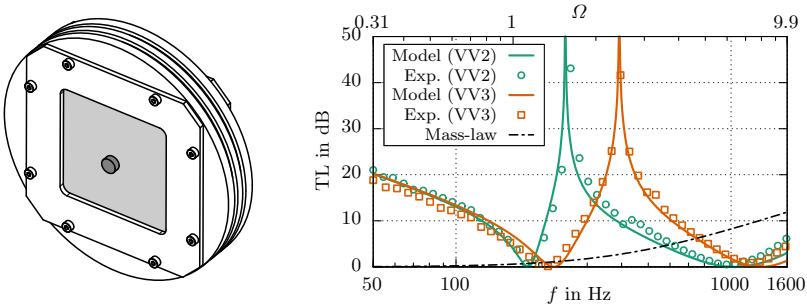

(a) MAM and adapter.

(b) Transmission loss.

Figure 2.14: Normal incidence sound transmission loss of the MAM unit cell configurations VV2 and VV3 given in Table 2.1 as obtained from the analytical model (effective mass) and the impedance tube measurements.

adapter as a parallel assembly. According to the method by Verdière et al. [95], the transfer matrix of the MAM within the adapter is then given by

$$\mathbf{T}^{(\mathrm{MAM})} = \begin{bmatrix} T_{11} & \psi_{\mathrm{MAM}} T_{12} \\ T_{21}/\psi_{\mathrm{MAM}} & T_{22} \end{bmatrix}, \tag{2.111}$$

where T_{11} to T_{22} are the elements of the originally measured transfer matrix $\mathbf{T}$ and $\psi_{\mathrm{MAM}} = L_x L_y/(0.25\pi D_{\mathrm{tube}}^2) \approx 0.27$ is the area fraction of the MAM unit cell within the impedance tube.

For the analytical calculations, the nondimensional parameters of the MAM unit cell configurations can be obtained from the physical parameters given above. The resulting nondimensional values are given in Table 2.1, denoted by configurations VV2 and VV3 for the steel and aluminum mass samples, respectively. The reference frequency ω_{ref} of these MAM unit cell configurations, which relates the angular frequency ω to the nondimensional frequency Ω, is given by $\omega_{\mathrm{ref}} = \sqrt{T_{\mathrm{m}}/m''_{\mathrm{m}}}/L_x \approx 1014$ rad/s. The analytical calculations were performed with the same settings as already described in Section 2.3.1, except that $I = 151$ matching points are used in both cases.

The experimental and analytical results for the normal incidence sound transmission loss are provided in Fig. 2.14(b). Only the analytical results from the effective surface mass density approximation are shown, because the unit cell edge lengths are smaller than the acoustic wavelength over the investigated frequency range. Generally, a very good agreement between the experimental data and the analytical model can be observed for both mass configurations. Around the anti-resonances at 260 Hz (VV2) and 400 Hz (VV3) with peak TL values of over 40 dB, the agreement is particularly good. The anti-resonance frequency of the smaller mass case (VV2) is smaller than that of the larger mass case (VV3), even though the added mass magnitude is nearly the same in both cases. This is caused by the stiffening effect of the larger mass, which will be discussed in the parameter studies in the following

section. The good agreement between theory and experiments for both cases indicates that the simplifications in the analytical model yield a suitable representation of the predominant physical mechanisms within MAM unit cell test samples.

At very high frequencies, it can be seen in Fig. 2.14(b) that the measurements begin to deviate from the analytical predictions. This can be attributed to the fluid loading effect which becomes important at these frequencies. In the stiffness-controlled regime at very low frequencies, some deviations can be observed as well, especially in the test case VV3. It is possible that inaccuracies in the manufacturing process of the test sample or the mounting conditions within the steel adapter led to these differences. Since this frequency range usually is not relevant for practical applications of MAMs [70], these differences can be accepted.

2.5. Parameter studies

In this section, the analytical models are employed to perform parameter studies such that the influence of the nondimensional parameters of the MAM on the sound transmission loss can be systematically investigated. This serves as a basis for the design of the MAM noise shield in Chapter 4. Some parameter studies of MAMs have been performed already by other authors, e.g. considering the added mass magnitude [54, 107], size [54, 66], eccentricity [10, 112], or membrane tension [10, 63]. However, these studies did not involve nondimensional parameters similar to those introduced in the present work, which help to reduce the available parameter space and apply the parameter study results to real designs where certain physical parameters are fixed (e.g. the fluid properties) and others can be freely chosen within certain technical or physical boundaries (e.g. the added mass properties).

In order to provide a systematic overview of the influence of these

nondimensional parameters, this section is divided in two sections: The first subsection provides parameter studies of the nondimensional parameters of a MAM unit cell. In the second subsection, the effects of selected parameters of a MAM array on the transmission loss spectrum are analyzed.

2.5.1. MAM unit cell

The basic properties of the investigated MAM unit cell are given in Table 2.1 as denoted by configuration PAR1. This corresponds to a square shaped unit cell with a single cylindrical mass attached to the MAM center. Thus, the acoustical properties of this unit cell design are fully determined by the ten nondimensional parameters given in Table 2.1. In order to evaluate the prevalent effect of one parameter, each parameter is varied individually while keeping the others constant. The nondimensional frequency Ω is restricted to values so that $\kappa_0 \ll 1$ (i.e. $\Omega \ll \varsigma_0$) and the effective surface mass density approximation can be readily applied. Also, only normal incidence ($\theta_\mathrm{i} = 0°$) is considered, since – as explained in Section 2.3 – the oblique incidence TL can be extrapolated from the normal incidence results in the long wavelength limit.

To provide an overview of the general vibrational characteristics of the MAM, the first four mode shapes of the MAM unit cell are shown in Fig. 2.15. The mode shapes have been generated by computing the eigenvectors according to the method described in Section 2.1.2. The modal displacement fields $u_i(x, y)$ then follow from the expansion in Eq. (2.6) as $u_i(x, y) = \sum_{mn} v_{i,mn} \Phi_{mn}(x, y)$, where $v_{i,mn}$ are the elements of the eigenvector $\mathbf{v}_i$.

It can be seen in Fig. 2.15 that the mode shape of the first eigenfrequency Ω_1 is characterized by a strong translational motion of the central mass, see the discussion in Section 1.2.3. The second and third

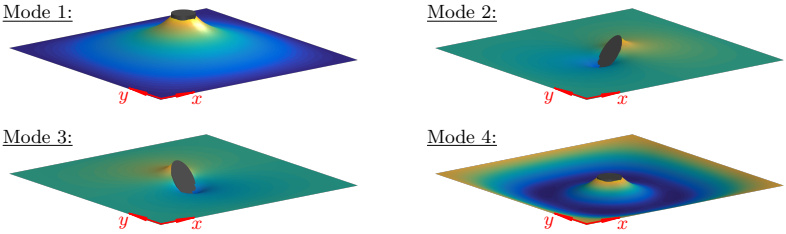

Figure 2.15: First four mode shapes of the MAM unit cell configuration PAR1 given in Table 2.1.

resonances both exhibit a strong rotational motion of the mass, which is governed by the moment of inertia of the mass. Since these two mode shapes are antisymmetric if the mass is placed in the MAM center, these modes do not couple with the surrounding fluid. Hence, it can be expected that Ω_2 and Ω_3 will not be visible in the TL spectra of the MAM as long as a centrally placed mass is considered. Finally, the fourth mode shape associated with Ω_4 is the first annular-type MAM mode, where the added mass is nearly at rest and only the free membrane surface vibrates.

Membrane aspect ratio: The results for the parameter variation of the aspect ratio Λ are shown in Fig. 2.16. The normal incidence TL for three different values of Λ is provided in Fig. 2.16(a). Fig. 2.16(b) shows the variation of the first four MAM resonance frequencies Ω_1 to Ω_4 and the first three anti-resonance frequencies $\Omega_{\mathrm{P}1}$ to $\Omega_{\mathrm{P}3}$ as a function of Λ. The green shaded band in Fig. 2.16(b) represents the bandwidth of the corresponding anti-resonance peak, which is defined here as the frequency range in which the MAM transmission loss exceeds the corresponding mass-law transmission loss by 10 dB.

The second and third resonance and anti-resonance frequencies are

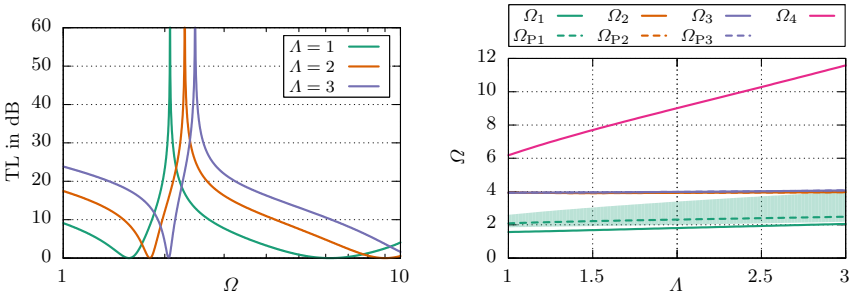

(a) Transmission loss. **(b)** Resonance and peak frequencies.

Figure 2.16: Parameter variation of the membrane aspect ratio Λ.

not visible in the TL spectrum of the MAM. As explained above, this is because the added mass center of gravity is located in the MAM center and the resulting antisymmetric mode shapes do not couple with the surrounding fluid. This is also evident in Fig. 2.16(b), where the curve pairs for Ω_2 and $\Omega_{\mathrm{P}2}$ as well as Ω_3 and $\Omega_{\mathrm{P}3}$ are coincident, i.e. the resonances and anti-resonances annihilate each other. As the aspect ratio of the membrane is increased, the transmission loss spectrum of the MAM shown in Fig. 2.16(a) is shifted to higher frequencies. This is consistent with the resonance frequency variations shown in Fig. 2.16(b), where the MAM resonance frequencies increase as the membrane aspect ratio grows. Ω_1 depends only weakly on Λ, because this mode depends mainly upon the inertia of the added mass. The two rotational modes Ω_2 and Ω_3 are nearly independent of the aspect ratio due to the primary rotational motion of the added mass while most of the membrane is at rest (see Fig. 2.15). A closer inspection of Fig. 2.16(b), however, reveals that for larger aspect ratios the third eigenfrequency begins to increase slightly faster than the second. As the aspect ratio of the MAM becomes larger, the MAM boundaries at $\eta = 0$ and $\eta = 1$ come closer to the

added mass. The nearby boundaries restrain the rotational mass motion about an axis parallel to the ξ-axis of the MAM and consequently Ω_3 is increased. The fourth mode, finally, is strongly increasing with Λ, because this mode is characterized by strong vibrations of the unloaded membrane surfaces. Since a larger aspect ratio effectively reduces the available membrane area, the fourth eigenfrequency is increased similar to the first eigenfrequency of an unloaded rectangular membrane, which is proportional to $\sqrt{1+\Lambda}$. In summary, the primary effect of the nondimensional parameter Λ is a strong shifting of the fourth eigenfrequency of the MAM. The lower eigenfrequencies and anti-resonance frequencies are only slightly affected by Λ.

Apart from the eigenfrequency shifting, increasing the aspect ratio Λ has a positive effect on the bandwidth of the first anti-resonance peak, as indicated in Fig. 2.16(b). However, it should be noted that since the static surface mass density of the MAM is given by $\mu''_{\mathrm{st}} = 1 + \Lambda\mu$, the MAM weight is also increased.

Membrane bending stiffness: In Fig. 2.17, the nondimensional membrane bending stiffness Ξ has been varied between zero (i.e. pure membrane stiffness) and 0.01. In the TL-spectra shown in Fig. 2.17(a) as well as the frequency variation diagram in Fig. 2.17(b) it can be seen that a higher bending stiffness moves all considered resonance and anti-resonance frequencies to higher values and consequently the TL-curve is shifted to the right in Fig. 2.17(a). This is because Ξ only appears in the elements of the membrane stiffness matrix $\mathbf{C}$, as given in Eq. (2.26). Thus, the parameter Ξ effectively increases the stiffness of the membrane and, as a consequence, the MAM resonance frequencies become higher. This added stiffness effect is particularly significant when the curvature of the membrane is high. The mode shapes in Fig. 2.15 indicate that for the second and third mode the curvature of the membrane is relatively high around the mass. This is reflected in Fig. 2.17(b) by

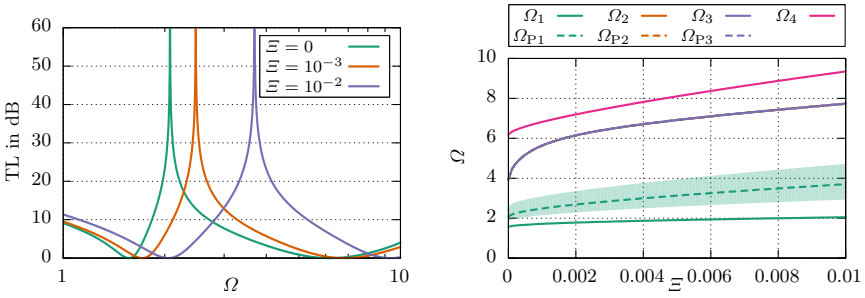

(a) Transmission loss. **(b)** Resonance and peak frequencies.

Figure 2.17: Parameter variation of the nondimensional membrane bending stiffness Ξ.

a strong increase of Ω_2 and Ω_3 as compared to the first eigenmode of the MAM. Ω_4 also increases much faster than Ω_1 due to the higher membrane curvature present in the corresponding mode shape.

The shaded area shows that the nondimensional bending stiffness has a positive effect on the bandwidth of the first anti-resonance peak. This can be explained by the spreading of the MAM resonances as Ξ is increased: The further the resonances are apart within the frequency spectrum, the higher the bandwidth of the anti-resonance between those resonant modes.

Membrane loss factor: As shown in Fig. 2.18, the membrane loss factor η_m does not affect the resonance and anti-resonance frequencies, because loss factors are typically $\eta_\mathrm{m} \ll 1$ and therefore introduce only a small amount of damping into the system. There is, however, a significant influence of the loss factor on the transmission loss of the MAM given in Fig. 2.18(a) for exemplary numerical values of η_m: A higher loss factor tends to smear out the TL minima and maxima at

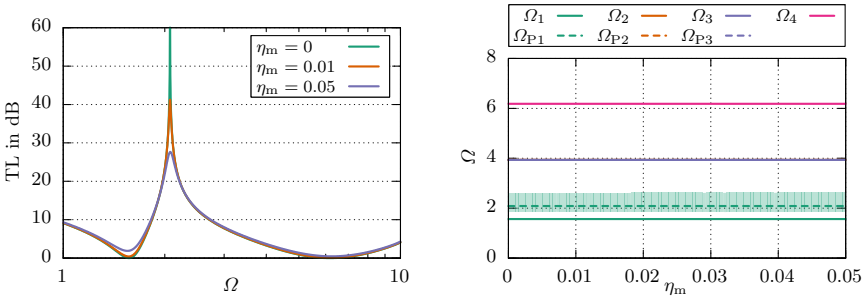

(a) Transmission loss. **(b)** Resonance and peak frequencies.

Figure 2.18: Parameter variation of the membrane loss factor η_m.

the MAM resonances and anti-resonances, respectively. Consequently, the TL maxima are diminished as η_m increases and the resonance minima become greater than zero. The peak bandwidth is not improved by a higher membrane loss factor, as can be seen in Fig. 2.18(b). This is because the resulting complex membrane stiffness matrix leads to a cropped peak which is not significantly broadened compared to the undamped case (see Fig. 2.18(a)). Thus, the main practical purpose of η_m is to reduce the TL dips at the MAM resonance frequencies at the cost of also reducing the TL peak values.

Mass magnitude: The influence of the nondimensional mass magnitude μ on the MAM transmission loss and the MAM (anti-)resonances is illustrated in Fig. 2.19. Many previous investigators (e.g. [10, 54, 63, 107, 112]) have already considered the effect of the added mass on the acoustic properties of MAMs. Thus, the results in Fig. 2.19 will only be discussed briefly.

Since a higher mass μ increases the inertia of both translational and rotational motion of the added mass, the first three eigenfrequencies

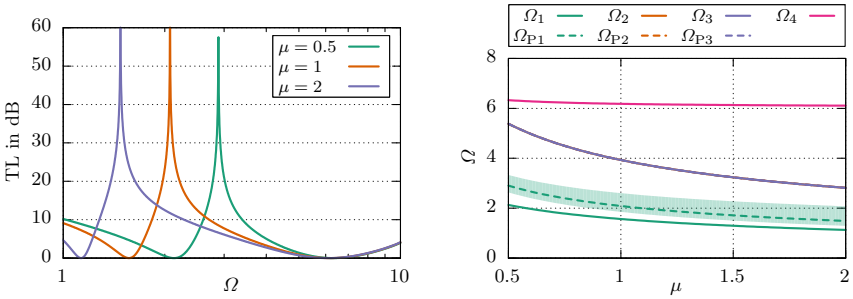

(a) Transmission loss. **(b)** Resonance and peak frequencies.

Figure 2.19: Parameter variation of the nondimensional added mass magnitude μ.

and anti-resonance frequencies of the MAM are decreased, as can be seen in Fig. 2.19(b). In fact, Ω_1 to Ω_3 as well as Ω_{P1} to Ω_{P3} are all proportional to $1/\sqrt{\mu}$ for the given MAM unit cell configuration. This agrees well with the findings of other researchers [10, 54, 63, 112]. The fourth MAM mode is governed by the mass being nearly at rest. Therefore, Ω_4 exhibits only a small sensitivity with respect to μ and remains nearly constant for large added mass magnitudes. However, when the nondimensional surface mass density of the added mass becomes small, so that $\mu\Lambda < 1$, the fourth eigenfrequency begins to increase for smaller values of μ. The reason is that in this regime the surface mass density of the membrane material is larger than that of the added mass and the added mass does not have enough inertia compared to the membrane material to stay at rest.

In Fig. 2.19(a) it is apparent that the TL peak becomes broader as μ is increased. But since the total weight of the MAM also increases with μ and so does the corresponding mass-law transmission loss, the indicated +10 dB-bandwidth of the first anti-resonance in Fig. 2.19(b) increases only marginally. Therefore, the added mass magnitude is pri-

marily suitable for tuning the first three resonance and anti-resonance frequencies of the MAM.

Mass radius of gyration: Since the mass is placed in the MAM center and the nondimensional squared radius of gyration ϑ is only related to the rotational inertia of the mass, just the MAM eigenmodes associated with Ω_2 and Ω_3 are affected by a variation of ϑ. Because these modes do not couple with the surrounding fluid for the given MAM configuration, there is no difference between the TL-curves for different values of ϑ visible in Fig. 2.20(a). However, the dependence of Ω_2 and Ω_3 on ϑ becomes visible in Fig. 2.20(b). It can be seen that – similar to the nondimensional mass magnitude μ – these two eigenfrequencies are proportional to $1/\sqrt{\vartheta}$, except for very small values of ϑ where the rotational inertia of the membrane material becomes important. The other (anti-)resonance frequencies are constant, because they are only governed by a translational motion of the centrally placed mass.

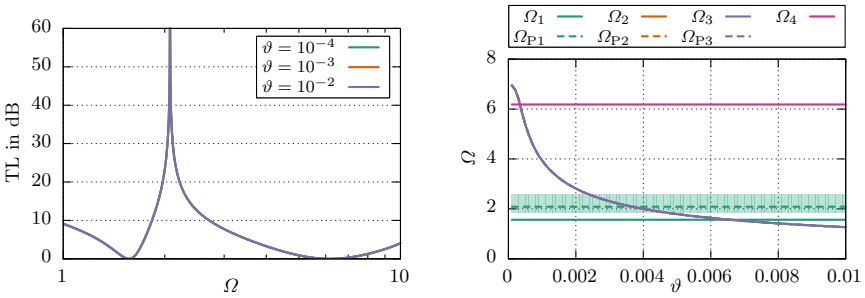

(a) Transmission loss. **(b)** Resonance and peak frequencies.

Figure 2.20: Parameter variation of the nondimensional squared radius of gyration ϑ of the added mass.

Mass diameter: The mass diameter is another MAM parameter that has been studied extensively in the literature (e.g. in [10, 54, 66]). The normal incidence sound transmission loss TL and the (anti-)resonance frequencies of the given MAM configuration are shown in Fig. 2.21 for different values of the nondimensional mass diameter δ_M. It can be seen that for larger diameters the TL spectrum of the MAM is shifted towards higher frequencies. Fig. 2.21(b) reveals that all resonance and anti-resonance frequencies increase as the mass diameter becomes bigger. An explanation for this is the larger membrane area covered by the mass and the resulting reduced membrane surface which can vibrate freely. This reduces the overall compliance of the membrane and therefore the MAM resonance frequencies increase. Closer inspection of the resonance frequency variations shows that for low values of δ_M the two rotational resonance frequencies grow faster than the resonance frequencies of the two translational modes Ω_1 and Ω_4. With increasing δ_M the curves for Ω_2 and Ω_3 flatten out and become similar to the shape of the Ω_4-curve. It is possible to explain this behavior with the rotational inertia of the membrane material attached to the mass, which

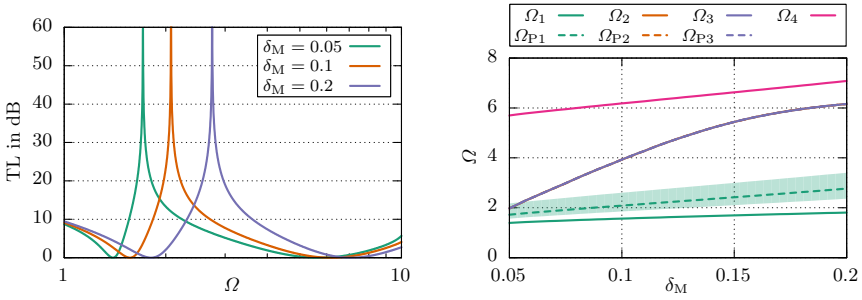

(a) Transmission loss. **(b)** Resonance and peak frequencies.

Figure 2.21: Parameter variation of the nondimensional mass diameter δ_M.

is proportional to δ_{M}^4. Since the rotational inertia of the added mass is kept constant, the inertia of the membrane material may become comparable to the mass inertia at some mass diameter δ_{M}. Similar to what has been observed for ϑ in Fig. 2.20(b), this leads to an effective reduction of the stiffening effect of the reduced free membrane surface for the rotational MAM modes.

As indicated in Fig. 2.21(b), the bandwidth of the first anti-resonance peak increases as the added mass becomes larger. This is a consequence of the enhanced eigenfrequency spreading, similar to the effect of the membrane bending stiffness, as shown in Fig. 2.17(b). Thus, the nondimensional mass diameter δ_{M} can be used to tune the MAM (anti-)resonance frequencies and the peak bandwidth without changing the total weight of the MAM.

Mass eccentricity: The eccentric positioning of the mass is investigated in two different cases: Fig. 2.22 shows the TL results and (anti-)resonance shiftings of the MAM when the mass position is var-

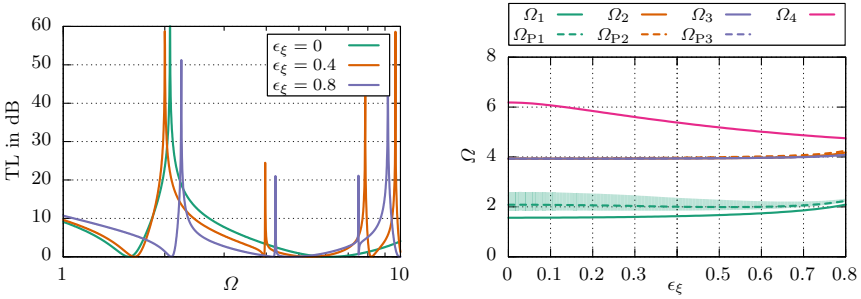

(a) Transmission loss. **(b)** Resonance and peak frequencies.

Figure 2.22: Parameter variation of the nondimensional mass eccentricity ϵ_ξ with the mass center of gravity coordinates $\xi^* = 0.5 + \epsilon_\xi/2$ and $\eta^* = 0.5$.

ied along the symmetry axis of the membrane in ξ-direction. The mass eccentricity is quantified using the nondimensional parameter ϵ_ξ, which relates to the ξ-coordinate of the mass center of gravity via $\xi^* = 0.5 + \epsilon_\xi/2$, and $\eta^* = 0.5$. In Fig. 2.22(a) it can be seen that for non-zero mass eccentricities an additional anti-resonance peak appears at $\Omega \approx 4$. The reason for this is that the second MAM mode (see Fig. 2.15) is not antisymmetric anymore and therefore couples with the surrounding fluid. As ϵ_ξ is increased, the first three MAM resonance frequencies shown in Fig. 2.22(b), which are mainly governed by rigid body motions of the added mass, remain nearly constant except when the mass comes close to the MAM edge and ϵ_ξ approaches 1. The additional stiffness induced by the nearby simply supported MAM edge then leads to a slight increase of the MAM resonance frequencies Ω_1 to Ω_3. The fourth MAM resonance frequency Ω_4 is affected differently by the mass eccentricity. Since this mode is dominated by the motion of the free MAM surface, the effective stiffness of this part of the MAM induced by the simply supported boundaries and the added mass is important for Ω_4. As the mass moves closer to one of the boundaries, the added stiffness effect of the mass overlaps with that of the nearby boundary and is therefore diminished. Thus, as can be seen in Fig. 2.22(b), Ω_4 decreases with increasing ϵ_ξ. Consequently, the MAM eigenfrequencies are squeezed together when the mass placement becomes more eccentric. As explained above, this also leads to a reduction of the anti-resonance peak bandwidths, as observed in Figs. 2.22(a) and 2.22(b).

The second parametric study for the mass eccentricity is shown in Fig. 2.23, where the mass is positioned along a circle around the MAM center with a radius of $\epsilon_\xi/2 = 0.4$ and a polar angle ϕ^*. Thus, the mass center of gravity coordinates are given by $\xi^* = 0.5 + \epsilon_\xi \cos\phi^*/2$ and $\eta^* = 0.5 + \epsilon_\xi \sin\phi^*/2$, respectively. Due to the square MAM shape and the axisymmetric cylindrical mass, the transmission loss results

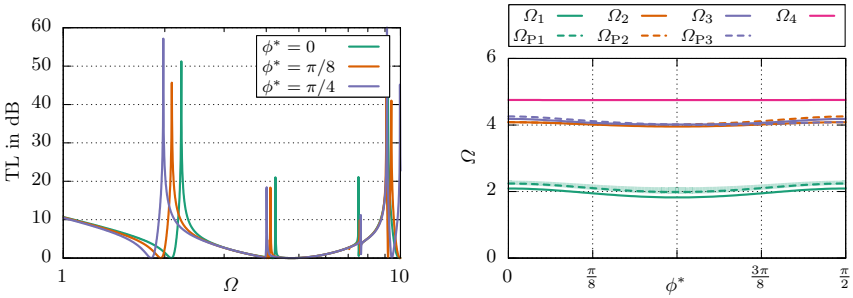

(a) Transmission loss. **(b)** Resonance and peak frequencies.

Figure 2.23: Parameter variation of the nondimensional mass eccentricity angle ϕ^* with the mass center of gravity coordinates $\xi^* = 0.5 + \epsilon_\xi \cos\phi^*/2$ and $\eta^* = 0.5 + \epsilon_\xi \sin\phi^*/2$. The radial displacement is fixed at $\epsilon_\xi = 0.8$.

in Fig. 2.23(a) are only shown for three values of ϕ^* up to $\phi^* = \pi/4$. Higher values of ϕ^* are redundant due to symmetry reasons, as can be seen in Fig. 2.23(b) where the (anti-)resonance frequency variation curves are symmetric to the vertical at $\phi^* = \pi/4$.

Apart from a slight shifting of the first three (anti-)resonances to lower frequencies as the mass position approaches the MAM diagonal, no significant difference between the TL spectra in Fig. 2.23(a) can be observed. The fourth MAM resonance frequency in Fig. 2.23(b) appears to be nearly independent of ϕ^*. Therefore, placing an eccentric mass on the diagonal of the MAM is slightly favorable compared to a mass placement on the horizontal or vertical symmetry axis of the MAM. This is a result of the higher spread between the first MAM eigenfrequency and the other resonance frequencies.

Fluid characteristic impedance: The dependency of the MAM transmission loss TL and (anti-)resonance frequencies on the non-dimensional characteristic impedance of the fluid $\mathcal{Z}_0$ is shown in Fig. 2.24.

Since in the long wavelength limit approximation $\mathcal{Z}_0$ appears only in Eq. (2.70) and the nondimensional effective surface mass density is obtained from the in vacuo response of the MAM, the resonance and anti-resonance frequencies are not affected by $\mathcal{Z}_0$. This is confirmed in Fig. 2.24(b), where the characteristic frequencies of the MAM are constant.

There is, however, a big influence on the bandwidth of the anti-resonance peak: $\mathcal{Z}_0$ is a measure for the characteristic impedance of the fluid in relation to the MAM impedance. This means, if $\mathcal{Z}_0$ is large, the MAM can be regarded as "light" compared to the surrounding fluid and the transmission loss of the MAM is considerably reduced. Consequently, the peak bandwidth is greatly reduced when $\mathcal{Z}_0 \gg 1$. Therefore, the nondimensional characteristic impedance should be chosen as low as possible (preferably $\mathcal{Z}_0 < 1$) to ensure large peak bandwidths without any mass penalty.

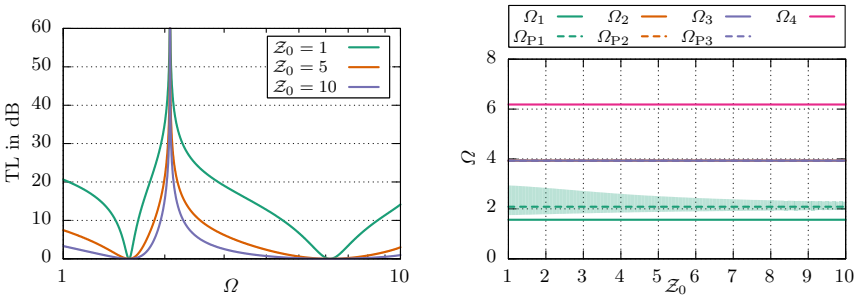

(a) Transmission loss. **(b)** Resonance and peak frequencies.

Figure 2.24: Parameter variation of the nondimensional characteristic impedance $\mathcal{Z}_0$ of the fluid.

2.5.2. MAM array

In the previous subsection, the parameter studies of a MAM unit cell showed how the different nondimensional parameters affect the acoustical properties of MAMs in the low-frequency regime. A MAM array consists of N_C unit cells and therefore a very large number of possibilities exists to tune the acoustic properties of the array. However, this parameter space can be substantially reduced when considering the long wavelength limit: As shown in Section 2.3.2, only the nondimensional effective surface mass densities $\mu''_{\mathrm{eff},pq}$ of the MAM unit cells are important and not the specific unit cell design details. Therefore, it suffices to only investigate the effect of variable μ''_eff-spectra across the MAM array. This can be achieved by suitable combinations of the nondimensional MAM unit cell parameters or a variation of the cell-specific nondimensional membrane prestress τ_{pq}.

The parameter studies of the MAM array investigate the influence of the following nondimensional parameters on the sound transmission properties of the array: the number of unit cells $N_\mathrm{C} = N_{\mathrm{C}x} N_{\mathrm{C}y}$ and the nondimensional unit cell prestress distribution τ_{pq} along the array, which represents the variation of μ''_eff-spectra between the unit cells. The basic properties of the investigated array are given in Table 2.2 denoted by configuration A-PAR1. This corresponds to a 4×4-array of MAM unit cells with the properties of unit cell configuration PAR1 given in Table 2.1. The prestress distribution of the basic array design is uniform with $\tau_{pq} = 1 = \mathrm{const}$. Since the unit cells of the array are considerably smaller than the acoustic wavelength within the investigated frequency range, the effective mass model from Section 2.2.3 was employed to conduct the parameter studies.

Number of unit cells: The calculated normal incidence transmission loss spectra of the MAM array panel for different numbers of unit cells are shown in Fig. 2.25. Additionally, the TL of the infinite array cal-

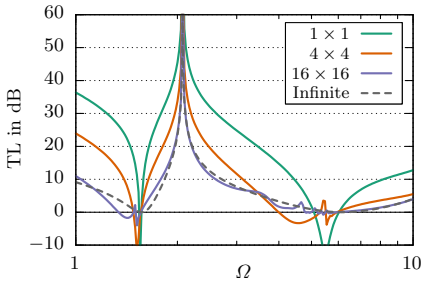

Figure 2.25: Parameter variation of the number of MAM array unit cells $N_C = N_{Cx} \times N_{Cy}$.

culated using the unit cell model given in Section 2.1.4 is shown as comparison. It can be seen that for the smallest possible array with only one unit cell the TL-values are the largest, except at the MAM resonance frequencies. With increasing array size, the array transmission loss reduces approximately by $10 \lg N_C$ until it converges to the infinite array transmission loss. As explained in Section 2.3.2, this is a consequence of the "windowing" effect by the aperture leading to higher transmission loss values for smaller panels [22, pp. 296–299].

Thus, the results in Fig. 2.25 show that even when the MAM array size is similar or even larger than the acoustic wavelength, the general qualitative features of the MAM sound transmission loss spectrum are retained, provided that the individual MAM unit cells are sub-wavelength sized. A small baffled MAM array will generally exhibit better TL-values, but a rigid baffle (as assumed in the analytical model) is difficult to realize in most practical cases. Large MAM arrays with uniform unit cell properties, on the other hand, can be well approximated using the infinite array model from Section 2.1. For example, the root-mean-square error between the TL-values for the 16×16-array shown in Fig. 2.25 and the infinite array results is only 1.4 dB.

Cell stress distribution: Two different cell stress distributions are considered in this parameter study: The first case represents a purposeful detuning of the MAM array unit cells in a checkerboard pattern, where the nondimensional prestress distribution is given by $\tau_{pq} = 1 \pm \Delta\tau/2$. The sign is switched for every other MAM cell and $\Delta\tau$ corresponds to the prestress spread between the detuned cells. In the second case, the nondimensional cell stresses are randomly distributed according to $\tau_{pq} = 1 + \sigma_\tau \mathcal{N}_{pq}$, where σ_τ is the standard deviation of the unit cell stresses within the array and $\mathcal{N}_{pq}$ is a random number drawn from the standard normal distribution.

The analytical results for the MAM array with checkerboard prestress distribution and a prestress spread ranging from $\Delta\tau = 0$ to 0.5 are shown in Fig. 2.26(a). For the non-uniform stress distribution results (i.e. $\Delta\tau > 0$) it can be seen that the single TL-minimum at $\Omega = 1.5$ corresponding to the first resonance frequency of the uniform MAM array is split up into two minima. These two minima correspond to the different first resonance frequencies of the MAM cells with the

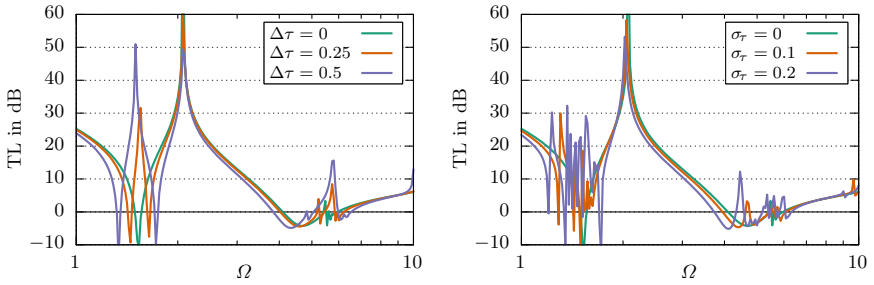

(a) Checkerboard distribution. **(b)** Random distribution.

Figure 2.26: Parameter variation of the nondimensional prestress distribution τ_{pq} within the MAM array.

reduced prestress (i.e. a lower first resonance frequency $\Omega_1^{(\mathrm{low})}$) and increased prestress (i.e. a higher first resonance frequency $\Omega_1^{(\mathrm{high})}$), respectively. Since the resonance frequencies of MAMs are proportional to the square root of the prestress resultant, these two eigenfrequencies are related to the prestress spread $\Delta\tau$ by

$$\frac{\Omega_1^{(\mathrm{high})}}{\Omega_1^{(\mathrm{low})}} = \sqrt{\frac{2+\Delta\tau}{2-\Delta\tau}}. \tag{2.112}$$

In between those minima, an additional TL-peak appears with its bandwidth increasing as the stress spread is increased. This additional peak in fact does not correspond to one of the anti-resonances of the detuned MAM unit cells. Much rather, this peak appears due to the specific vibrational behavior of the adjacent MAM unit cells, similar to what has been observed for MAM arrays with different added masses [113]: For frequencies slightly above $\Omega_1^{(\mathrm{low})}$, the vibration of the MAM cells with lower prestress exhibits a rapid phase reversal and becomes out-of-phase by nearly 180° compared to the MAM cells with higher prestress. At a certain frequency, the sound radiated by the out-of-phase MAM cells cancels out the sound radiated by the in-phase MAM cells and thus an additional maximum in the TL-spectrum can be observed. Since this peak is a consequence of the phase reversal at the MAM resonances, it appears in between the two first resonance minima of the different MAM unit cell classes.

The same effect happens between the two anti-resonances of the differently tuned MAM unit cells, because MAMs also exhibit a phase reversal at the anti-resonance frequencies. This means that the two anti-resonances of the different classes of MAMs are not retained in the array arrangement, but a single TL-maximum appears in between. For the given stress distribution, both anti-resonances are shifted by approximately the same amount in opposite directions. Therefore, the resulting TL-maximum of the whole array appears at roughly the same

frequency as the original peak of the uniform array (green curve in Fig. 2.26(a)). For higher values of the stress spread $\Delta\tau$, the bandwidth of this peak is reduced due to the MAM resonances moving closer to the anti-resonance. In summary, the results show that a checkerboard prestress distribution in a MAM array yields an additional peak in the transmission loss spectrum, approximately located at the first resonance frequency of the uniform MAM array. The original TL-peak is, except for a reduced bandwidth, not significantly affected by the prestress spread $\Delta\tau$.

The calculated TL of the MAM array with random prestress distribution is shown in Fig. 2.26(b). The prestress standard deviation ranges from $\sigma_\tau = 0$ to 0.2. Similar to the effect already observed for the checkerboard stress distribution in Fig. 2.26(a), many different resonance minima appear in a frequency band around the first resonance of the uniform MAM array at $\Omega = 1.5$. These minima are caused by the randomly shifted first resonance frequencies of the cells within the array and the affected frequency band widens with increasing standard deviation σ_τ. Additionally, narrowband TL-peaks appear between those resonance minima. These are caused analogously to the checkerboard cell stress distribution by certain out-of-phase cells compensating the sound radiation of other in-phase cells. In practice, it can be expected that these narrowband minima and maxima will be smeared out due to damping within the membrane material and the mounting of the MAM array. The original TL-peak of the array is not significantly affected by the random cell stress distribution, except for a slight shifting to lower frequencies. This corresponds to the observations in Fig. 2.26(a) for the checkerboard stress pattern and the mean value of τ_{pq} being equal to 1 (i.e. the nondimensional prestress of the uniform MAM array). In summary, these results show that a random cell prestress distribution does not significantly affect the main anti-resonance of the array. Such random cell prestress distributions can be caused in practice, for example,

by tolerances in the manufacturing process of a MAM array. Contrary to the checkerboard distribution, the additional anti-resonances forming around the first resonance are too narrowband to be of practical significance.

3. Modeling of multi-layered structures with MAMs

3.1. Analytical model for multi-layered structures

While there has been some effort by other investigators to analytically model the transmission of sound through MAM unit cells, the modeling of multi-layered arrangements involving MAMs has received little attention in the present literature. Yang et al. [108] reported that stacking multiple layers of MAMs yields a much more broadband performance as compared to the narrowband characteristic of individual MAM cells. Some numerical simulations of stacked MAMs have been performed by Ma [53] and Naify et al. [66] in order to investigate certain parameters, such as the MAM spacing or the added mass magnitude on each membrane layer. However, both investigations do not provide a suitable framework for predicting the performance of multi-layered structures involving MAMs without the use of numerical simulations. Also, MAMs have not been investigated in combination with conventional elements found in noise protection, such as walls, porous layers, or Helmholtz resonators.

In the first part of this section, the transfer matrix model is introduced which is used to analyze the acoustic properties of multi-layered structures with MAMs. The second part provides a simplified methodology for calculating the resonance and anti-resonance frequencies of multi-layered systems containing walls and MAMs.

3.1.1. Transfer matrix model

As explained in Section 2.4 in the context of the impedance tube measurements, the acoustic transfer matrices $\mathbf{T}$, as defined in Eq. (2.109), can be used to characterize the acoustic properties of planar structures [2]. The transfer matrix elements T_{11}, T_{12}, T_{21}, and T_{22} are, in general, complex-valued. Apart from the material and geometrical properties of the particular element, the transfer matrix elements also depend on the frequency and the angle of incidence θ_i of the incoming plane sound wave.

Once known, the transfer matrix elements allow the calculation of the oblique incidence transmission factor $\tilde{t}_{\theta_\mathrm{i}}$ and reflection factor $\tilde{r}_{\theta_\mathrm{i}}$ of the element using [9]

$$\tilde{t}_{\theta_\mathrm{i}} = \frac{2}{T_{11} + T_{12}\cos\theta_\mathrm{i}/Z_0 + T_{21}Z_0/\cos\theta_\mathrm{i} + T_{22}} \quad \text{and} \tag{3.1}$$

$$\tilde{r}_{\theta_\mathrm{i}} = (T_{11} + T_{12}\cos\theta_\mathrm{i}/Z_0)\,\tilde{t}_{\theta_\mathrm{i}} - 1, \tag{3.2}$$

assuming the same fluid on both the incidence and transmission side of the element. If a multi-layered structure with N_lay different layers is considered, the transfer matrix $\mathbf{T}$ of the whole structure is given by

$$\mathbf{T} = \mathbf{T}_\mathrm{I} \cdot \mathbf{T}_\mathrm{II} \cdot \ldots \cdot \mathbf{T}_{N_\mathrm{lay}} = \prod_{i=\mathrm{I}}^{N_\mathrm{lay}} \mathbf{T}_i, \tag{3.3}$$

where $\mathbf{T}_i$ are the transfer matrices of each individual layer. The index $i = \mathrm{I}$ corresponds to the outermost layer on the incident side of the structure.

The transfer matrix $\mathbf{T}_i$ of a certain acoustic element can be obtained using analytical models, experiments [3], or numerical simulations. For a fluid layer i with thickness d_i (such as layers II and IV in the example system shown in Fig. 3.1), the transfer matrix $\mathbf{T}_i^{(\mathrm{F})}$ is given by [2, p. 245]

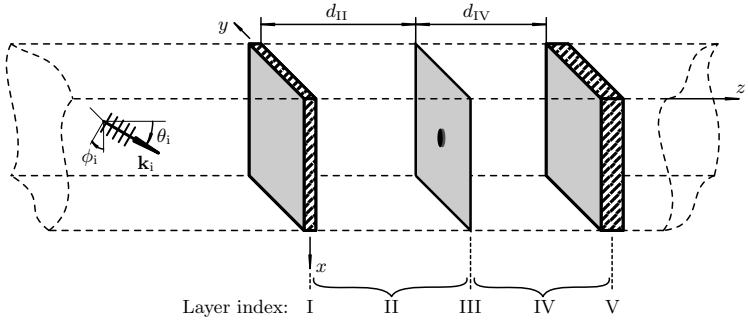

Figure 3.1: Example for a multi-layered system with a total of five different layers: two walls (layers I and V), two fluid layers (II and IV), and one MAM layer (III).

$$\mathbf{T}_i^{(\mathrm{F})} = \begin{bmatrix} \cos(k_{z,i}d_i) & \frac{\mathrm{i}\omega\rho_{0,i}}{k_{z,i}}\sin(k_{z,i}d_i) \\ -\frac{k_{z,i}}{\mathrm{i}\omega\rho_{0,i}}\sin(k_{z,i}d_i) & \cos(k_{z,i}d_i) \end{bmatrix}, \tag{3.4}$$

where $k_{z,i}$ is the z-component of the acoustic wave vector $k_{0,i}$ and $\rho_{0,i}$ is the fluid density inside the i-th fluid layer. $k_{z,i}$ follows from the dispersion relation $k_{z,i}^2 = k_{0,i}^2 - k_0^2 \sin^2\theta_{\mathrm{i}}$ with the acoustic wave number k_0 and incidence angle θ_{i} of the incident plane wave. If the fluid inside the fluid layer has the same properties as the fluid on the incident side of the multi-layered structure, it simply follows that $k_{z,i} = k_{\mathrm{i}z} = k_0 \cos\theta_{\mathrm{i}}$.

Limp porous materials (e.g. glass fiber blankets or open-celled foams) can be represented by the fluid layer transfer matrix in Eq. (3.4) using an equivalent fluid model [2, p. 252]. In this case, $\rho_{0,i}$ is replaced by an equivalent density $\rho_{\mathrm{eq,limp}}$ and $k_{z,i}$ is obtained from the dispersion relation with $k_{0,i}$ replaced by the effective wave number $k_{\mathrm{eq}} = \omega\sqrt{\rho_{\mathrm{eq,limp}}/K_{\mathrm{eq}}}$, where K_{eq} is the equivalent bulk modulus of the po-

rous material. $\rho_{\mathrm{eq,limp}}$ can be calculated using [2, p. 253]

$$\rho_{\mathrm{eq,limp}} \approx \frac{\rho_{\mathrm{tot}}\rho_{\mathrm{eq}} - \rho_0^2}{\rho_{\mathrm{tot}} + \rho_{\mathrm{eq}} - 2\rho_0}, \tag{3.5}$$

where $\rho_{\mathrm{tot}} = \rho + \chi\rho_0$ is the (apparent) total density of the porous material, ρ is the density of the frame or fiber structure (as specified e.g. by the manufacturer), and χ is the porosity of the material. The equivalent quantities ρ_{eq} and K_{eq} can be obtained from empirical models, such as the well-known Champoux-Allard model [1].

In case of an acoustically thin wall (such as layers I and V in Fig. 3.1), the analytical transfer matrix $\mathbf{T}_i^{(\mathrm{W})}$ is

$$\mathbf{T}_i^{(\mathrm{W})} = \begin{bmatrix} 1 & Z_{\mathrm{W},i} \\ 0 & 1 \end{bmatrix}, \tag{3.6}$$

where $Z_{\mathrm{W},i} = \mathrm{i}\omega m_i''(1 - (\omega/\omega_{\mathrm{cr},i})^2 \sin^4\theta_{\mathrm{i}})$ is the mechanical wall impedance with the surface mass density m_i'' and critical frequency $\omega_{\mathrm{cr},i}$ of the wall [2, p. 255].

For the modeling of MAMs (e.g. layer III in Fig. 3.1) using the transfer matrix method, the following simplification is applied: Since the transfer matrix method assumes the propagation of plane waves inside the multi-layered structure [2], it seems reasonable to require the MAM unit cells to be of sub-wavelength size within the frequency range of interest. Consequently, as discussed in Section 2.1, only plane waves are radiated by the MAMs and the sound transmission through the MAMs can be characterized using the nondimensional effective surface mass density μ_{eff}'', as defined in Eq. (2.71). The effective mechanical impedance is related to the effective surface mass density via $Z_{\mathrm{eff}} = \mathrm{i}\omega m_{\mathrm{m}}''\mu_{\mathrm{eff}}''$. Using the expression for a transfer matrix of a wall in Eq. (3.6) and replacing the wall impedance $Z_{\mathrm{W},i}$ by the effective

impedance, the following transfer matrix for a MAM is obtained:

$$\mathbf{T}_i^{(\mathrm{MAM})} = \begin{bmatrix} 1 & \mathrm{i}\omega m''_{\mathrm{m},i}\mu''_{\mathrm{eff},i} \\ 0 & 1 \end{bmatrix}. \tag{3.7}$$

3.1.2. Resonance and anti-resonance frequencies of multi-layered structures

Since all the different layers in a multi-layered acoustic material together form a dynamically coupled system, such systems can exhibit resonance and anti-resonance frequencies, where the sound transmission loss drops significantly or reaches comparatively high values, respectively. A typical example for a resonance frequency of multi-layered systems is the mass-air-mass resonance frequency of a double wall (see Fig. 1.2(b)), which is caused by the two walls acting as masses and the air gap in between acting as a spring. Since such resonance frequencies impair the performance of multi-layered acoustic treatments, they should be estimated a-priori. By this means, suitable countermeasures can be applied in the design process and the negative influence of the system resonances can be reduced.

For multi-layered systems consisting only of thin, limp walls with surface mass densities m''_i and air gaps, the resonance frequencies can be readily obtained as the resonance frequencies of a corresponding multiple degrees of freedom (DOF) mass-spring-oscillator [50]. But if MAMs are included, this approach is not as straightforward, since the dynamic properties of MAMs are more complex than those of simple walls. However, this complication can be eliminated by employing the effective surface mass density approximation and representing the MAM layers by discrete masses with a *frequency-dependent* surface mass density $m''_i(\omega) = m''_{\mathrm{m},i}\mu''_{\mathrm{eff},i}$. This approach is illustrated in Fig. 3.2 for the example system in Fig. 3.1. The two walls are represented by simple masses with constant surface mass densities m''_{I} and

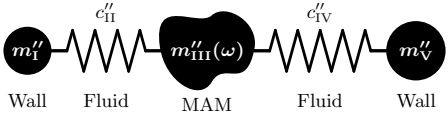

Figure 3.2: 3DOF-oscillator representation of the multi-layered system shown in Fig. 3.1.

m''_{V}, assuming that the frequency f is well below the critical frequencies of the panels. If the thickness d_i of the fluid layers is much smaller than the acoustic wavelength, then the surface spring stiffness of the air gaps is given by $c''_i = \rho_{0,i} c^2_{z,i}/d_i$, where $c_{z,i} = \omega/k_{z,i}$ is the z-component of the phase velocity vector within the i-th fluid layer. If the fluid has the same properties as the ambient fluid, $c_{z,i}$ is given by $c_{z,i} = c_0/\cos\theta_{\mathrm{i}}$ and, consequently, $c''_i = \rho_0 c_0^2/(d_i \cos^2\theta_{\mathrm{i}})$.

From the equations of motion for the discrete masses coupled with springs in Fig. 3.2, the frequency-dependent dynamic stiffness matrix $\mathbf{D}(\omega)$ can be assembled as

$$\mathbf{D}(\omega) = \begin{bmatrix} c''_{\mathrm{II}} - \omega^2 m''_{\mathrm{I}} & -c''_{\mathrm{II}} & 0 \\ -c''_{\mathrm{II}} & c''_{\mathrm{II}} + c''_{\mathrm{IV}} - \omega^2 m''_{\mathrm{III}}(\omega) & -c''_{\mathrm{IV}} \\ 0 & -c''_{\mathrm{IV}} & c''_{\mathrm{IV}} - \omega^2 m''_{\mathrm{V}} \end{bmatrix}. \quad (3.8)$$

The assembly of the dynamic stiffness matrix $\mathbf{D}(\omega)$ for other multi-layered systems follows analogously. The resonance frequencies of the multi-layered system $\omega_i = 2\pi f_i$ correspond to the frequencies for which $\mathbf{D}(\omega)$ becomes singular. Thus, the ω_i can be calculated by solving the characteristic equation

$$\det \mathbf{D}(\omega_i) \stackrel{!}{=} 0, \quad (3.9)$$

where it has to be taken into account that for MAM layers the effective surface mass densities are also functions of ω. The anti-resonance frequencies of the system, $\omega_{\mathrm{P}i}$, on the other hand correspond to those

frequencies for which the rightmost layer exhibits a vanishing vibration amplitude for a given excitation pressure at the leftmost layer. Comparable to Section 2.1.4, the rank of the Rosenbrock system matrix

$$\mathbf{P}(\omega_{\mathrm{P}i}) = \left[\begin{array}{ccc:c} & & & 1 \\ & \mathbf{D}(\omega_{\mathrm{P}i}) & & 0 \\ & & & \vdots \\ & & & 0 \\ \hdashline 0 & \cdots & 0 \; 1 & 0 \end{array}\right] \tag{3.10}$$

drops from its usual value at these anti-resonance frequencies.

3.2. Numerical verification

For the numerical verification of the transfer matrix model for multi-layered structures with MAMs, a similar finite element model as in the verification of the MAM unit cell model in Section 2.3.1 is used. An illustration of the basic numerical setup is given in Fig. 3.3. The investigated multi-layered structure is similar to the example structure shown in Fig. 3.1: The first layer at $z = 0$ is a thin wall modeled using two-dimensional shell elements with a surface mass density (relative to the surface mass density of the membrane material m''_{m}) of $m''_{\mathrm{I}} = 5m''_{\mathrm{m}}$ and a nondimensional critical frequency at $\Omega_{\mathrm{cr,I}} = \omega_{\mathrm{cr,I}}/\omega_{\mathrm{ref}} = 400$. Layer II is a fluid layer of thickness $d_{\mathrm{II}} = 0.5L_x$, which is followed by a MAM layer with properties corresponding to configuration VV1 in Table 2.1. The next layer IV is another fluid layer with thickness $d_{\mathrm{IV}} = 0.3L_x$. The last layer is another thin wall with $m''_{\mathrm{V}} = 10m''_{\mathrm{m}}$ and $\Omega_{\mathrm{cr,V}} = 200$. An overview of the investigated layers and the associated properties is provided in Table 3.1.

The model consists of a box-shaped domain with lateral dimensions in x- and y-direction corresponding to one MAM unit cell and Bloch-

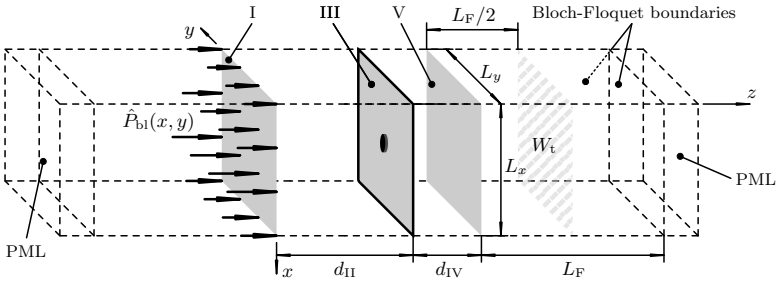

Figure 3.3: Basic setup of the numerical model used for the validation of the transfer matrix model (not to scale). The properties of the layers I to V are given in Table 3.1.

Floquet boundary conditions applied to the lateral surfaces of the domain. The edges of the two wall layers are not constrained in order to model laterally unbounded walls. The edges of the MAM, on the other hand, are simply supported. In z-direction, the fluid domains are truncated by perfectly matched layers. The first wall is excited by a blocked pressure field as given in Eq. (2.108) and the transmitted sound power W_t is obtained from integrating the z-component of the acoustic intensity vector along a surface $L_F/2$ away from the last layer of the structure (see Fig. 3.3). The discretization and solution procedure is the same as already described for the MAM unit cell model

Table 3.1: Layer properties of the multi-layered system shown in Fig. 3.3.

Layer:	I	II	III	IV	V
Type:	Wall	Air gap	MAM	Air gap	Wall
Properties:	$\frac{m''_I}{m''_n} = 5$	$\frac{d_{II}}{L_x} = 0.5$	VV1	$\frac{d_{IV}}{L_x} = 0.3$	$\frac{m''_V}{m''_n} = 10$
	$\frac{\omega_{cr,I}}{\omega_{ref}} = 400$				$\frac{\omega_{cr,V}}{\omega_{ref}} = 200$

verification in Section 2.3.1.

The resulting transmission loss curves are shown in Figs. 3.4(a) and 3.4(b) for normal incidence and oblique incidence with $\theta_\mathrm{i} = 60°$ and $\phi_\mathrm{i} = 30°$, respectively. The solid line represents the analytical results from the proposed transfer matrix model and the circles correspond to the FEM simulations. Additionally, the transmission loss spectra of the MAM unit cell VV1 are provided for comparison. An excellent agreement between the analytical results and the numerical simulations can be observed in both cases, except at higher frequencies where κ_0 approaches unity. As already observed in Section 2.3.1 for the MAM unit cell model, this is caused by the simplifications in the effective mass approximation and the neglect of fluid loading effects when calculating the effective surface mass density of the MAM. Nevertheless, the good agreement indicates that the transfer matrix method is an adequate method for calculating the acoustic transmission properties of laterally unbounded multi-layered structures involving MAM layers, as long as

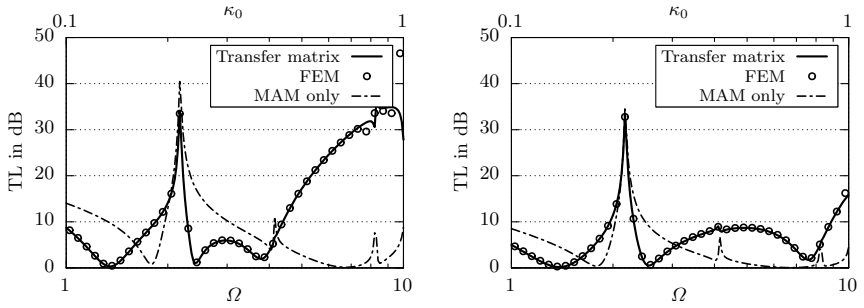

(a) $\theta_\mathrm{i} = 0°$.

(b) $\theta_\mathrm{i} = 60°$.

Figure 3.4: Normal and oblique incidence sound transmission loss of the multi-layered structure with a MAM layer given in Table 3.1 as obtained from the analytical model and the FEM simulations.

the long wavelength limit criterion is met.

When comparing the multi-layered TL with the transmission loss of the individual MAM layer in Fig. 3.4(a), it can be seen that the first TL peak of the MAM is at the same anti-resonance frequency Ω_{P1} as in the TL spectrum of the multi-layered system. A closer inspection of the results reveals that this is also true for the second anti-resonance peak, which is not as clearly visible in the multi-layered TL spectrum as the first anti-resonance. Consequently, these results indicate that the MAM anti-resonance frequencies are not affected within a multi-layered structure. The bandwidth of the TL peaks, however, is reduced in the multi-layered setup. This happens because the multi-layer resonances, which are visible as TL minima in Fig. 3.4, influence the MAM anti-resonances. In particular, the second resonance frequency of the multi-layered structure is very close to the first MAM anti-resonance frequency, so that the TL drops off much more rapidly than in case of the single MAM layer, where the second resonances frequency is much higher. Since the air layer stiffnesses are depending on θ_{i}, the multi-layer resonance frequencies and peak bandwidths also depend on the inclination angle of the incident plane wave, as can be seen by comparing Figs. 3.4(a) and 3.4(b).

The unaffected MAM anti-resonances in the multi-layered structure can be explained using the illustrations in Fig. 3.5, where the qualitative displacement of a MAM in front of a wall is shown at the first resonance frequency and the first anti-resonance frequency of the MAM. In Fig. 3.5(a), the MAM displacement at the first resonance is in-phase across the whole MAM surface. Thus, the air volume enclosed by the MAM layer and the wall is alternately compressed and expanded, as indicated by the arrows in Fig. 3.5(a). Therefore, the MAM resonance is affected by the added stiffness due to the compression/expansion of the air layer. In case of the anti-resonance, however, some parts of the MAM vibrate out-of-phase (see Fig. 3.5(b)). Since the high TL-values

(a) Resonance. **(b)** Anti-resonance.

Figure 3.5: Qualitative displacement of a MAM in front of a wall at the first MAM resonance frequency and the first MAM anti-resonance frequency.

at a MAM anti-resonance are caused by the average displacement of the MAM being nearly zero, the volume of the air layer remains constant and no added stiffness is experienced by the MAM. In fact, the air between the wall and the MAM layer is just moved back and forth between the region around the added mass and the outer perimeter of the MAM. Therefore, the MAM anti-resonances are unchanged within a multi-layered setup.

Additional simulations were performed with a slightly different arrangement of the multi-layered structure given in Table 3.1. In order to also verify the transfer matrix model for arrangements with MAM layers closely positioned to other layers (e.g. walls), the air gap heights d_{II} and d_{IV} are changed to $d_{\mathrm{II}}/L_x = 0.7$ and $d_{\mathrm{IV}}/L_x = 0.1$, respectively. This means that the MAM layer is positioned very close to the second wall layer while keeping the total height of the multi-layered structure constant. The resulting TL curves are shown in Fig. 3.6 for normal and oblique incidence. Again a very good agreement between the transfer matrix predictions and the FEM results can be observed in both cases. Therefore, the acoustic near fields of the MAMs do not significantly affect the sound transmission properties of multi-layered structures, even when the MAM layers are positioned very close to other layers.

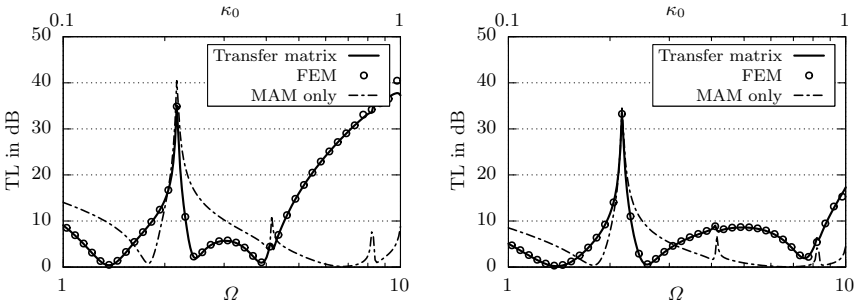

(a) $\theta_\mathrm{i} = 0°$. **(b)** $\theta_\mathrm{i} = 60°$.

Figure 3.6: Normal and oblique incidence sound transmission loss of a multi-layered structure similar to that in Table 3.1 with $d_\mathrm{II}/L_x = 0.7$ and $d_\mathrm{IV}/L_x = 0.1$.

3.3. Experimental validation

The transfer matrix model is validated using similar impedance tube measurements as in Section 2.4 for the validation of the MAM unit cell model. A multi-layered test sample consisting of the two MAM samples VV2 and VV3 from Section 2.4 separated by an air gap with a thickness of $d_\mathrm{II} = 10$ mm is mounted inside the steel adapter for the measurements. The properties of the layers are summarized in Table 3.2. Fig. 3.7(a) provides an illustration of the layering structure of the test

Table 3.2: Layer properties of the experimentally investigated multi-layered MAM system.

Layer:	I	II	III
Type:	MAM	Air gap	MAM
Properties:	VV2	$\frac{d_\mathrm{II}}{L_x} \approx 0.22$	VV3

sample. All remaining parameters and the experimental procedure are the same as in Section 2.4.

The experimental results and the predictions of the transfer matrix model for the normal incidence sound transmission loss between 50 and 1600 Hz are compared in Fig. 3.7(b). In general, a very good agreement between both results can be observed. The test sample exhibits two TL peaks at 260 Hz and 400 Hz, which correspond to the anti-resonance frequencies of the two MAM layers. This confirms that by stacking two differently tuned MAM layers, the anti-resonances of the individual layers are retained in the multi-layered arrangement [66]. Additionally, three TL minima can be observed within the investigated frequency range at 200 Hz, 310 Hz, and 1100 Hz. These can be attributed to the resonance frequencies of the multi-layered system and are accurately predicted by the transfer matrix model. For frequencies greater than 1000 Hz, it can be seen that the transfer matrix results underestimate the experimental results. As already explained in Section 2.4, this effect

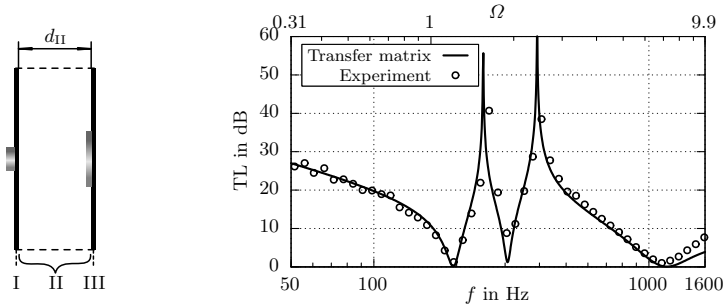

(a) Test sample layers. **(b)** Transmission loss.

Figure 3.7: Normal incidence sound transmission loss of the multi-layered structure with two MAM layers given in Table 3.2 as obtained from the analytical model and impedance tube measurements.

can be attributed to the simplifications in the effective surface mass density approximation for the MAM layers being inaccurate when the acoustic wavelength is comparable to the edge length of the MAM unit cells. However, since typical MAM structures are composed of sub-wavelength sized unit cells, the good agreement of the results in Fig. 3.7(b) in the low-frequency range indicates that the transfer matrix model is a suitable method for predicting the sound transmission loss of MAM unit cells in multi-layered arrangements.

3.4. Parameter studies

The transfer matrix method is used to perform parameter studies of a double wall design with an integrated MAM layer (see Fig. 3.1 for the layer arrangement). Thus, the influence of important design parameters on the sound reduction performance of a multi-layered noise shield design with MAM layers can be investigated. The parameters of the walls and the air gaps are systematically varied to study their influence on the transmission loss and (anti-)resonance frequencies of the multi-layered system. An overview of the properties of the different layers in the basic setup of this parameter study is given in Table 3.3. This corresponds to a symmetric arrangement with the same surface mass densities for the two walls $m''_{\mathrm{I}} = m''_{\mathrm{V}} = 50m''_{\mathrm{m}}$ and equal cavity heights $d_{\mathrm{II}} = d_{\mathrm{IV}} = 0.25L_x$, i.e. the MAM layer is placed in the middle between

Table 3.3: Layer properties of the basic multi-layered system for the parameter studies, similar to that shown in Fig. 3.1.

Layer:	I	II	III	IV	V
Type:	Wall	Air gap	MAM	Air gap	Wall
Properties:	$\frac{m''_{\mathrm{I}}}{m''_{\mathrm{m}}} = 50$	$\frac{d_{\mathrm{II}}}{L_x} = 0.25$	PAR1	$d_{\mathrm{IV}} = d_{\mathrm{II}}$	$m''_{\mathrm{V}} = m''_{\mathrm{I}}$

the walls. The properties of the MAM layer correspond to configuration PAR1 in Table 2.1 and remain constant for the subsequent calculations.

A general impression of the dynamic characteristics of the multi-layered structure can be obtained from investigating the first three mode shapes which are obtained as the eigenvectors of the dynamic stiffness matrix in Eq. (3.8). The qualitative modal displacements of the three masses from the 3DOF-oscillator representation are shown in Fig. 3.8. The first mode shape is primarily characterized by a uniform in-phase displacement of all three masses, which resembles a typical rigid body mode. The air layers are not compressed in this mode so that it can be expected that the first eigenfrequency of the multi-layered system does not exhibit a significant dependence on the air layer properties. In the second mode, the MAM layer displacement is negligible compared to the wall displacements. Additionally, the two walls exhibit an out-of-phase motion pattern with a strong compression and expansion of the air cavities between the walls and the MAM layer. Thus, this mode shape is similar to the mass-air-mass resonance

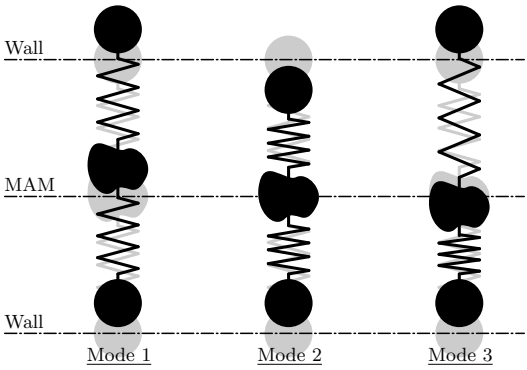

Figure 3.8: Equivalent 3DOF-oscillator representation of the first three mode shapes of the multi-layered system with the properties given in Table 3.3.

of a conventional double wall. The third mode shape is characterized by an in-phase motion of the two walls and an out-of-phase displacement of the MAM layer. Thus, the two inner air gap volumes are alternately compressed and expanded. Like in the first eigenmode, the total air volume between the walls, however, does not significantly change.

Wall surface mass densities: In Fig. 3.9, the results for the normal incidence TL and the (anti-)resonance frequencies of the multi-layered system are shown for a variation of the first wall surface mass density m''_{I} between $25m''_{\mathrm{m}}$ and $100m''_{\mathrm{m}}$. According to Table 3.3, the other wall surface mass density m''_{V} is set to be equal to m''_{I} so that the system remains symmetric. Fig. 3.9(a) shows the TL for three different values of the wall surface mass density. It can be seen that the transmission loss curves resemble that of a typical double wall structure, except for the peak and the additional resonances introduced by the MAM layer. Above a certain frequency which corresponds to the eigenfrequency of the second mode, the transmission loss increases by approximately

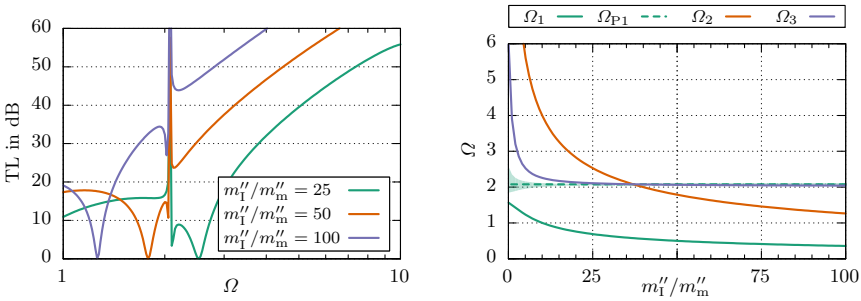

(a) Transmission loss. **(b)** Resonance and peak frequencies.

Figure 3.9: Parameter variation of the wall surface mass density m''_{I} with $m''_{\mathrm{V}} = m''_{\mathrm{I}}$.

18 dB per octave. Thus, the second eigenmode corresponds to the mass-air-mass resonance mode of a conventional double wall, which separates the mass-law governed frequency range from the high TL region. Following Eq. (1.5), this resonance frequency is shifted to lower frequencies as the surface mass densities of the walls are increased. The TL peak at $\Omega_{\mathrm{P1}} \approx 2.1$ is found to be very narrowband compared to the peak of the isolated MAM layer (see e.g. the green curve in Fig. 2.16(a)). This is because of the very close third resonance, which diminishes the anti-resonance and is not significantly affected by the surface mass densities of the walls.

This becomes more obvious in Fig. 3.9(b), where the (anti-)resonance frequencies of the multi-layered system are given in dependence of the nondimensional wall surface mass density $m''_{\mathrm{I}}/m''_{\mathrm{m}}$. It can be seen that the first two resonance frequencies decrease as the wall surface mass densities become larger. This is because the first mode exhibits a rigid body-type mode shape (see Fig. 3.8) and the second mode, as discussed above, corresponds to the mass-air-mass resonance of a double wall. As the wall surface mass densities become smaller than m''_{m}, Ω_1 approaches the first resonance frequency of the MAM, because the walls become transparent to the acoustic waves. The mass-air-mass-type resonance frequency Ω_2, however, approaches infinity as $m''_{\mathrm{I}} \to 0$, because it is inversely proportional to the square root of the total mass of the system. The third resonance frequency Ω_3, on the other hand, is nearly independent of the wall mass and remains close to the anti-resonance frequency Ω_{P3} for most values of m''_{I}. However, only when the wall surface mass densities approach zero, Ω_3 increases strongly and approaches the second resonance frequency of the MAM.

Additionally to the (anti-)resonance frequencies of the structure, the TL peak bandwidth is indicated in Fig. 3.9(b) as a shaded band. The bandwidth of an anti-resonance is in this case defined as the frequency band in which the TL of the multi-layered structure with MAM layer

exceeds the transmission loss of a reference double wall design by at least 10 dB. This reference corresponds to a conventional double wall with the same wall spacing as the MAM panel and the additional mass of the MAM layer evenly added to the two walls. It can be seen that the bandwidth of the anti-resonance peak is strongly diminished when $m''_{\mathrm{I}} \gg m''_{\mathrm{m}}$ due to the negative influence of the approaching third resonance frequency Ω_3. The reduced bandwidth for larger wall surface mass densities can also be interpreted as a masking effect due to the walls surrounding the MAM. Consequently, symmetric designs should be avoided when MAM layers are integrated within a double wall with large wall surface mass densities.

Wall mass ratio: In order to evaluate the sound reduction performance of an asymmetric arrangement, the ratio of the wall surface mass densities $m''_{\mathrm{I}}/m''_{\mathrm{V}}$ has been varied between 0 (i.e. a MAM layer backed by a single wall) and 1 (i.e. a symmetric arrangement), while keeping the total surface mass density of the system constant by setting $m''_{\mathrm{I}} + m''_{\mathrm{V}} = 100 m''_{\mathrm{m}}$. The resulting TL curves are shown in Fig. 3.10(a). The results show that, as the wall mass ratio decreases, the high TL region with 18 dB per octave shifts to higher frequencies. This is consistent with the behavior of the mass-air-mass resonance frequency of a conventional double wall: For constant total mass and wall spacing, the lowest mass-air-mass resonance frequency is achieved for a mass ratio of unity [83].

The MAM anti-resonance peak in Fig. 3.10(a) becomes slightly broader when the wall mass ratio is considerably smaller than unity. This is also reflected in Fig. 3.10(b), where the (anti-)resonance frequencies and the first peak bandwidth are shown for $m''_{\mathrm{I}}/m''_{\mathrm{V}} = 0 \ldots 1$. The third resonance frequency, which in Fig. 3.9(b) remained close to Ω_{P1} except for very small wall masses, diverges to infinity as m''_{I} approaches zero. Ω_2, on the other hand, is only weakly depending on $m''_{\mathrm{I}}/m''_{\mathrm{V}}$ and moves

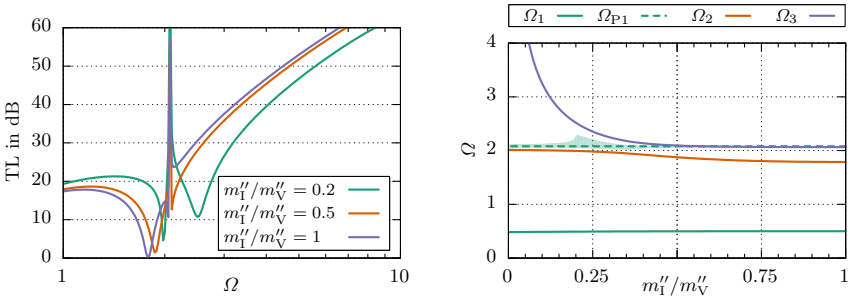

(a) Transmission loss. **(b)** Resonance and peak frequencies.

Figure 3.10: Parameter variation of the wall surface mass density ratio $m''_\mathrm{I}/m''_\mathrm{V}$ with constant total wall surface mass density $m''_\mathrm{I} + m''_\mathrm{V} = 100 m''_\mathrm{m}$.

closer to the anti-resonance frequency as the wall mass distribution becomes more and more asymmetric. Therefore, in this particular case there is a certain point at $m''_\mathrm{I}/m''_\mathrm{V} \approx 0.2$ where the anti-resonance bandwidth is maximal. For even lower values of $m''_\mathrm{I}/m''_\mathrm{V}$, the anti-resonance is diminished again by the approaching second resonance frequency. Ω_1, finally, does not depend on the wall mass ratio, because this resonance is characterized by a rigid body-type mode shape (see Fig. 3.8).

Air gap thicknesses: Fig. 3.11 shows the analytical results for a variation of the air gap thickness d_II, while requiring $d_\mathrm{IV} = d_\mathrm{II}$ and keeping the wall surface mass densities constant. The effect of the air gap thicknesses on the sound transmission loss as shown in Fig. 3.11(a) is similar to what is known from a conventional double wall: For larger air spacings, the mass-air-mass resonance frequency (here: Ω_2) is lowered and the 18 dB per octave region extends to lower frequencies. The bandwidth of the MAM anti-resonance remains very small, independently of the selected air gap thickness. A similar result has been observed

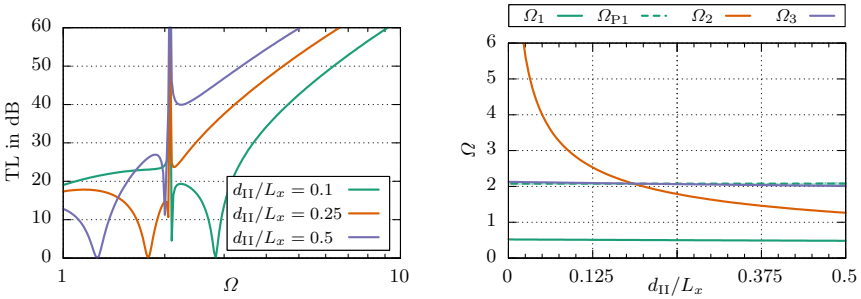

(a) Transmission loss. **(b)** Resonance and peak frequencies.

Figure 3.11: Parameter variation of the air gap thickness d_{II} with $d_{\mathrm{IV}} = d_{\mathrm{II}}$.

in Fig. 3.9(a) for the wall surface mass density variation: The overall double wall-like behavior of the structure can be improved by choosing large spacings between the layers, but the MAM anti-resonance bandwidth remains small in this symmetric design.

This observation can be confirmed in Fig. 3.11(b), where the (anti-) resonance frequencies and peak bandwidth of the multi-layered system are shown for d_{II}/L_x ranging from 0 (which rather is an academical value) to 0.5. As expected from the mode shapes shown in Fig. 3.8, the first resonance frequency Ω_1 does not depend on the thickness of the air gaps. Ω_2, on the other hand, exhibits the same variation as in Fig. 3.9(b), because in the symmetrical setup Ω_2 corresponds to the mass-air-mass resonance frequency of the two walls. According to Eq. (1.5), this frequency is proportional to $1/\sqrt{d_{\mathrm{II}} + d_{\mathrm{IV}}} = 1/\sqrt{2d_{\mathrm{II}}}$ and therefore diverges as $d_{\mathrm{II}} \to 0$. Finally, the third resonance frequency Ω_3 in Fig. 3.11(b) shows very little dependence on the thickness of the air gaps. Since in the basic design this resonance frequency is already very close to the anti-resonance frequency of the MAM, this explains the diminished peak bandwidth for every air gap thickness investigated in

Fig. 3.11(a). Therefore, it can be deduced that it should be avoided to place the MAM layer in the midplane between two walls with equal surface mass densities.

Air gap thickness ratio: The above studies have shown that the placement of the MAM layer in the midplane between the two outer walls is not advantageous for the bandwidth of the anti-resonance peak. Hence, it is now investigated how the placement of the MAM layer between the two walls affects the peak bandwidth. In Fig. 3.12, the analytical results are shown for a variation of the air gap ratio $d_{\mathrm{II}}/d_{\mathrm{IV}}$ while keeping the total spacing between the outer walls constant at $d_{\mathrm{II}} + d_{\mathrm{IV}} = 0.5L_x$. A small value of $d_{\mathrm{II}}/d_{\mathrm{IV}}$ corresponds to the MAM layer being placed very close to the first wall, while $d_{\mathrm{II}}/d_{\mathrm{IV}} = 1$ yields a symmetric layer structure. The transmission loss results in Fig. 3.12(a) show that the air gap thickness ratio does not affect the very low-frequency and high-frequency double wall-like characteristic of the system. This is consistent with the fact that the principal double wall parameters (i.e. the

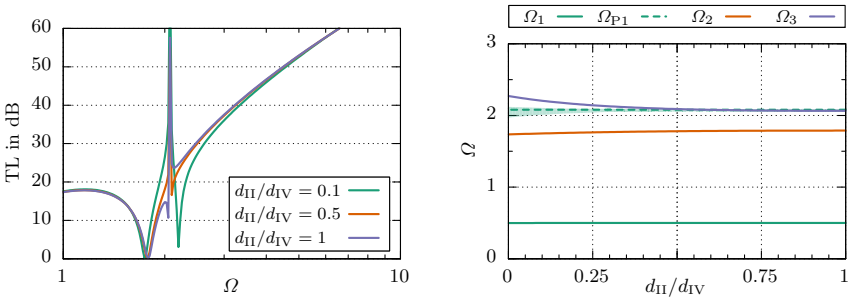

(a) Transmission loss. **(b)** Resonance and peak frequencies.

Figure 3.12: Parameter variation of the air gap thickness ratio $d_{\mathrm{II}}/d_{\mathrm{IV}}$ with constant total wall spacing $d_{\mathrm{II}} + d_{\mathrm{IV}} = 0.5L_x$.

wall surface mass densities and the wall spacing) are unchanged and only the interior layering structure is modified. However, as the MAM layer is moved closer to the first wall, the third resonance frequency moves away from the MAM anti-resonance. Consequently, the bandwidth of the peak is increased for small values of $d_{\mathrm{II}}/d_{\mathrm{IV}}$.

This can also be seen in Fig. 3.12(b), where the (anti-)resonance frequency shifting is shown for $d_{\mathrm{II}}/d_{\mathrm{IV}}$ varying from 0 (which, again, is only a theoretically possible value) to 1. As already mentioned, the first mode associated with Ω_1 is not depending on the properties of the air gaps and therefore Ω_1 remains constant in Fig. 3.12(b). For Ω_2, the air gap ratio almost has no influence, except for very low values of the air gap thickness ratio, which, however, are not relevant in practice. This nearly constant behavior can be explained by Ω_2 approximately corresponding to the mass-air-mass resonance of the two outer walls. This resonance is mainly affected by the total spacing between the walls, which is kept constant, and not by the placement of the MAM layer in between. The third resonance frequency Ω_3 exhibits the strongest dependence on the air gap thickness ratio $d_{\mathrm{II}}/d_{\mathrm{IV}}$ with Ω_3 increasing as $d_{\mathrm{II}}/d_{\mathrm{IV}}$ becomes lower. Consequently, the spacing between the resonance frequencies and the MAM anti-resonance frequency is the largest for the most asymmetric MAM layer placement close to one of the walls. Therefore, as shown in Fig. 3.12(a), the peak bandwidth is greatly improved in the present design for a strongly asymmetric arrangement of the layers.

Simultaneous parameter variation: The previous parameter studies were performed by varying a single parameter while keeping all others constant. Since for both the wall mass as well as the air gap parameter variations two different individual parameters have been varied, it is useful to perform a simultaneous parameter variation of each of these parameter pairs in order to find optimal combinations for obtain-

ing a large TL peak bandwidth. For this purpose, Figs. 3.13(a) and 3.13(b) show two heat maps of the relative bandwidth of the MAM anti-resonance for a simultaneous variation of the wall surface mass densities and the air gap thicknesses, respectively. The relative peak bandwidth is defined as the ratio of the absolute bandwidth of the peak divided by the center frequency of the band.

In Fig. 3.13(a), the relative peak bandwidth is shown for a simultaneous variation of the normalized first wall surface mass density $m''_{\mathrm{I}}/m''_{\mathrm{m}}$ and the wall surface mass density ratio $m''_{\mathrm{V}}/m''_{\mathrm{I}}$ of the two walls. These results confirm that in general it is not advantageous for the peak bandwidth to have a symmetric or nearly symmetric distribution of the wall surface mass densities. It can be seen that for a given value of m''_{I} there is a certain optimum value of $m''_{\mathrm{V}}/m''_{\mathrm{I}}$. For very large values of m''_{I}, the relative bandwidth reaches a maximum value of up to 14 %, as indicated by the red cross in Fig. 3.13(a). This particular behavior of the bandwidth maximum with respect to the wall surface mass densities is

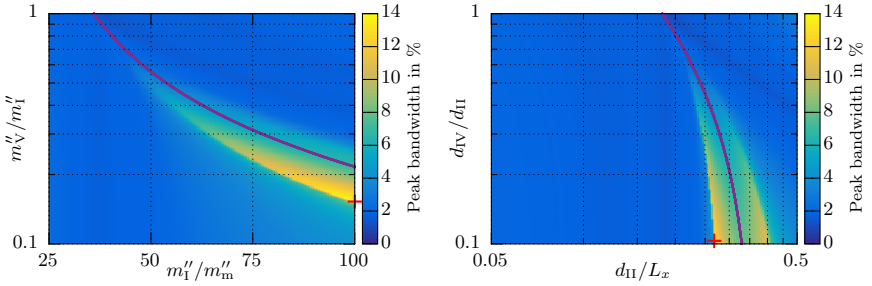

(a) Wall mass parameters. **(b)** Air gap parameters.

Figure 3.13: Relative anti-resonance peak bandwidth for different wall mass and air gap parameters. Red crosses indicate the maximum bandwidth configurations and the purple curves correspond to configurations with equal double wall mass-air-mass frequency and MAM anti-resonance frequency Ω_{P1}.

a result of the mass-air-mass resonance of the reference double wall design being close to the MAM anti-resonance frequency Ω_{P1}. The purple curve in Fig. 3.13(a) indicates the combinations of the two parameters $m''_{\mathrm{I}}/m''_{\mathrm{m}}$ and $m''_{\mathrm{V}}/m''_{\mathrm{I}}$ for which the mass-air-mass resonance frequency of the reference double wall design coincides with Ω_{P1}. It can be seen that the high bandwidth region in Fig. 3.13(a) is close to this curve. This indicates that it is advantageous for the given structure to place the mass-air-mass resonance frequency of the empty double wall close to the MAM anti-resonance frequency.

The relative peak bandwidth for a simultaneous variation of the air gap parameters is shown in Fig. 3.13(b). This diagram shows that it is also beneficial for the peak bandwidth to have an asymmetric placement of the MAM layer between the walls, as indicated by the optimum point being at $d_{\mathrm{IV}}/d_{\mathrm{II}} \approx 0.1$, which corresponds to the MAM layer being positioned close to the back wall. In this case, there is a certain range of values for d_{II} in Fig. 3.13(b) where the peak bandwidth is considerably larger with maximum values of up to 14 %. This can again be explained by the proximity between the mass-air-mass resonance frequency of the reference double wall and Ω_{P1}.

Air cavity absorption: Sound absorbing materials are commonly used within double walls to reduce the transmission loss dips at the resonance frequencies of the double wall system. As shown in the parameter studies above, the resonance frequencies of multi-layered systems with MAMs can diminish the transmission loss performance at the MAM anti-resonances. Hence, they should be spread out as much as possible by using a suitable layering structure. Additionally, the negative impact of the panel resonances could be reduced by introducing some absorption into the multi-layered system.

For simplicity, the effect of added sound absorption within the air cavities is investigated by introducing a frequency independent attenua-

tion coefficient Γ_0 and the complex acoustic wave number $k_0 \to k_0 - \mathrm{i}\Gamma_0$. In Fig. 3.14, the normalized air cavity attenuation coefficient $\Gamma_0 L_x$ has been varied between 0 (i.e. no absorption) and 0.1. The selected transmission loss curves in Fig. 3.14(a) indicate that the absorption leads to greatly improved TL values around the panel resonances. The positive effect of the sound absorbing cavities is particularly obvious at the second eigenfrequency, which, in the symmetric case, corresponds to the mass-air-mass resonance of the panel where the cavities undergo considerable oscillations. The MAM anti-resonance TL peak value, on the other hand, is not reduced by the sound absorption within the air gaps. This is different to the effect of damping within the membrane material, as observed in Fig. 2.18(a). As shown in Fig. 3.14(b), the (anti-)resonance frequencies of the panel are not affected by the attenuation coefficient Γ_0. Also, the bandwidth of the MAM anti-resonance remains very small even at the highest value of Γ_0. Nevertheless, as much sound absorbing materials as possible should be used within multi-layered panels containing MAMs to reduce the transmission loss reductions at the panel resonances. Selecting suitable absorbers in practical appli-

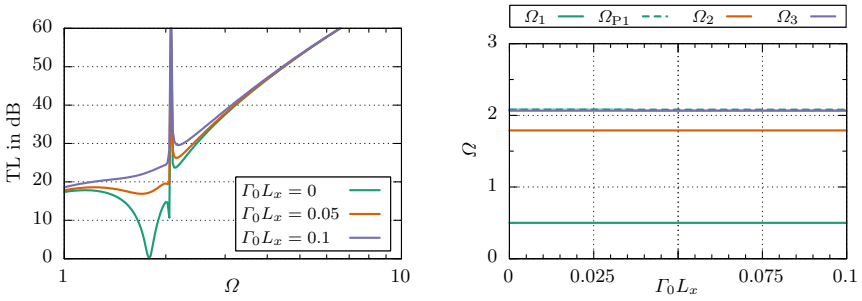

(a) Transmission loss. **(b)** Resonance and peak frequencies.

Figure 3.14: Parameter variation of the air cavity attenuation coefficient Γ_0.

cations, however, can be difficult. Hence, achieving a significant sound absorption performance at the low-frequencies where the anti-resonance frequencies of MAMs typically occur remains a certain challenge.

4. Noise shield demonstrator

In this chapter, the analytical models and the knowledge acquired in the previous chapters are used to design a noise shield demonstrator with membrane-type acoustic metamaterials for the experimental evaluation in a full-scale test environment. The tests were conducted on an acoustic fuselage demonstrator, which is described briefly in the first section of this chapter. The main objective of the noise shield demonstrator is to validate that MAMs are able to reduce efficiently (i.e. better than the corresponding mass-law) the transmission of sound with dominant tonal components around 100 Hz. An in-depth description of the noise shield design is provided in Section 4.2. Finally, the last section of this chapter covers the measurement procedure, the experimental results, and a discussion of these results.

4.1. Description of the acoustic fuselage demonstrator

The acoustic fuselage demonstrator is a vibro-acoustic test bench for the validation of numerical modeling techniques and innovative noise control treatments in the low- to mid-frequency regime [97]. As shown in Fig. 4.1(a), the test bench is located inside a large hemi-anechoic chamber and consists of a full-scale cylindrical aluminum fuselage segment with overall dimensions and design characteristics similar to a modern single-aisle airplane. The structural design of the fuselage, however, is considerably simplified compared to a real aircraft in order to

(a) Overview. **(b)** Loudspeaker array system.

Figure 4.1: Photographs of the acoustic fuselage demonstrator.

enhance the comparability between the test bench and results from numerical models. For example, the fuselage does not contain cut-outs for the cabin windows. The general dimensions and features of the test bench fuselage are summarized in Table 4.1. The fuselage rests on adjustable gas springs to approximate free-free boundary conditions and minimize the transmission of ground vibrations into the fuselage structure.

A moveable loudspeaker array system with 132 individually controllable loudspeakers is used for the acoustic excitation of the fuselage. Fig. 4.1(b) shows a close-up of the loudspeakers and the fuselage. This

Table 4.1: Summary of the general dimensions and features of the acoustic fuselage demonstrator test bench.

Fuselage		Loudspeaker Array	
Diameter:	4 m	Number of speakers:	12×11
Length:	8.5 m	Speaker spacing:	160 mm
		Array size:	1.92×1.76 m^2

system is capable of applying arbitrary acoustic pressure fields onto the fuselage surface up to 400 Hz to simulate, for example, the in-flight near-field noise of a CROR propulsion system [87, 97]. Further details on the loudspeaker array specifications are given in Table 4.1. It is possible to measure the acoustic pressure field on the fuselage using a microphone array which can be traversed along the circumference of the fuselage. As can be seen in Fig. 4.1(b), the loudspeaker array itself runs on a trolley that can be moved 360° around the demonstrator and in axial direction. Thus, the excitation system can reach most areas of the fuselage. Additionally, the individual loudspeakers can be tilted and adjusted in radial direction in order to account for the fuselage curvature.

The interior of the fuselage demonstrator is subdivided into two floors, a cabin and a cargo area below the cabin floor. At both ends of the fuselage, the interior cavity is anechoically terminated using sound absorbing end caps. Thus, standing sound waves in the axial direction are minimized to approximate the environment inside the much longer cabins of real aircraft.

4.2. Design of the noise shield demonstrator

As previously shown in Fig. 1.1, the principal conception of the aircraft noise shield is to attach suitable acoustic treatments to the *outer* surface of the fuselage. This means that the noise shield structure is exposed to the harsh environmental conditions that occur on the outside of an aircraft, e.g. the low temperatures during cruise flight or precipitation. Since most advanced acoustic treatments, in particular the membrane-type acoustic metamaterials considered here, can be easily damaged under such adverse conditions, an additional outer layer is required in order to protect the acoustic treatment from the environment. As illustrated in Fig. 4.2, this effectively leads to a particular layering

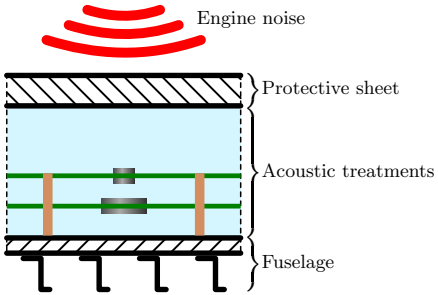

Figure 4.2: Basic structure of the aircraft noise shield demonstrator.

structure of the noise shield, where the acoustic treatment (i.e. one or more MAM layers) is located inside the air gap of a double wall-like partition. The two walls correspond to the stiffened skin panels of the fuselage (i.e. the interior wall) and the protective sheet (i.e. the outer wall), the latter being directly exposed to the environment.

Consequently, the noise shield demonstrator is assembled from two different parts: First, a cover sheet which is described in Section 4.2.1. Secondly, the MAM layers which are designed to fit between the protective sheet and the fuselage. The particular design of the MAM elements as well as the selection of suitable MAM parameters (e.g. membrane and mass properties, number of layers) are described in Section 4.2.2. The final subsection covers the assembly of these two parts and the final noise shield demonstrator design which is mounted onto the fuselage demonstrator.

4.2.1. Cover sheet design

An orthogonally stiffened aluminum panel with a curvature adjusted to that of the fuselage is used as the cover sheet of the noise shield demonstrator. As shown in Fig. 4.3(a), the cover sheet has 5 frames,

11 stringer rows, a length of 2.7 m, and a width of 2.7 m. The total dimensions of the noise shield are chosen so that its surface area is larger than that of the loudspeaker array. This ensures that the direct sound field from the loudspeakers only excites the noise shield surface. The skin thickness is 1.5 mm, the frames are curved T-shaped beams, and the stringers are Z-profiles. The skin is fixed to the stiffeners using M4 screws. Fig. 4.3(b) shows a photograph of the stiffening structure of the cover sheet and geometrical data for the stiffener cross sections. Overall, the mass of the cover sheet is given by $M_{\text{cover}} = 70$ kg. Taking into account the curvature of the panel, the surface area covered by the noise shield is $S_{\text{shield}} = 2.7 \times 3\ \text{m}^2 = 8.1\ \text{m}^2$ and the corresponding surface mass density of the cover sheet is $m''_{\text{cover}} = 8.6\ \text{kg/m}^2$.

It should be mentioned that the cover sheet of the noise shield demonstrator is rather heavy and bulky compared to what one would expect to be attached to a real aircraft. This is because the main driver for the cover sheet design is the flexibility to investigate the noise shield

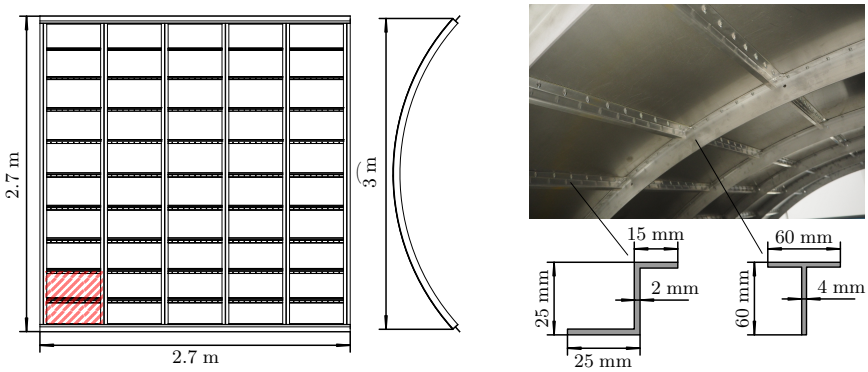

(a) Cover sheet dimensions. The red shaded region indicates a bay for one MAM element.

(b) Photograph and geometry of the stiffeners.

Figure 4.3: The cover sheet of the aircraft noise shield demonstrator.

demonstrator in laboratory environments other than the acoustic fuselage demonstrator test bench. Also, it should be possible to integrate other innovative acoustic treatments into the noise shield. Another important requirement is the manufacturing of the noise shield, which is based on the same tools and principles used in the manufacturing of the fuselage to minimize the manufacturing costs for the noise shield demonstrator.

4.2.2. MAM layer design

The acoustic treatment of the noise shield demonstrator is to be integrated into the underside of the stiffened cover sheet. Therefore, it is reasonable to exploit the particular structure of the panel for the design and integration of the MAM layers. In Fig. 4.3(a) it can be seen that the frames and stringers subdivide the cover sheet underside into rectangular bays. Skipping every second stringer row and using the frames as lateral boundaries, as indicated by the red shaded rectangle in Fig. 4.3(a), the cover sheet is sectioned into 5×5 bays. In each of these bays a so-called MAM element containing multiple unit cells and layers of MAMs is fastened to the frame webs of the cover sheet. 25 of these MAM elements tiled along the cover sheet in this manner make up the acoustic treatment of the noise shield demonstrator.

The resulting length and width of the MAM elements are 430 mm and 490 mm, respectively. An aluminum lattice is used to hold the MAM layers. As shown in Fig. 4.4, the lattice consists of 20 mm $\times$ 20 mm U-beams welded together and subdividing the MAM element into 3×3 MAM unit cells. Attachment lugs are welded to the sides of the grid so that the MAM element can be attached to the frames of the cover sheet. The edge lengths of the unit cells are given by $L_x = 137$ mm and $L_y = 117$ mm, respectively. Thus, the aspect ratio of the MAM unit cells is $\Lambda \approx 1.17$. The mass of a lattice element is

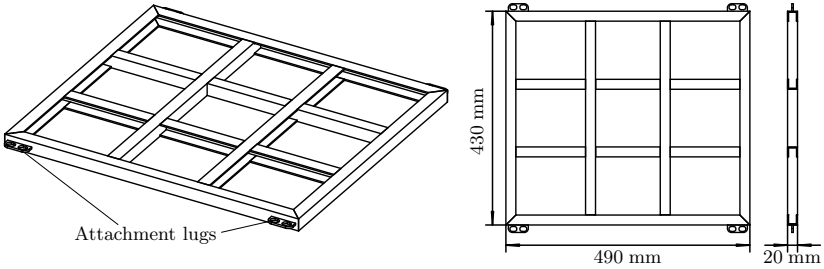

Figure 4.4: MAM element grid for supporting the two MAM layers inside the noise shield demonstrator.

given by $M_{\mathrm{G}} = 1$ kg. This particular design for the MAM element grid is a compromise between the required sub-wavelength size of the MAM unit cells and the grid mass, which – for fixed beam properties – linearly scales with the number of unit cells. Additionally, these MAM elements are sized so that they can also be integrated into the side wall of the fuselage. This enables further investigations of MAMs as cabin lining elements for other sound reduction concepts.

The same *Orastick* membrane material as in the experimental MAM unit cell investigations (see Sections 2.4 and 3.3) is used for the MAM elements of the noise shield demonstrator. The manufacturing procedure of the MAM elements is similar to the unit cell test samples, so that the same membrane prestress resultant of $T_{\mathrm{m}} = 200$ N/m can be assumed. With these membrane properties, the nondimensional bending stiffness for the noise shield MAMs is given by $\Xi = 1.5 \times 10^{-6}$ and can be regarded as negligible. For ambient air conditions with $\rho_0 = 1.18$ kg/m^3 and $c_0 = 343$ m/s, the nondimensional speed of sound and characteristic impedance become $\varsigma_0 = 7.4$ and $\mathcal{Z}_0 = 12.9$, respectively. Compared to the other MAM configurations, which are summarized in Table 2.1, ς_0 is identical to the values for the impedance tube samples,

because this quantity depends only on the membrane and fluid material properties. The nondimensional characteristic impedance, however, is considerably larger for the noise shield MAMs, since $\mathcal{Z}_0$ is proportional to the MAM unit cell edge length, which is nearly three times larger than in the impedance tube measurements. Hence, from the parameter study results shown in Fig. 2.24 it must be expected that the TL-peak bandwidth is strongly reduced for the larger MAM unit cells. It follows that a suitable added mass configuration has to be found so that the noise reduction performance of the MAMs is notable in the measurements.

The parameter studies in Section 2.5 have identified which nondimensional MAM mass parameters are appropriate for tuning the MAM anti-resonance bandwidth. The eccentricity of a single mass as well as the mass radius of gyration have been shown to be inapplicable for the bandwidth control. Thus, the remaining tuning parameters of the noise shield MAMs are the nondimensional mass magnitude μ and the nondimensional mass diameter δ_{M}. According to the parameter study results in Section 2.5, these two parameters are used to control the MAM anti-resonance in the following way: First, the mass diameter δ_{M} should be large in order to obtain a high anti-resonance bandwidth. Secondly, since a higher δ_{M} shifts the anti-resonance to higher frequencies, the mass μ must be increased accordingly. This, however, adds to the total mass of the MAM layers.

A parameter variation of these two mass parameters for the given MAM configurations revealed that it is difficult to find a suitable combination of δ_{M} and μ, when only one mass per unit cell is used. The chosen parameter combination has to ensure large anti-resonance bandwidths at the desired frequencies and result in a mass geometry that is readily available on the market (due to the high number of masses required for assembly). However, this can be resolved by using two masses per unit cell with smaller diameters instead of one large mass.

Fig. 4.5(a) compares the analytically obtained transmission loss of a MAM element unit cell with one or two masses attached. In case of the single mass configuration, a cylindrical steel mass with $D_{\mathrm{M}} = 50$ mm and $M = 11.6$ g is attached to the center of the unit cell. The double mass configuration is illustrated in Fig. 4.5(b), where two masses with each $D_{\mathrm{M}} = 30$ mm and $M = 5.8$ g are placed along the y-symmetry axis with a spacing of $L_x/3$. The resulting static surface mass densities of both MAM configurations are equal with $m''_{\mathrm{st}} = 820$ g/m^2. The analytical results in Fig. 4.5(a) show that the transmission loss of both configurations is nearly identical with a clear anti-resonance at $f_{\mathrm{P1}} = 100$ Hz. In both cases, the anti-resonance bandwidth is equally good, except for an additional resonance and anti-resonance below 150 Hz for the double mass configuration, which occurs due to the additional mass. Since the MAM unit cell configuration with two masses yields smaller masses with larger thicknesses that are readily available on the market, this design is preferred over a single mass unit cell configuration for the MAM elements.

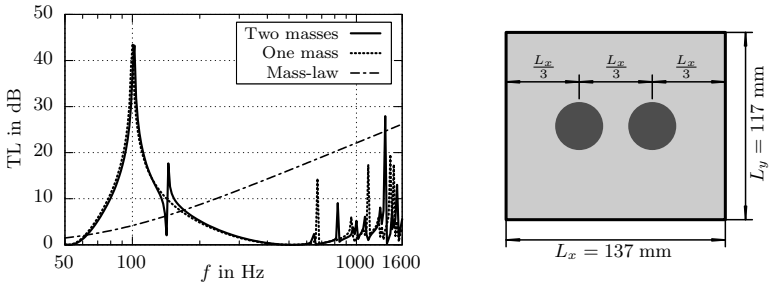

(a) Transmission loss. **(b)** Unit cell with two masses.

Figure 4.5: Sound transmission loss of a MAM element unit cell carrying one or two masses with the same total mass.

As shown in Fig. 4.5(a), the choice of two cylindrical steel masses with $D_\mathrm{M} = 30$ mm and $M = 5.8$ g yields an anti-resonance at $f_\mathrm{P1} = 100$ Hz with a +10 dB-bandwidth (compared to the mass-law) of 36 Hz. Therefore, this design is chosen for the MAM unit cells on the first side of the MAM elements. In order to achieve an anti-resonance at a slightly higher frequency, smaller steel masses with $D_\mathrm{M} = 20$ mm and $M = 2.6$ g are selected for the other side of the MAM elements. This results in an anti-resonance at $f_\mathrm{P1} = 120$ Hz and a slightly smaller bandwidth of 32 Hz. Table 4.2 summarizes the resulting nondimensional parameters for these two MAM configurations, with NS1 and NS2 corresponding to the MAMs with Ø30 mm-masses and Ø20 mm-masses, respectively. With the given air gap between the two MAM layers as prescribed by the height of the MAM element grids (20 mm, see Fig. 4.4), the transfer matrix model is employed to estimate the normal incidence sound transmission loss of these MAM elements. The results are shown in Fig. 4.6(a). For comparison, Fig. 4.6(a) also shows the calculated sound transmission loss curves for the two individual MAM layers NS1 and NS2 (orange and purple dashed curves, respectively), as given in Table 4.2, as well as the corresponding mass-law curves (dash-dotted lines) with taking into account the mass of the grid ($m''_\mathrm{st} = 5.6$ kg/m^2) and without the grid ($m''_\mathrm{st} = 0.9$ kg/m^2). The

Table 4.2: Nondimensional parameters of the two MAM layers on each side of the noise shield MAM elements with two cylindrical masses per unit cell, as shown in Fig. 4.5(b).

	Membrane			Cylindrical mass (×2)					Fluid	
Conf.	Λ	Ξ	η_m	δ_M	μ	ϑ	ξ^*	η^*	$\mathcal{Z}_0$	ς_0
NS1	1.17	1.5×10^{-6}	10^{-3}	0.22	3.4	3×10^{-3}	$\frac{1}{3}$; $\frac{2}{3}$	0.5	12.9	7.4
NS2	1.17	1.5×10^{-6}	10^{-3}	0.15	1.5	1.3×10^{-3}	$\frac{1}{3}$; $\frac{2}{3}$	0.5	12.9	7.4

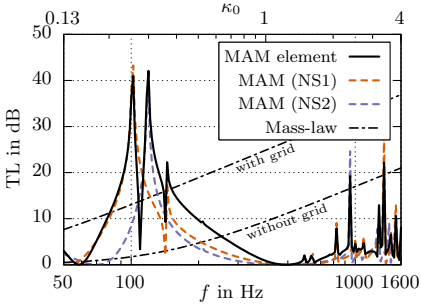

(a) Estimated transmission loss.

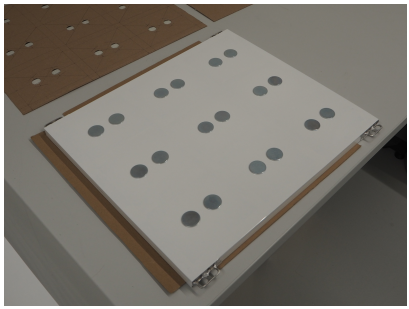

(b) Photograph of a MAM element.

Figure 4.6: Analytically estimated normal incidence sound transmission loss of the MAM elements for the noise shield.

analytical results for the MAM element in Fig. 4.6(a) exhibit the well-known characteristics of stacked membrane-type acoustic metamaterials [66]. The anti-resonances of each MAM layer are retained in this arrangement and an additional resonance occurs between the two major anti-resonances. As indicated in the top axis of Fig. 4.6(a), the nondimensional wave number κ_0 is well below unity at the two anti-resonances so that the effective surface mass density approximation is valid in this frequency range. The combined bandwidth of the MAM element anti-resonances is determined to be 55 Hz, if the grid mass is not considered, and 11 Hz, if $m''_{\mathrm{st}} = 5.6\,\mathrm{kg/m^2}$ is chosen as the reference mass for the bandwidth calculation. This indicates that the grid mass has a strong influence on the resulting bandwidth of the MAM elements. Therefore, the support grids for MAMs should be as lightweight as possible to minimize the amount of acoustical deadweight introduced into the structure.

Based upon these analytical predictions, the selected mass configurations for the two layers of the MAM elements can be considered

as sufficient for meeting the requirements of the noise shield demonstrator. Therefore, all 25 MAM elements are manufactured according to this specification. Fig. 4.6(b) shows a photograph of an assembled MAM element with the nine unit cells containing the Ø30 mm-masses facing upwards.

4.2.3. Noise shield assembly

The inner layering structure of the noise shield assembly on top of the fuselage structure is shown in Fig. 4.7. The final assembly consists of nine different layers, denoted by I to IX in Fig. 4.7. The first layer corresponds to the stiffened cover sheet with surface mass density $m''_{\mathrm{I}} = m''_{\mathrm{cover}} = 8.6\ \mathrm{kg/m^2}$. On the inside of the cover sheet, a $d_{\mathrm{II}} = 25$ mm thick melamine foam layer (*Basotect*) is attached in order to provide some absorption inside the noise shield interior cavity and reduce the negative impact of cavity resonances on the sound transmission through the noise shield. Layer III is an air gap separating the melamine foam layer from the upper side of the MAM elements. Due to the curvature of the noise shield, the thickness of the air gap d_{III} varied approximately

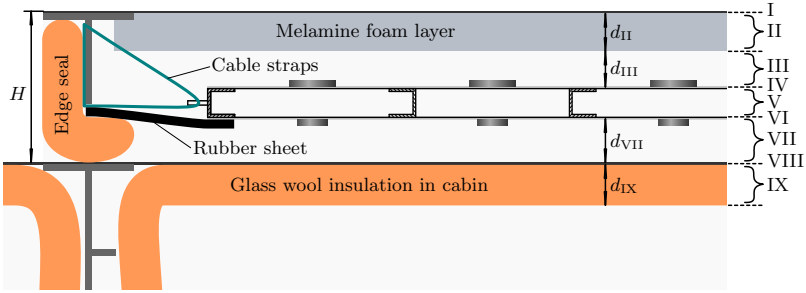

Figure 4.7: Layering structure of the noise shield assembly on top of the fuselage structure.

between 20 and 35 mm along the circumferential direction. Layer IV corresponds to the first of the two MAM layers attached to the MAM element grids. This MAM layer has the two Ø30 mm-masses per unit cell attached to the membrane and its nondimensional properties are denoted as configuration NS1 in Table 4.2. In terms of the surface area covered by the noise shield, this layer introduces a surface mass density of $m''_{\mathrm{MAM1}} = 0.38\ \mathrm{kg/m^2}$ into the structure. The next layer is the air gap which is enclosed by the two MAM layers and the MAM element grid. As shown in Fig. 4.4, the MAM layer spacing is prescribed by the grid as $d_{\mathrm{V}} = 20$ mm and the MAM element grids itself have a surface mass density of $m''_{\mathrm{G}} = 25 \cdot M_{\mathrm{G}}/S_{\mathrm{shield}} = 3\ \mathrm{kg/m^2}$. The MAM layer on the other side of the grid is denoted as layer VI in Fig. 4.7. This MAM layer carries two Ø20 mm-masses per unit cell and the nondimensional properties are given under configuration NS2 in Table 4.2. The resulting surface mass density for this layer is $m''_{\mathrm{MAM2}} = 0.2\ \mathrm{kg/m^2}$.

As shown in Fig. 4.7, each MAM element is fixed to the cover sheet frames using cable straps through the attachment lugs (see Fig. 4.4) and holes inside the frames. Fig. 4.8(a) shows a photograph of the MAM element attachment with the cable straps. This way it is possible to keep the MAM elements in place inside the noise shield without introducing too many structure-borne sound bridges, which could compromise the high airborne sound insulation at the anti-resonances of the MAMs. Furthermore, Fig. 4.8(a) shows large gaps of roughly 100 mm width between adjacent MAM elements due to their reduced size. In total, the MAM elements covered only about 67 % of the noise shield surface area. The remaining 33 % of the surface have to be sealed properly so that sound waves cannot bypass the MAMs through those gaps. As indicated in Fig. 4.7, 6 mm thick rubber sheets ($\rho_{\mathrm{rubber}} = 1500\ \mathrm{kg/m^3}$) are glued onto the edges of the MAM elements in order to cover up the gaps. Fig. 4.8(b) shows a photograph of the interior of the fully assembled noise shield with sealed gaps. With respect to the full surface area

(a) MAM element attachment. **(b)** Full assembly.

Figure 4.8: Photographs of the noise shield assembly.

of the noise shield, these rubber strips add $m''_{\text{rubber}} \approx 2.8\ \text{kg/m}^2$ to the surface mass density of the noise shield. Finally, the last layer within the noise shield is layer VII which, as illustrated in Fig. 4.7, is the air gap between the MAM elements and the skin of the fuselage. The spacing d_{VII} is determined by the thickness of the other noise shield layers and the noise shield height $H = 100$ mm via $d_{\text{VII}} = H - (d_{\text{II}} + d_{\text{III}} + d_{\text{V}})$. In an effort to reduce the amount of sound transmitted through the small gap between the edges of the noise shield and the fuselage, a glass wool edge seal is applied to the circumference of the panel (see Fig. 4.7). Thus, when the noise shield is resting on the fuselage, the edge seal is supposed to provide an airtight sealing. Therefore, the interior of the noise shield is somewhat isolated from the exterior sound levels around the panel edges. The glass wool edge seal can also be seen in the photograph shown in Fig. 4.8(b).

The two remaining layers VIII and IX represent the fuselage structure. Layer VIII corresponds to the stiffened primary structure with a surface mass density of $m''_{\text{VIII}} = m''_{\text{fsl}} = 10\ \text{kg/m}^2$. The interior surface of the fuselage is lined with glass wool insulation (layer IX) to provide some acoustic absorption inside the cabin. The thickness of the glass

wool layer is approximately $d_{\mathrm{IX}} = 50$ mm. Lining panels have not been installed into the cabin at the time of these measurements.

A tabular overview of the different layers and their relevant acoustic properties is given in Table 4.3. These values are used for transfer matrix calculations of this noise shield setup. Since the transfer matrix model does not account for the curvature of the fuselage structure, the air gap thickness d_{III} is set to 30 mm. This value corresponds to the average spacing between the MAM elements and the melamine foam layer along the circumference. The density ρ, porosity χ, and specific flow resistivity σ of the melamine foam layer and glass wool insulation have been taken from [90] and [51], respectively. These values are used in the transfer matrix calculations to obtain the equivalent densities and bulk moduli of the corresponding porous layers using the Champoux-Allard model [1], as described in Section 3.1.1.

The noise shield is attached to the fuselage at two points using hinge joints. One of these hinge joints can be seen in Fig. 4.8(b) at the upper edge of the panel near the upper right corner. Thus, the fully assem-

Table 4.3: Layer properties of the noise shield assembly shown in Fig. 4.7.

Layer:	Type:	Properties:
I	Wall	$m''_{\mathrm{I}} = 8.6$ kg/m^2
II	Porous layer	$d_{\mathrm{II}} = 25$ mm, $\rho_{\mathrm{II}} = 9.2$ kg/m^3, $\chi_{\mathrm{II}} = 0.99$, $\sigma_{\mathrm{II}} = 10$ kN s/m^4 [90]
III	Air gap	$d_{\mathrm{III}} = 30$ mm
IV	MAM	NS1 in Table 4.2 (Masses with Ø30 mm)
V	Air gap	$d_{\mathrm{V}} = 20$ mm
VI	MAM	NS2 in Table 4.2 (Masses with Ø20 mm)
VII	Air gap	$d_{\mathrm{VII}} = 25$ mm
VIII	Wall	$m''_{\mathrm{VIII}} = 10$ kg/m^2
IX	Porous layer	$d_{\mathrm{IX}} = 50$ mm, $\rho_{\mathrm{IX}} = 5.5$ kg/m^3, $\chi_{\mathrm{IX}} = 0.95$, $\sigma_{\mathrm{IX}} = 21$ kN s/m^4 [51]

bled noise shield panel can be folded around these hinges using ropes until the panel rests safely on top of the fuselage. Two spacers on the opposite edge to the hinges ensure the height of the noise shield to be approximately $H = 100$ mm. Fig. 4.9(a) shows a photograph of the noise shield resting on the fuselage after being fully folded up.

4.3. Noise shield measurements

4.3.1. Measurement procedure

When the noise shield panel is folded up, the loudspeaker array is positioned in front of the noise shield. Fig. 4.9(a) shows the final position of the loudspeakers, which was reproduced for every measured configuration of the noise shield. The distance between the loudspeaker membranes and the surface of the noise shield is adjusted to be approximately 0.26 m everywhere along the loudspeaker array surface. Several types of excitation signals are available to evaluate the sound

(a) Noise shield with loudspeaker array in position.

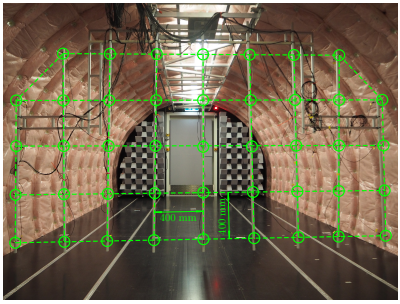

(b) Microphone array for mapping the sound level inside the cabin.

Figure 4.9: Photographs of the measurement setup with the excitation system in front of the noise shield and the microphone array inside the cabin.

transmission through the noise shield for different incident sound fields. A broadband pink noise signal (bandwidth $f = 60 \ldots 1000$ Hz) is used to characterize the noise shield over a wide range of frequencies. To emulate typical noise fields generated by CROR engines, multi-tonal noise fields with arbitrary trace wave numbers imprinted on the noise shield are employed.

The different sound fields on the surface of the noise shield, as generated by the loudspeaker array, are characterized using the moveable microphone array between the fuselage and the loudspeakers. The microphones allow the measurement of the sound pressure field at 240 points distributed on a rectangular grid across the surface covered by the loudspeaker array. Fig. 4.10 shows the measured sound pressure level and phase angle fields for the pink noise excitation at a representative frequency of $f = 100$ Hz. It can be seen that the sound pressure level distribution is nearly uniform with $L_P \approx 85$ dB, except for a considerable sound level reduction near the vertical center line of the loudspeaker array. The explanation for this particular inhomogeneity in

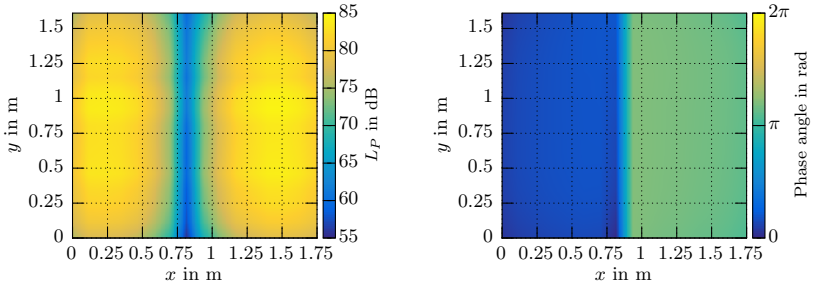

(a) Sound pressure level. **(b)** Phase angle.

Figure 4.10: Measured spatial distribution of the sound pressure level and phase angle at $f = 100$ Hz for the pink noise excitation.

the pink noise sound field can be found in the phase angle distribution shown in Fig. 4.10(b). The left and right halves of the loudspeaker array exhibit a phase difference of 180° which leads to cancellation effects at the vertical center line. This phase difference is caused by the internal circuitry of the two amplifiers driving each half of the loudspeaker array and could not be compensated for the pink noise fields at the time of the measurements. Therefore, when discussing measurement results obtained under pink noise excitation, this particular characteristic of the pink noise field needs to be accounted for.

An example for one of the multi-tonal noise fields at a frequency of $f = 100$ Hz is shown in Fig. 4.11. The imprinted trace wave propagates in x-direction (i.e. along the fuselage axis) with an axial wave number component of $k_x = 5.5$ rad/m, as can be seen in the phase angle distribution in Fig. 4.11(b). The sound pressure level is mostly uniform at $L_P \approx 88$ dB across the loudspeaker array (see Fig. 4.11(a)). Several wave numbers ranging from 2.5 rad/m (long wavelength) to 8.5 rad/m

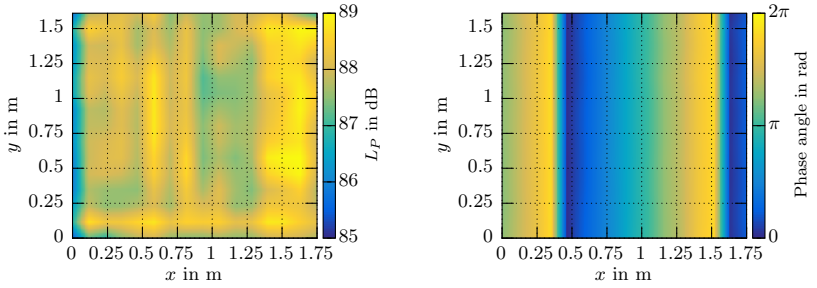

(a) Sound pressure level. **(b)** Phase angle.

Figure 4.11: Measured spatial distribution of the sound pressure level and phase angle at $f = 100$ Hz for the multi-tonal excitation with an imprinted trace wave number of $k_x = 5.5$ rad/m.

(small wavelength) as well as wave directions (axial k_x, circumferential k_y, and diagonal k_{xy}) are investigated. In case of these multi-tonal sound fields, the phase mismatch of the two amplifiers could be compensated.

Inside the cabin of the demonstrator fuselage, the resulting sound pressure field is measured using a microphone array carrying 43 1/2" diffuse field microphones in a grid-like pattern with a regular microphone spacing of 400 mm, as shown in Fig. 4.9(b). This array allows the simultaneous measurement of a whole cross-section through the cabin and can be traversed along the fuselage axis to capture the whole cavity. For every measurement, the array is moved to 15 stations with a uniform spacing of 533 mm along the fuselage axis (equal to the frame spacing), so that the total number of measurement points inside the cabin is 645. For the evaluation of the measurement results, this large number of data points is condensed to a single value per frequency by calculating the average sound pressure level (SPL) inside the cabin, defined as

$$\langle L_P \rangle_{\text{cabin}} = 10 \lg \left(\frac{1}{V_{\text{cabin}}} \iiint_{V_{\text{cabin}}} 10^{0.1 L_P} \, \mathrm{d}V_{\text{cabin}} \right), \tag{4.1}$$

where $V_{\text{cabin}} \approx 37 \text{ m}^3$ is the measurement volume inside the cabin and L_P is the sound pressure level. Since L_P is measured only at discrete points, the integral in Eq. (4.1) is calculated numerically using the trapezoidal rule. In order to obtain a measure for the noise shield transmission loss, the spatially averaged noise reduction $\langle \text{NR} \rangle$ is employed. This quantity is closely related to the TL of the noise shield and is defined as

$$\langle \text{NR} \rangle = \langle L_P \rangle_{\text{exc}} - \langle L_P \rangle_{\text{cabin}} , \tag{4.2}$$

where $\langle L_P \rangle_{\text{exc}}$ is the surface average of the excitation field sound pressure level [36]. $\langle L_P \rangle_{\text{exc}}$ is obtained from the measured spatial sound

pressure level distributions (as for example shown in Fig. 4.10(a)) using an integration procedure over the loudspeaker array surface, similar to Eq. (4.1) for the interior cavity.

In order to identify the acoustic performance of the MAM elements integrated inside the noise shield structure, a total of three different noise shield configurations and, as a reference, the bare fuselage structure without a noise shield are investigated. These configurations are listed in Table 4.4 with the estimated total surface mass density m''_{tot} of each configuration. Configuration A corresponds to the reference case where the cabin sound pressure levels without any noise shield structure are measured. A photograph of noise shield configuration B is shown in Fig. 4.12(a). This configuration represents a conventional double wall design, where the cover sheet of the noise shield is filled with glass wool packages. The resulting total surface mass density is nearly twice as large as that of the fuselage alone. Configuration C basically is the same as the fully assembled MAM noise shield (configuration D), however with the MAM elements removed (see Fig. 4.12(b)). The rubber strips are kept inside the noise shield for this configuration in order to act as dummy masses. Thus, by comparing configurations C and D, the influence of the MAMs on the sound transmission properties of the

Table 4.4: Descriptions and estimated total surface mass densities of the measured noise shield configurations.

Conf.:	Description:	m''_{tot} (kg/m^2)
A	No noise shield (fuselage only)	10.3
B	Cover sheet filled with glass wool (double wall)	19.7
C	Noise shield without MAM elements, but rubber strips as dummy masses	21.9
D	Noise shield with MAM elements and rubber strips	25.5

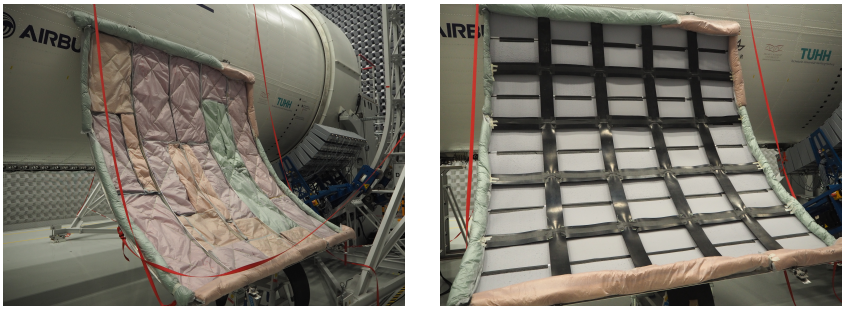

(a) Double wall configuration.

(b) Noise shield without MAM elements.

Figure 4.12: Photographs of the additionally measured noise shield configurations B and C, as listed in Table 4.4.

noise shield can be evaluated. The total surface mass density of configuration C is 11 % higher than that of the double wall (configuration B). With the MAM elements integrated, the surface mass density of the noise shield is 29 % larger.

4.3.2. Results for pink noise excitation

Fig. 4.13 shows the measurement results for the fuselage and the three noise shield configurations given in Table 4.4 under pink noise excitation. In Fig. 4.13(a), the average noise reductions for all noise shield configurations are displayed over a frequency range of 50 to 250 Hz. Fig. 4.13(b) shows the related noise reduction differences $\Delta\langle \mathrm{NR} \rangle = \langle \mathrm{NR} \rangle - \langle \mathrm{NR} \rangle_{\mathrm{ref}}$ of the noise shields, where the reference configuration corresponds to the bare fuselage (i.e. configuration A in Table 4.4). Thus, a positive NR difference indicates an improved fuselage sound transmission loss by the noise shield.

At low frequencies between 50 and 100 Hz, the noise reduction of the

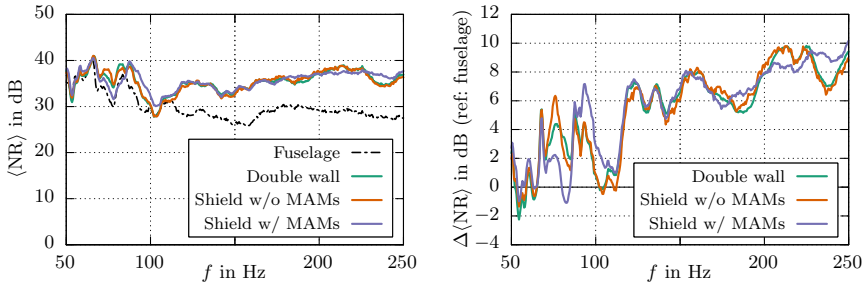

(a) Average noise reduction. **(b)** Average noise reduction difference.

Figure 4.13: Measured average noise reduction and noise reduction difference for the different noise shield configurations at pink noise excitation.

bare fuselage (dash-dotted curve in Fig. 4.13(a)) exhibits strong variations ranging from 30 to 40 dB. These variations can be attributed to the modal behavior of the fuselage structure. Above 100 Hz, the fuselage ⟨NR⟩ drops to a nearly constant value of around 29 dB, which is consistent with previous noise reduction measurements of similar fuselage structures [36]. At first, the noise reduction curves of the three noise shield configurations in Fig. 4.13(a) qualitatively follow the fuselage ⟨NR⟩ curve with slightly higher ⟨NR⟩ levels. But above approximately 105 Hz, the noise reduction of the noise shields becomes considerably higher than that of the fuselage. This indicates that above this frequency, the double wall effect becomes the predominant noise reduction mechanism for all three noise shield designs. It should be noted that, according to Eq. (1.5), the mass-air-mass resonance of the double wall noise shield would be predicted as $f_0 \approx 88$ Hz (assuming $\theta_\mathrm{i} = 0°$), which is 16 % lower than the 105 Hz observed in Fig. 4.13(a). This discrepancy can possibly be attributed to the curvature of the noise shield, which is not accounted for in Eq. (1.5), and the non-uniform pink noise

excitation field (see Fig. 4.10). Above the presumed mass-air-mass resonance at 105 Hz, the noise reduction improvement of the noise shields jumps to about 6 dB and continues to rise as the frequency increases. This observation is consistent with the noise reduction improvement of double walls over a single wall above the mass-air-mass resonance.

The different acoustic performances of the noise shield variants become more clearly visible in the noise reduction difference plots in Fig. 4.13(b). Here it can be seen that the $\langle \mathrm{NR} \rangle$ of the noise shield without MAMs (orange curve) is mostly very similar to that of the double wall (green curve). However, for some narrow frequency bands, considerable differences can be observed. For example, around 75 Hz the cabin noise reduction of the noise shield without MAMs is up to 2 dB larger than that of the double wall. Since the most notable difference between those two noise shield designs is the introduction of the rubber strips as dummy masses, this noise reduction improvement should be attributable to the dynamic behavior of the rubber strips. The $\Delta\langle \mathrm{NR} \rangle$ of the noise shield with MAMs (purple curve) deviates most notably from the noise shield without MAMs at low frequencies between 75 and 125 Hz. In order to emphasize these differences, Fig. 4.14(a) shows the measured noise reduction differences of the noise shield with and without MAMs as compared to the $\langle \mathrm{NR} \rangle$ of the double wall configuration. Between 75 and 85 Hz it can be seen that the noise reduction of the noise shield is significantly reduced by up to 3 dB when the MAM elements are integrated. As explained in Chapter 3, where multi-layered structures with MAMs were analyzed, the integration of MAM layers inside a double wall structure introduces additional panel resonances. These significantly reduce the sound transmission loss of the structure around these frequencies. Furthermore, the sound absorption of the melamine layers is expected to be very low at frequencies below 100 Hz so that the TL reduction at a panel resonance of the noise shield structure can become very pronounced, as observed in Fig. 4.14(a). This

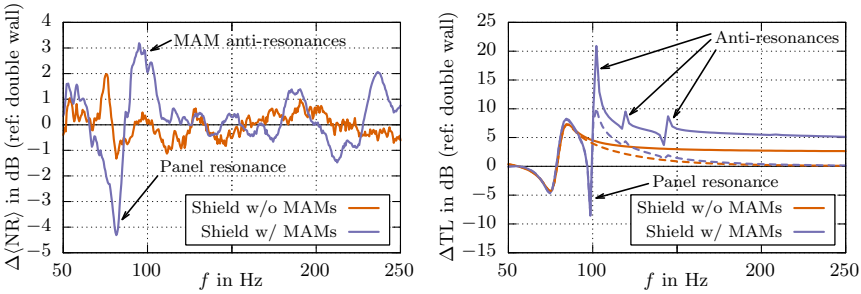

(a) Demonstrator measurements. **(b)** Transfer matrix model.

Figure 4.14: Measured noise reduction differences and analytically predicted transmission loss differences of the noise shield with and without MAMs compared to the double wall configuration. The dashed lines in (b) indicate the calculated $\Delta\langle \mathrm{NR} \rangle$ using Eq. (D.6) assuming a flanking incident sound power ratio of $W_{\mathrm{i,fsl}}/W_{\mathrm{i,shield}} = 0.1$.

indicates that in fact a panel resonance occurs within the MAM noise shield at around 82 Hz, which has been marked as such in Fig. 4.14(a). For frequencies between 85 and 125 Hz, on the other hand, the $\Delta\langle \mathrm{NR} \rangle$ of the MAM noise shield increases by up to 3 dB compared to the noise shield without MAMs. The frequency range of this noise reduction improvement lies slightly below the expected anti-resonance frequencies of the MAM elements (compare Fig. 4.6(a)). Since the MAM elements are not rigidly attached to the noise shield structure (unlike the fixed membrane edges assumed in the analytical MAM model), the compliant attachment of the MAM elements using cable straps shifts the anti-resonances of the MAMs to lower frequencies. Therefore, it is a reasonable assumption that the noise reduction improvement in this frequency range is in fact caused by the anti-resonances of the integrated MAM layers.

For comparison, Fig. 4.14(b) shows the normal incidence transmis-

sion loss difference $\Delta\mathrm{TL} = \mathrm{TL} - \mathrm{TL}_{\mathrm{ref}}$, calculated using the transfer matrix method with the layer properties given in Table 4.3. In order to account for the additional mass introduced by the rubber strips, $m''_{\mathrm{rubber}} \approx 2.8\ \mathrm{kg/m^2}$ is added to the cover sheet surface mass density m''_{I}. The analytical results clearly show the MAM anti-resonances with three peaks at the expected frequencies (compare Fig. 4.6(a)) and a pronounced panel resonance slightly below the first MAM anti-resonance frequency. Qualitatively, this is consistent with the observations in the measurement results given in Fig. 4.14(a). However, besides the already explained frequency shift in the measured MAM anti-resonances and panel resonance, the most notable difference between the analytical and the experimental results is the large difference between the maximum measured noise reduction improvements (3 dB) and the maximum predicted transmission loss improvements (up to 20 dB) at the MAM anti-resonances.

A very likely explanation for this discrepancy is the flanking transmission of airborne sound through the bare fuselage surrounding the finite sized noise shield structure. This is possible due to the lateral surfaces around the loudspeaker array not being sealed off so that sound waves can propagate sideways (away from the noise shield), pass through the bare fuselage, and thus compromise the otherwise good sound insulation properties of the noise shield. Similar effects have been observed for example in [37] in the course of flight tests of enhanced acoustic cabin sidewall treatments with Helmholtz resonators. As shown in Appendix D, the noise reduction difference $\Delta\langle\mathrm{NR}\rangle$ only corresponds to the actual transmission loss difference of the two noise shield configurations under certain circumstances. Accordingly, the amount of sound power incident on the fuselage around the noise shield structure $W_{\mathrm{i,fsl}}$ should be very small compared to the incident sound power on the noise shield itself, $W_{\mathrm{i,shield}}$. Furthermore, the ΔTL-value should not be too high. Very large transmission loss differences

(e.g. due to anti-resonances of the MAM elements) cannot be captured with $\Delta\langle \mathrm{NR} \rangle$, because most of the total incident sound power bypasses the noise shield around the flanking paths and contributes to the average SPL inside the cabin. In order to illustrate the consequences of this effect, the dashed lines in Fig. 4.14(b) indicate the actual $\Delta\langle \mathrm{NR} \rangle$ calculated using Eq. (D.6). For that, an incident sound power ratio of $W_{\mathrm{i,fsl}}/W_{\mathrm{i,shield}} = 0.1$ is assumed and the transmission loss values of the different noise shield configurations are taken from the transfer matrix results. This shows that the maximum noise reduction difference at the first MAM anti-resonance is drastically reduced from over 20 dB to approximately 9 dB if the acoustic flanking is taken into account. It is expected that the structure-borne sound coupling between the noise shield and the fuselage further reduces the measured $\Delta\langle \mathrm{NR} \rangle$-values. Compared to that, the noise reduction difference minimum at about 100 Hz (in the analytical calculations) due to the panel resonance in Fig. 4.14(b) is completely unaffected by the flanking paths.

According to the discussion above, the measurement results for the noise shield demonstrator shown in Fig. 4.14(a) have to be viewed in the light of possible acoustic flanking paths. These are unavoidable in the given measurement environment. The measured $\Delta\langle \mathrm{NR} \rangle$-peak value of 3 dB at the MAM anti-resonances serves only as a lower bound of the actual ΔTL-value of the MAM noise shield compared to the double wall. This value can be considerably higher than the $\Delta\langle \mathrm{NR} \rangle$, depending on the amount of sound power bypassing the noise shield via flanking paths. Nevertheless, the measurement results provide a strong indication that the MAMs are effective even in this very complex structural environment. However, the flanking sound paths are a very important factor which needs to be carefully taken into account in the design of aircraft noise shields.

4.3.3. Results for tonal noise excitation

The measurement results for the noise reduction difference of the noise shields with respect to the ⟨NR⟩ of the fuselage under tonal noise excitation at $f = 100$ Hz with different trace wave numbers are shown in Fig. 4.15. The first row in Fig. 4.15 shows the results for the excitation sound wave propagating purely in axial direction (k_x) at three different trace wave numbers 2.5, 5.5, and 8.5 rad/m. In the second row, the excitation sound wave propagates in a 45° angle along the noise shield (k_{xy}) at the same three trace wave numbers. The third row shows the results for excitation waves propagating in circumferential direction (k_y).

In the pink noise excitation results in Fig. 4.13(b), it could be seen that at 100 Hz the noise reduction difference of the MAM noise shield is approximately 3 dB. The noise reduction of the other noise shield

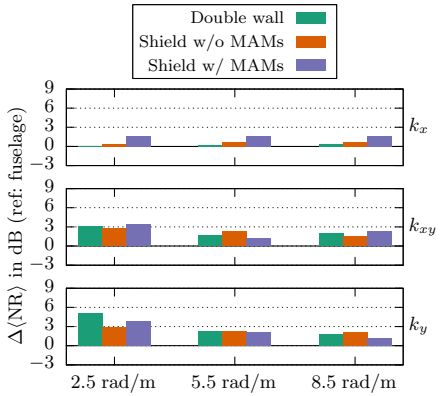

Figure 4.15: Measured average noise reduction differences for the different noise shield configurations at tonal noise excitation ($f = 100$ Hz) with different trace wave numbers.

configurations is slightly below 1 dB. The tonal excitation results with different wave numbers in Fig. 4.15 indicate that the noise reduction differences of all three noise shield designs strongly depend on the characteristics of the excitation field. For example, in the case of an excitation with $k_{xy} = 2.5\,\mathrm{rad/m}$ or $k_y = 2.5\,\mathrm{rad/m}$, the $\Delta\langle\mathrm{NR}\rangle$-value of the MAM noise shield is similar to the value obtained under pink noise excitation. On the other hand, in all three k_x-cases, the $\Delta\langle\mathrm{NR}\rangle$ of the MAM noise shield is only half of that value. For the other two noise shield configurations shown in Fig. 4.15, a negligible noise reduction difference can be observed for the k_x-cases. For $k_y = 2.5\,\mathrm{rad/m}$, however, the double wall yields the biggest noise reduction improvement of all three noise shields, even though it is the lightest design and does not contain any MAMs.

Therefore, no clear conclusions can be drawn from these measurement results under tonal noise excitation. For example, in all three k_x-cases the measured $\Delta\langle\mathrm{NR}\rangle$-values seem to be independent from the actual trace wave number. This is consistent with the analytical predictions in previous chapters, where it was shown that the anti-resonances of MAMs are not affected by the nature of the incident sound field, as long as the unit cells are smaller than the acoustic wavelength. For the other wave directions, k_{xy} and k_y, however, the $\Delta\langle\mathrm{NR}\rangle$ of the MAM noise shield varies considerably with the magnitude of the trace wave number. In the case of k_y-waves, for example, the MAM noise shield has a $\Delta\langle\mathrm{NR}\rangle$ of nearly 4 dB at the smallest trace wave number and drops to slightly above 1 dB at the largest value of k_y. Since the other two noise shield designs also exhibit large variations for these two wave direction cases, it can be expected that this is more likely a result of the global behavior of the noise shield response to the acoustical excitation. It is possible that the noise shield structure exhibits different structural and acoustical modes, depending on what is integrated into the air gap between the fuselage and the cover sheet. Furthermore, it

is possible that the acoustic flanking paths in the measurements also depend on the excitation characteristics. An effect inherent only to the MAM layers, therefore, seems unlikely to be the cause for the strong wave number and direction dependence of the noise reduction performance of the noise shield.

5. Conclusions and outlook

The aim of this work was to investigate the applicability of MAMs as acoustic treatments inside an aircraft fuselage noise shield for the reduction of low-frequency tonal noise produced by counter-rotating open rotor engines. Analytical models for the efficient prediction of the oblique incidence sound transmission properties of MAMs (both unit cell and multi-cell arrangements) and multi-layered structures with integrated MAM layers were developed. These models were verified and validated using FEM simulations and experiments, respectively. Parameter studies were performed using these analytical models in order to identify the most important parameters relevant for the design of noise shields with MAMs. Based upon these results, a MAM noise shield demonstrator with realistic dimensions was designed and evaluated experimentally on an acoustic fuselage demonstrator under different broadband and tonal noise excitation conditions.

In summary, the research questions for this work, as formulated in Section 1.3, can be answered as follows:

- In the analysis of the analytical models of MAM unit cells and multi-celled MAM panels in Chapter 2 it was shown that the anti-resonance characteristics of MAMs do not depend on the characteristics of the sound excitation and the overall dimensions of multi-celled panels. This is valid as long as the acoustic wavelength is large compared to the unit cell dimensions and the sound pressure acting on the MAMs is approximately uniform over each unit cell. Thus, under these conditions, MAMs still ex-

hibit significant TL maxima at their anti-resonances, even when more realistic sound excitation fields (e.g. diffuse fields) and finite sized multi-celled panels are considered. Furthermore, it could be shown that the membrane prestress variation in multi-celled arrangements, which cannot be avoided entirely due to manufacturing uncertainties, does not significantly impair the anti-resonance characteristics of the MAM panel.

- In the long wavelength limit, the effective surface mass density and the transfer matrix approach can be used to accurately and quickly estimate the sound reduction performance of multi-layered structures with MAMs. Certain assumptions inherent to the transfer matrix method, such as laterally unbounded and planar layers, limit the applicability of this method. However, the computational effectiveness of this approach makes it an excellent tool for the preliminary design process of such structures.

- Using the transfer matrix it could be shown that it is indeed possible to considerably enhance the low-frequency transmission loss of a double wall with MAMs. The anti-resonances of the MAM layers remain effective, but the bandwidth of the corresponding TL maxima can be greatly reduced when an improper design is chosen. For example, it was shown that a double wall design with integrated MAM layers should be as asymmetric as possible (e.g. by placing the MAMs very close to one of the walls) in order to retain a reasonable anti-resonance bandwidth.

- Finally, the measurements of the full-scale noise shield model on an acoustic fuselage demonstrator indicated the effectiveness of MAMs in a much more complex and realistic noise shield setup. Under pink noise excitation, a noise reduction improvement by up to 3 dB (compared to the noise shield without MAMs) could be

identified around 100 Hz. This improvement could be attributed to the anti-resonances of the MAM layers. However, it was possibly diminished by potential acoustic flanking paths in the test setup. Furthermore, in the tonal excitation measurements, a considerable dependence of the MAM shield noise reduction performance on the spatial characteristics of the excitation field could be identified.

All in all, these answers to the research questions of this thesis accomplish a significant step forward to the industrial application of membrane-type acoustic metamaterials as low-frequency acoustic treatments within aircraft noise shields. However, new open questions have been identified in the framework of this thesis, which should be addressed in further research efforts. The most important questions are:

- How significant is the influence of the acoustic flanking paths in the experimental setup on the fuselage demonstrator test bench? How can these be avoided?
- What is the physical explanation for the large differences in the noise reduction performance of the MAM noise shield in case of the different tonal excitation fields?
- How can the frequency shifting of the MAM anti-resonances in case of non-rigid attachment to the host structure be accounted for in the analytical models?

It can be expected that by answering these open questions, the MAM noise shield concept can achieve technology readiness level (TRL) 5 [56]. This enables the development of industrial-scale prototypes for reaching the next TRL.

In addition to that, the analytical models that were derived in this thesis provide a new and efficient framework to investigate sound insulation structures containing MAMs. The models are not restricted to be

applied for noise mitigation in aircraft structures, but they can be used in many different fields of noise control engineering, e.g. noise in cars or trains and building acoustics. Furthermore, the analytical models can be employed to develop innovative concepts for new acoustic metamaterials. For example, the analytical models in this work have been successfully applied to develop MAMs with adjustable acoustic properties which can modify their (anti-)resonance frequencies in situ by applying a static pressurization to the membrane [38]. This approach might be useful when the tonal components in the noise spectrum change over time, e.g. due to shaft rotation speed variations in CROR engines at the different flight phases. Another technological enhancement of MAMs employs perforations inside the mass and membrane material to introduce additional anti-resonances and improve the sound absorption capabilities of MAMs without introducing additional mass penalties [39]. This concept also has been developed based upon the analytical models from this work.

As a final conclusion, the results in the present work have shown that MAMs offer a great potential for improving the low-frequency noise reduction of conventional sound insulation structures. The noise shield demonstrator measurements, however, have also identified that – even almost ten years after their first appearance – the successful application of MAMs in practice still is a challenging problem. But the analytical models that were developed in this work can support the solution of this problem such that one day MAMs could be used to address low-frequency noise issues in aircraft, cars, trains, buildings, and many other environments.

Bibliography

[1] J. Allard and Y. Champoux. New empirical equations for sound propagation in rigid frame fibrous materials. *The Journal of the Acoustical Society of America*, 91(6):3346–3353, 1992.

[2] J. F. Allard and N. Atalla. *Propagation of Sound in Porous Media: Modelling Sound Absorbing Materials*. John Wiley & Sons, Chichester, 2nd edition, 2009.

[3] American Society for Testing and Materials ASTM E2611-09. Standard test method for measurement of normal incidence sound transmission of acoustical materials based on the transfer matrix method, 2009.

[4] M. R. Bai and M. Tsao. Estimation of sound power of baffled planar sources using radiation matrices. *The Journal of the Acoustical Society of America*, 112(3):876–883, 2002.

[5] B. Banerjee. *An Introduction to Metamaterials and Waves in Composites*. Taylor & Francis, Boca Raton, 2011.

[6] D. A. Bies and C. H. Hansen. *Engineering Noise Control: Theory and Practice*. Spon Press, London, 3rd edition, 2003.

[7] M. G. Blevins. *Design and Optimization of Membrane-Type Acoustic Metamaterials*. PhD thesis, University of Nebraska-Lincoln, 2016.

[8] I. U. Borchers, S. T. Laemmlein, P. Bartels, A. Rausch, M. Faust, J. A. F. Coebergh, and K. Koeble. Acoustic protection on payload fairings of expendable launch vehicles, Sept. 23 1997. US Patent

5,670,758.

[9] B. Brouard, D. Lafarge, and J.-F. Allard. A general method of modelling sound propagation in layered media. *Journal of Sound and Vibration*, 183(1):129–142, 1995.

[10] Y. Chen, G. Huang, X. Zhou, G. Hu, and C.-T. Sun. Analytical coupled vibroacoustic modeling of membrane-type acoustic metamaterials: Membrane model. *The Journal of the Acoustical Society of America*, 136(3):969–979, 2014.

[11] Y. Chen, G. Huang, X. Zhou, G. Hu, and C.-T. Sun. Analytical coupled vibroacoustic modeling of membrane-type acoustic metamaterials: Plate model. *The Journal of the Acoustical Society of America*, 136(6):2926–2934, 2014.

[12] Y. Cheng, C. Zhou, B. G. Yuan, D. J. Wu, Q. Wei, and X. J. Liu. Ultra-sparse metasurface for high reflection of low-frequency sound based on artificial Mie resonances. *Nature Materials*, 14 (10):1013–1019, 2015.

[13] H. Cohen and G. Handelman. On the vibration of a circular membrane with added mass. *The Journal of the Acoustical Society of America*, 29(2):229–233, 1957.

[14] M. J. Crocker. *Handbook of Noise and Vibration Control*. John Wiley & Sons, Hoboken, New Jersey, 2007.

[15] S. A. Cummer, J. Christensen, and A. Alù. Controlling sound with acoustic metamaterials. *Nature Reviews Materials*, 1:16001, 2016.

[16] S. J. Elliott and M. E. Johnson. Radiation modes and the active control of sound power. *The Journal of the Acoustical Society of America*, 94(4):2194–2204, 1993.

[17] S. J. Elliott and P. A. Nelson. Active noise control. *Signal Processing Magazine, IEEE*, 10(4):12–35, 1993.

[18] U. Emborg, F. Samuelsson, J. Holmgren, and S. Leth. Active and passive noise control in practice on the SAAB 2000 high speed turboprop. AIAA-Paper 98-2231, 1998.

[19] S. J. Estéve. *Control of sound transmission into payload fairings using distributed vibration absorbers and Helmholtz resonators.* PhD thesis, Virginia Polytechnic Institute and State University, 2004.

[20] S. J. Estéve and M. E. Johnson. Reduction of sound transmission into a circular cylindrical shell using distributed vibration absorbers and helmholtz resonators. *The Journal of the Acoustical Society of America*, 112(6):2840–2848, 2002.

[21] F. J. Fahy. *Foundations of Engineering Acoustics.* Elsevier Academic Press, San Diego, 2001.

[22] F. J. Fahy and P. Gardonio. *Sound and structural vibration: radiation, transmission and response.* Academic press, Oxford, UK, 2007.

[23] N. Fang, D. Xi, J. Xu, M. Ambati, W. Srituravanich, C. Sun, and X. Zhang. Ultrasonic metamaterials with negative modulus. *Nature Materials*, 5(6):452–456, 2006.

[24] H. J. Fuchs. *Schallabsorber und Schalldämpfer.* Springer, Berlin, 3rd edition, 2010.

[25] P. Gardonio. Review of active techniques for aerospace vibro-acoustic control. *Journal of Aircraft*, 39(2):206–214, 2002.

[26] J. F. Groeneweg and L. J. Bober. NASA advanced propeller research. NASA-TM-101361, 1988.

[27] S. Guenneau, A. Movchan, G. Pétursson, and S. A. Ramakrishna. Acoustic metamaterials for sound focusing and confinement. *New Journal of Physics*, 9(11):399, 2007.

[28] H. V. Henderson and S. R. Searle. On deriving the inverse of a

sum of matrices. *SIAM Review*, 23(1):53–60, 1981.

[29] A.-C. Hladky-Hennion and J.-N. Decarpigny. Analysis of the scattering of a plane acoustic wave by a doubly periodic structure using the finite element method: Application to alberich anechoic coatings. *The Journal of the Acoustical Society of America*, 90 (6):3356–3367, 1991.

[30] K. M. Ho, Z. Yang, X. X. Zhang, and P. Sheng. Measurements of sound transmission through panels of locally resonant materials between impedance tubes. *Applied Acoustics*, 66(7):751–765, 2005.

[31] T.-Y. Huang, C. Shen, and Y. Jing. Membrane- and plate-type acoustic metamaterials. *The Journal of the Acoustical Society of America*, 139(6):3240–3250, 2016.

[32] X. Jiang, B. Liang, R.-Q. Li, X.-Y. Zou, L.-L. Yin, and J.-C. Cheng. Ultra-broadband absorption by acoustic metamaterials. *Applied Physics Letters*, 105(24):243505, 2014.

[33] M. R. F. Kidner, C. R. Fuller, and B. Gardner. Increase in transmission loss of single panels by addition of mass inclusions to a poro-elastic layer: Experimental investigation. *Journal of Sound and Vibration*, 294(3):466–472, 2006.

[34] K. Kochan, D. Sachau, and H. Breitbach. Robust active noise control in the loadmaster area of a military transport aircraft. *The Journal of the Acoustical Society of America*, 129(5):3011–3019, 2011.

[35] E. T. Kornhauser and D. Mintzer. On the vibration of mass-loaded membranes. *The Journal of the Acoustical Society of America*, 25(5):903–906, 1953.

[36] H. L. Kuntz and R. A. Prydz. Interior noise in the untreated Gulfstream II Propfan Test Assessment aircraft. *Journal of Air-*

craft, 27(7):647–652, 1990.

[37] H. L. Kuntz, R. J. Gatineau, R. A. Prydz, and F. J. Balena. Development and testing of cabin sidewall acoustic resonators for the reduction of cabin tone levels in propfan-powered aircraft. NASA CR-4388, 1991.

[38] F. Langfeldt, J. Riecken, W. Gleine, and O. von Estorff. A membrane-type acoustic metamaterial with adjustable acoustic properties. *Journal of Sound and Vibration*, 373:1–18, 2016.

[39] F. Langfeldt, H. Kemsies, W. Gleine, and O. von Estorff. Perforated membrane-type acoustic metamaterials. *Physics Letters A*, 381(16):1457–1462, 2017.

[40] Lanitz-Prena GmbH. Technical data sheets, 2017. `https://www.oracover.de/index.php/sites2/view/7-1-technische_datenblaetter.html` (Accessed 6 January 2017).

[41] Lanitz-Prena GmbH. Weight table, 2017. `https://www.oracover.de/downloads2/datenblaetter/Foliengewichte_engl.pdf` (Accessed 6 January 2017).

[42] S. H. Lee, C. M. Park, Y. M. Seo, Z. G. Wang, and C. K. Kim. Acoustic metamaterial with negative modulus. *Journal of Physics: Condensed Matter*, 21(17):175704, 2009.

[43] S. H. Lee, C. M. Park, Y. M. Seo, Z. G. Wang, and C. K. Kim. Composite acoustic medium with simultaneously negative density and modulus. *Physical Review Letters*, 104(5):054301, 2010.

[44] A. W. Leissa. Vibration of plates. NASA SP-160, 1969.

[45] J. Li and C. T. Chan. Double-negative acoustic metamaterial. *Physical Review E*, 70(5):055602, 2004.

[46] J. Li, L. Fok, X. Yin, G. Bartal, and X. Zhang. Experimental demonstration of an acoustic magnifying hyperlens. *Nature ma-*

terials, 8(12):931–934, 2009.

[47] Y. Liu and X. Zhang. Metamaterials: a new frontier of science and technology. *Chemical Society Reviews*, 40(5):2494–2507, 2011.

[48] Z. Liu, X. Zhang, Y. Mao, Y. Y. Zhu, Z. Yang, C. T. Chan, and P. Sheng. Locally resonant sonic materials. *Science*, 289(5485): 1734–1736, 2000.

[49] Z. Liu, C. T. Chan, and P. Sheng. Analytic model of phononic crystals with local resonances. *Physical Review B*, 71(1):014103, 2005.

[50] M. Long. *Architectural Acoustics*. Elsevier, Amsterdam, 2005.

[51] K. Lühe. *Rechnerische und messtechnische Untersuchung zur Modellierung absorbierender Wandverkleidungen bei der akustischen Auslegung von Flugzeugkabinen*. B.Sc. thesis, Hamburg University of Applied Sciences, 2014.

[52] G. Ma. *Experimental Investigation of Locally Resonant Sonic Metamaterials in Sub-kHz Region*. M.Ph. thesis, Hong Kong University of Science and Technology, 2009.

[53] G. Ma. *Membrane-type acoustic metamaterials*. PhD thesis, Hong Kong University of Science and Technology, 2012.

[54] G. Ma, J. Mei, M. Yang, Z. Yang, W. Wen, and P. Sheng. Low-frequency total absorption with membrane-type acoustic metamaterial. In *Proceedings of the 19th ICSV*, Vilnius, Lithuania, 2012.

[55] G. Ma, M. Yang, Z. Yang, and P. Sheng. Low-frequency narrow-band acoustic filter with large orifice. *Applied Physics Letters*, 103(1):011903, 2013.

[56] J. C. Mankins. Technology readiness levels: A white Paper, 1995. `http://www.hq.nasa.gov/office/codeq/trl/trl.pdf` (Accessed 29 March 2017).

[57] D. N. May, K. J. Plotkin, R. G. Selden, and B. H. Sharp. Lightweight sidewalls for aircraft interior noise control. NASA CR-172490, 1985.

[58] D. J. McClure. Polyester (PET) film as a substrate: a tutorial. In *50th Annual Technical Conference Proceedings*, pages 692–699, Louisville, KY, 2007. Society of Vacuum Coaters.

[59] J. Mei, G. Ma, M. Yang, Z. Yang, W. Wen, and P. Sheng. Dark acoustic metamaterials as super absorbers for low-frequency sound. *Nature Communications*, 3:756, 2012.

[60] J. S. Mixson and J. F. Wilby. Interior noise. In H. H. Hubbard, editor, *Aeroacoustics of flight vehicles: theory and practice. Volume 2: Noise Control*. NASA, Washington, DC, 1991.

[61] M. Möser. *Technische Akustik*. Springer, Berlin, 10th edition, 2015.

[62] K. Nagaya and K. Poltorak. Method for solving eigenvalue problems of the helmholtz equation with a circular outer and a number of eccentric circular inner boundaries. *The Journal of the Acoustical Society of America*, 85(2):576–581, 1989.

[63] C. J. Naify, C.-M. Chang, G. McKnight, and S. Nutt. Transmission loss and dynamic response of membrane-type locally resonant acoustic metamaterials. *Journal of Applied Physics*, 108 (11):114905, 2010.

[64] C. J. Naify, C.-M. Chang, G. McKnight, and S. Nutt. Transmission loss of membrane-type acoustic metamaterials with coaxial ring masses. *Journal of Applied Physics*, 110(12):124903, 2011.

[65] C. J. Naify, C.-M. Chang, G. McKnight, F. Scheulen, and S. Nutt. Membrane-type metamaterials: Transmission loss of multi-celled arrays. *Journal of Applied Physics*, 109(10):104902, 2011.

[66] C. J. Naify, C.-M. Chang, G. McKnight, and S. R. Nutt. Scaling

of membrane-type locally resonant acoustic metamaterial arrays. *The Journal of the Acoustical Society of America*, 132(4):2784–92, 2012.

[67] C. M. Park, J. J. Park, S. H. Lee, Y. M. Seo, C. K. Kim, and S. H. Lee. Amplification of acoustic evanescent waves using metamaterial slabs. *Physical Review Letters*, 107(19):194301, 2011.

[68] J. J. Park, C. M. Park, K. J. B. Lee, and S. H. Lee. Acoustic superlens using membrane-based metamaterials. *Applied Physics Letters*, 106(5):051901, 2015.

[69] B. Parlett. *The Symmetric Eigenvalue Problem*. Society for Industrial and Applied Mathematics, Philadelphia, 1998.

[70] A. Peiffer, M. Grünewald, and P. Lempereur. Comment on "A lightweight yet sound-proof honeycomb acoustic metamaterial" [Appl. Phys. Lett. 106, 171905 (2015)]. *Applied Physics Letters*, 107(21):216101, 2015.

[71] J. B. Pendry. Negative refraction makes a perfect lens. *Physical Review Letters*, 85(18):3966–3969, 2000.

[72] J. B. Pendry, D. Schurig, and D. R. Smith. Controlling electromagnetic fields. *Science*, 312(5781):1780–1782, 2006.

[73] F. Pinto. Analytical and experimental investigation on a vibrating annular membrane attached to a central free, rigid core. *Journal of Sound and Vibration*, 291(3–5):1278–1287, 2006.

[74] B.-I. Popa, L. Zigoneanu, and S. A. Cummer. Experimental acoustic ground cloak in air. *Physical Review Letters*, 106(25): 253901, 2011.

[75] R. A. Prydz, L. S. Wirt, H. L. Kuntz, and L. D. Pope. Transmission loss of a multilayer panel with internal tuned helmholtz resonators. *The Journal of the Acoustical Society of America*, 87 (4):1597–1602, 1990.

[76] X. Qiu, J. Lu, and J. Pan. A new era for applications of active noise control. In *Proceedings of the 43th International Congress and Exposition on Noise Control Engineering (inter-noise 2014)*, Melbourne, 2014.

[77] S. A. Ramakrishna. Physics of negative refractive index materials. *Reports on Progress in Physics*, 68(2):449–521, 2005.

[78] J. D. Revell, F. J. Balena, and L. R. Koval. Interior noise control by fuselage design for high-speed propeller-driven aircraft. *Journal of Aircraft*, 19(1):39–45, 1982.

[79] W. Schirmer. *Technischer Lärmschutz*. Springer, Berlin, 2nd edition, 2006.

[80] D. Schurig, J. J. Mock, B. J. Justice, S. A. Cummer, J. B. Pendry, A. F. Starr, and D. R. Smith. Metamaterial electromagnetic cloak at microwave frequencies. *Science*, 314(5801):977–980, 2006.

[81] K. Sha, J. Yang, and W.-S. Gan. A simple calculation method for the self- and mutual-radiation impedance of flexible rectangular patches in a rigid infinite baffle. *Journal of Sound and Vibration*, 282(1–2):179–195, 2005.

[82] V. M. Shalaev. Transforming light. *Science*, 322(5900):384–386, 2008.

[83] B. H. Sharp. A study of techniques to increase the sound insulation of building elements. Wyle Laboratories Report WR 73-5, 1973.

[84] J. Sherman and W. J. Morrison. Adjustment of an inverse matrix corresponding to a change in one element of a given matrix. *The Annals of Mathematical Statistics*, 21(1):124–127, 1950.

[85] *Falcon 9 launch vehicle: payload user's guide*. Space Exploration Technologies Corp., October 2015.

[86] W. C. Strack, G. Knip, A. L. Weisbrich, J. Godston, and

E. Bradley. Technology and benefits of aircraft counter rotation propellers. NASA-TM-82983, 1982.

[87] M. Teschner, M. Wandel, A. Röder, P. Faulhaber, and S. Tewes. Coupling of multi-tone signatures and fuselage structures. In *Proceedings of Inter-Noise 2016*, pages 3286–3295, Hamburg, 2016.

[88] D. Thompson, P. Gardonio, and J. Rohlfing. Can a transmission coefficient be greater than unity? *Applied Acoustics*, 70(5):681–688, 2009.

[89] H. Tian, X. Wang, and Y.-H. Zhou. Theoretical model and analytical approach for a circular membrane-ring structure of locally resonant acoustic metamaterial. *Applied Physics A*, 114(3):985–990, 2013.

[90] C. van der Kelen and P. Göransson. Identification of the full anisotropic flow resistivity tensor for multiple glass wool and melamine foam samples. *The Journal of the Acoustical Society of America*, 134(6):4659–4669, 2013.

[91] J. van Dyke, J. Schendel, C. Gunderson, and M. Ballard. Cabin noise reduction in the DC-9. AIAA Paper 67-401, 1967.

[92] B. van Genechten, B. Pluymers, C. Vanmaele, D. Vandepitte, and W. Desmet. Application of modal model reduction for hybrid structural Finite Element–Acoustic Wave Based models. In *Proceedings of the 14th International Congress on Sound & Vibration*, Cairns, 2007.

[93] S. Varanasi, J. S. Bolton, and T. Siegmund. Experiments on the low frequency barrier characteristics of cellular metamaterial panels in a diffuse sound field. *The Journal of the Acoustical Society of America*, 141(1):602–610, 2017.

[94] I. L. Vér and L. L. Beranek. *Noise and vibration control engineering: principles and applications*. John Wiley & Sons, Inc.,

2nd edition, 2006.

[95] K. Verdière, R. Panneton, S. Elkoun, T. Dupont, and P. Leclaire. Transfer matrix method applied to the parallel assembly of sound absorbing materials. *The Journal of the Acoustical Society of America*, 134(6):4648–4658, 2013.

[96] V. G. Veselago. The electrodynamics of substances with simultaneously negative values of ϵ and μ. *Soviet Physics Uspekhi*, 10 (4):509–514, 1968.

[97] M. Wandel and H. Scheel. Design Requirements of Acoustic Flight LAB Platform. In *Proceedings of Inter-Noise 2016*, pages 3264–3273, Hamburg, 2016.

[98] C. Y. Wang. Vibration of an annular membrane attached to a free, rigid core. *Journal of Sound and Vibration*, 260(4):776–782, 2003.

[99] C. Y. Wang. Vibration of a circular plate with an attached core. *Journal of Sound and Vibration*, 280(3–5):1075–1082, 2005.

[100] X. Wang, H. Zhao, X. Luo, and Z. Huang. Membrane-constrained acoustic metamaterials for low frequency sound insulation. *Applied Physics Letters*, 108(4):041905, 2016.

[101] Wikipedia. Tupolev Tu-114, 2017. `https://en.wikipedia.org/w/index.php?title=Tupolev_Tu-114&oldid=788385732` (Accessed 6 September 2017).

[102] J. F. Wilby. Aircraft interior noise. *Journal of Sound and Vibration*, 190(3):545–564, 1996.

[103] J. F. Wilby, D. C. Rennison, E. G. Wilby, and A. H. Marsh. Noise control prediction for high-speed, propeller-driven aircraft. AIAA-Paper 80-0999, 1980.

[104] C. Yang and L. Cheng. Sound absorption of microperforated panels inside compact acoustic enclosures. *Journal of Sound and*

Vibration, 360:140–155, 2016.

[105] M. Yang, G. Ma, Z. Yang, and P. Sheng. Coupled membranes with doubly negative mass density and bulk modulus. *Physical Review Letters*, 110:134301, 2013.

[106] M. Yang, Y. Li, C. Meng, C. Fu, J. Mei, Z. Yang, and P. Sheng. Sound absorption by subwavelength membrane structures: A geometric perspective. *Comptes Rendus Mécanique*, 343(12):635–644, 2015.

[107] Z. Yang, J. Mei, M. Yang, N. H. Chan, and P. Sheng. Membrane-type acoustic metamaterial with negative dynamic mass. *Physical Review Letters*, 101(20):204301, 2008.

[108] Z. Yang, H. M. Dai, N. H. Chan, G. C. Ma, and P. Sheng. Acoustic metamaterial panels for sound attenuation in the 50–1000 Hz regime. *Applied Physics Letters*, 96(4):041906, 2010.

[109] Z. Y. Yang, W. Wen, P. Sheng, and X. Zhang. Sound attenuating structures, July 8 2008. US Patent 7,395,898.

[110] S. Zhang, C. Xia, and N. Fang. Broadband acoustic cloak for ultrasound waves. *Physical Review Letters*, 106(2):024301, 2011.

[111] X. Zhang and Z. Liu. Superlenses to overcome the diffraction limit. *Nature Materials*, 7(6):435–441, 2008.

[112] Y. Zhang, J. Wen, Y. Xiao, X. Wen, and J. Wang. Theoretical investigation of the sound attenuation of membrane-type acoustic metamaterials. *Physics Letters A*, 376(17):1489–1494, 2012.

[113] Y. Zhang, J. Wen, H. Zhao, D. Yu, L. Cai, and X. Wen. Sound insulation property of membrane-type acoustic metamaterials carrying different masses at adjacent cells. *Journal of Applied Physics*, 114(6):063515, 2013.

[114] J. Zhao, Z. N. Chen, B. Li, and C.-W. Qiu. Acoustic cloaking by extraordinary sound transmission. *Journal of Applied Physics*,

117(21):214507, 2015.

Appendix

A. Extension of the unit cell model to multiple masses

The analytical model for MAM unit cells derived in Section 2.1 can be readily extended to account for multiple added masses in a single unit cell. This can be useful in some applications, e.g. to introduce additional anti-resonances and increase the bandwidth of the MAM [59, 64].

Let N_M be the number of masses added to the MAM unit cell and $i = 1 \dots N_\mathrm{M}$ be the running index referring to one of the added masses. Each mass i can be characterized using a non-dimensional local Cartesian coordinate system $(\xi_i', \eta_i', \zeta_i')$, rotation angle θ_i', and global center of gravity coordinates ξ_i^*, η_i^*, and ζ_i^*. The dimensionless mass magnitude and squared radii of gyration of the i-th mass are denoted by $\mu^{(i)}$ as well as $\vartheta_{\xi_i'}^{(i)}$ and $\vartheta_{\eta_i'}^{(i)}$, respectively. After employing the point matching approach and distributing point forces along the common surfaces between the masses and the membrane, the dimensionless membrane-mass interaction stress γ'' is given by a summation over the masses as

$$\gamma'' \approx \sum_{i=1}^{N_\mathrm{M}} \sum_{j=1}^{I_i} \gamma_{ij} \delta(\xi - \xi_{ij})\, \delta(\eta - \eta_{ij})\,, \tag{A.1}$$

where I_i is the number of matching points for the i-th mass and γ_{ij} is the dimensionless point force of the j-th matching point of the i-th

mass at the global coordinates ξ_{ij} and η_{ij}. Hence, the total number of matching points for the MAM unit cell is given by $I = \sum_{i=1}^{N_\mathrm{M}} I_i$. The mass equations of motion (2.17) can be formulated for each mass individually and expressed in matrix form as

$$\Omega^2 \mathbf{u}_\mathrm{M}^{(i)} = \mathbf{Q}^{(i)} \boldsymbol{\gamma}^{(i)}, \tag{A.2}$$

where $\mathbf{Q}^{(i)}$ is calculated using Eq. (2.20) with μ, $\vartheta_{\xi'}$, $\vartheta_{\eta'}$, and the matching point coordinates ξ_j' and η_j' corresponding to those of the mass i. Eq. (2.18) then corresponds to the assembly of Eq. (A.2) for all N_M masses, where $\mathbf{u}_\mathrm{M} \in \mathbb{C}^{3N_\mathrm{M}}$ and $\boldsymbol{\gamma} \in \mathbb{C}^I$ are constructed from the scaled degrees of freedom and the matching point forces of all masses, respectively, and $\mathbf{Q} \in \mathbb{R}^{3N_\mathrm{M} \times I}$ is given by

$$\mathbf{Q} = \begin{bmatrix} \mathbf{Q}^{(1)} & & \mathbf{0} \\ & \ddots & \\ \mathbf{0} & & \mathbf{Q}^{(N_\mathrm{M})} \end{bmatrix}. \tag{A.3}$$

The same principle applies to the continuity condition in Eq. (2.21), which also can be formulated for each mass i individually. From this it follows that in matrix form the continuity condition still can be expressed as

$$\mathbf{L}^\mathrm{T} \mathbf{c} = \mathbf{Q}^\mathrm{T} \mathbf{u}_\mathrm{M}, \tag{2.22}$$

but $\mathbf{L}$ now is a N by I matrix with the elements given by

$$l_{mnij} = \Phi_{mn}^{(ij)} = 2 \sin(m\pi\xi_{ij}) \sin(n\pi\eta_{ij}). \tag{A.4}$$

From this it follows that if multiple masses within a MAM unit cell are to be considered in the analytical model in Section 2.1, only the matrices $\mathbf{Q}$ and $\mathbf{L}$ have to be replaced by Eqs. (A.3) and (A.4), respectively. Apart from that, the remaining procedures, such as the eigenmode extraction or the fluid-structure coupling, remain unchanged. For

the sake of completeness, however, it should be noted that in the case of N_M added masses, the rank of the matrix $\mathbf{B}$ in Eq. (2.28) is $N + 3N_\mathrm{M}$.

In a similar manner, the analytical model for MAM arrays from Section 2.2 can also be used when MAM unit cells with multiple masses are to be considered. In that case, the system of equations (2.77) is of size $(N_{pq} + 3N_{\mathrm{M},pq} + I_{pq})$ by $(N_{pq} + 3N_{\mathrm{M},pq} + I_{pq})$, where $N_{\mathrm{M},pq}$ is the number of masses within the unit cell (p, q). The matrices $\mathbf{Q}_{pq}$ and $\mathbf{L}_{pq}$ in Eq. (2.77) are obtained from Eqs. (A.3) and (A.4), respectively.

B. Reduction of the MAM eigenvalue problem

The reduction of the generalized eigenvalue problem in Eq. (2.28) is performed by taking the singular value decomposition of the non-zero upper right blocks in $\mathbf{A}$ as

$$\begin{bmatrix} -\mathbf{L} \\ \mathbf{Q} \end{bmatrix} = \underbrace{\begin{bmatrix} \boldsymbol{\mathcal{U}}_{11} & \boldsymbol{\mathcal{U}}_{12} \\ \boldsymbol{\mathcal{U}}_{21} & \boldsymbol{\mathcal{U}}_{22} \end{bmatrix}}_{\boldsymbol{\mathcal{U}}} \begin{bmatrix} \boldsymbol{\Sigma} \\ \mathbf{0} \end{bmatrix} \boldsymbol{\mathcal{V}}^\mathrm{T}, \tag{B.1}$$

where $\boldsymbol{\mathcal{U}}$ and $\boldsymbol{\mathcal{V}}$ are orthonormal and $\boldsymbol{\Sigma}$ is diagonal positive-definite containing the singular values of the decomposed matrix. With the orthonormal transformation matrix $\boldsymbol{\mathcal{S}} = \mathrm{diag}([\boldsymbol{\mathcal{U}}, \boldsymbol{\mathcal{V}}])$, Eq. (2.29) can be transformed into

$$\widetilde{\mathbf{A}}\widetilde{\mathbf{v}}_i = \Omega_i^2 \mathbf{B}\widetilde{\mathbf{v}}_i, \tag{B.2}$$

where

$$\widetilde{\mathbf{A}} = \boldsymbol{\mathcal{S}}^\mathrm{T}\mathbf{A}\boldsymbol{\mathcal{S}} = \begin{bmatrix} \boldsymbol{\mathcal{U}}_{11}^\mathrm{T}\mathbf{C}\boldsymbol{\mathcal{U}}_{11} & \boldsymbol{\mathcal{U}}_{11}^\mathrm{T}\mathbf{C}\boldsymbol{\mathcal{U}}_{12} & \boldsymbol{\Sigma} \\ \boldsymbol{\mathcal{U}}_{12}^\mathrm{T}\mathbf{C}\boldsymbol{\mathcal{U}}_{11} & \boldsymbol{\mathcal{U}}_{12}^\mathrm{T}\mathbf{C}\boldsymbol{\mathcal{U}}_{12} & \mathbf{0} \\ \boldsymbol{\Sigma} & \mathbf{0} & \mathbf{0} \end{bmatrix} \tag{B.3}$$

and $\widetilde{\mathbf{v}}_i = \boldsymbol{\mathcal{S}}^\mathrm{T}\mathbf{v}_i$. The special form of Eq. (B.2) can be exploited to retrieve the finite eigenfrequencies Ω_i^2 and the associated transformed

eigenvectors $\widetilde{\mathbf{v}}_i$ from the symmetric standard eigenvalue problem [69]

$$\boldsymbol{\mathcal{U}}_{12}^{\mathrm{T}}\mathbf{C}\boldsymbol{\mathcal{U}}_{12}\widetilde{\mathbf{w}}_i = \Omega_i^2\widetilde{\mathbf{w}}_i \tag{B.4}$$

and the relationship

$$\widetilde{\mathbf{v}}_i = \underbrace{\begin{bmatrix} \mathbf{0} \\ \mathbf{I} \\ -\boldsymbol{\Sigma}^{-1}\boldsymbol{\mathcal{U}}_{11}^{\mathrm{T}}\mathbf{C}\boldsymbol{\mathcal{U}}_{12} \end{bmatrix}}_{\widetilde{\boldsymbol{\mathcal{S}}}} \widetilde{\mathbf{w}}_i. \tag{B.5}$$

Since Eq. (B.4) is a symmetric eigenvalue problem, there exists a full set of orthonormal eigenvectors $\widetilde{\mathbf{W}}$ which transforms the system matrix in Eq. (B.4) into diagonal form, i.e. $\widetilde{\mathbf{W}}^{\mathrm{T}}\boldsymbol{\mathcal{U}}_{12}^{\mathrm{T}}\mathbf{C}\boldsymbol{\mathcal{U}}_{12}\widetilde{\mathbf{W}} = \boldsymbol{\Lambda}$. $\boldsymbol{\Lambda}$ is a diagonal matrix containing the squared eigenfrequencies Ω_i^2 of the MAM unit cell associated to the eigenvectors $\widetilde{\mathbf{w}}_i$. The eigenvectors of the original system (2.29) are related to $\widetilde{\mathbf{w}}_i$ via $\mathbf{v}_i = \boldsymbol{\mathcal{S}}\widetilde{\boldsymbol{\mathcal{S}}}\widetilde{\mathbf{w}}_i$. Thus, the set $\mathbf{V}$ containing the MAM eigenvectors $\mathbf{v}_i$ is given by $\mathbf{V} = \boldsymbol{\mathcal{S}}\widetilde{\boldsymbol{\mathcal{S}}}\widetilde{\mathbf{W}}$. It can be shown that this set of eigenvectors simultaneously diagonalizes the system matrices $\mathbf{A}$ and $\mathbf{B}$ in Eq. (2.29), because

$$\mathbf{V}^{\mathrm{T}}\mathbf{A}\mathbf{V} = \widetilde{\mathbf{W}}^{\mathrm{T}}\widetilde{\boldsymbol{\mathcal{S}}}^{\mathrm{T}}\widetilde{\mathbf{A}}\widetilde{\boldsymbol{\mathcal{S}}}\widetilde{\mathbf{W}} = \widetilde{\mathbf{W}}^{\mathrm{T}}\boldsymbol{\mathcal{U}}_{12}^{\mathrm{T}}\mathbf{C}\boldsymbol{\mathcal{U}}_{12}\widetilde{\mathbf{W}} = \boldsymbol{\Lambda} \tag{B.6}$$

and

$$\mathbf{V}^{\mathrm{T}}\mathbf{B}\mathbf{V} = \widetilde{\mathbf{W}}^{\mathrm{T}}\widetilde{\boldsymbol{\mathcal{S}}}^{\mathrm{T}}\mathbf{B}\widetilde{\boldsymbol{\mathcal{S}}}\widetilde{\mathbf{W}} = \widetilde{\mathbf{W}}^{\mathrm{T}}\widetilde{\mathbf{W}} = \mathbf{I}. \tag{B.7}$$

C. Simplified expression for the MAM unit cell transmission factor

In order to derive a simplified expression for the transmission factor of a MAM unit cell at low frequencies (i.e. $\kappa_0 = k_0 L_x \ll 1$), the system

of equations (2.56) can be rewritten as

$$(\mathbf{A}_{\text{vac}} + \mathbf{A}_{\text{rad}})\,\mathbf{x} = \mathbf{y}. \tag{C.1}$$

$$\mathbf{A}_{\text{vac}} = \begin{bmatrix} \mathbf{C} - \Omega^2\mathbf{I} & \mathbf{0} & -\mathbf{L} \\ \mathbf{0} & -\Omega^2\mathbf{I} & \mathbf{Q} \\ -\mathbf{L}^{\mathrm{T}} & \mathbf{Q}^{\mathrm{T}} & \mathbf{0} \end{bmatrix} \tag{C.2}$$

is the coefficient matrix for the in vacuo MAM unit cell (i.e. no coupling between the MAM vibration and the reradiated pressure field),

$$\mathbf{A}_{\text{rad}} = \mathrm{i}\Omega \begin{bmatrix} \boldsymbol{\Xi} & \mathbf{0} & \mathbf{0} \\ \mathbf{0} & \mathbf{0} & \mathbf{0} \\ \mathbf{0} & \mathbf{0} & \mathbf{0} \end{bmatrix} \tag{C.3}$$

contains the radiation impedance matrix from the fluid-structure interaction model, $\mathbf{x}^{\mathrm{T}} = (\mathbf{c}^{\mathrm{T}}, \mathbf{u}_{\mathrm{M}}^{\mathrm{T}}, \boldsymbol{\gamma}^{\mathrm{T}})/(2\beta_{\mathrm{i}0})$, and $\mathbf{y}^{\mathrm{T}} = (\mathbf{b}^{\mathrm{T}}, \mathbf{0}^{\mathrm{T}}, \mathbf{0}^{\mathrm{T}})$. Thus, Eq. (2.67) can be written in terms of the inversion of Eq. (C.1) as

$$\tilde{t}_{\theta_{\mathrm{i}}} = \frac{2\mathcal{Z}_0\mathrm{i}\Omega}{\cos\theta_{\mathrm{i}}}\mathbf{y}^{\mathrm{H}}\mathbf{x} = \frac{2\mathcal{Z}_0\mathrm{i}\Omega}{\cos\theta_{\mathrm{i}}}\mathbf{y}^{\mathrm{H}}(\mathbf{A}_{\text{vac}} + \mathbf{A}_{\text{rad}})^{-1}\,\mathbf{y}. \tag{C.4}$$

The definition of the radiation impedance matrix $\boldsymbol{\Xi}$ in Eq. (2.57) can be written as

$$\boldsymbol{\Xi} = 2\kappa_0\mathcal{Z}_0 \sum_{rs} \frac{\mathbf{r}_{rs}\mathbf{r}_{rs}^{\mathrm{H}}}{\kappa_{rs}} = 2\kappa_0\mathcal{Z}_0 \frac{\mathbf{r}_{00}\mathbf{r}_{00}^{\mathrm{H}}}{\kappa_{00}} + 2\kappa_0\mathcal{Z}_0 \sum_{\substack{rs \\ (r,s)\neq(0,0)}} \frac{\mathbf{r}_{rs}\mathbf{r}_{rs}^{\mathrm{H}}}{\kappa_{rs}}, \tag{C.5}$$

where the zero-order fluid mode ($r = s = 0$) has been isolated from the summation. Noting that for this fluid mode $\kappa_{00} = \kappa_0 \cos\theta_{\mathrm{i}}$ and $\mathbf{r}_{00} = \mathbf{b}$ (see Section 2.1.4), Eq. (C.5) can be rewritten as

$$\boldsymbol{\Xi} = \frac{2\mathcal{Z}_0}{\cos\theta_{\mathrm{i}}}\mathbf{b}\mathbf{b}^{\mathrm{H}} + 2\mathcal{Z}_0 \sum_{\substack{rs \\ (r,s)\neq(0,0)}} \frac{\kappa_0}{\kappa_{rs}}\mathbf{r}_{rs}\mathbf{r}_{rs}^{\mathrm{H}}. \tag{C.6}$$

For very small values of κ_0, the ratio κ_0/κ_{rs} in the summation in Eq. (C.6) can be approximated up to first order as

$$\frac{\kappa_0}{\kappa_{rs}} \approx -\frac{\kappa_0}{\mathrm{i}2\pi\sqrt{r^2+\Lambda^2 s^2}} + \mathcal{O}(\kappa_0^2). \tag{C.7}$$

Inserting this into Eq. (C.6) and neglecting the second and higher order terms of κ_0 yields

$$\boldsymbol{\Xi} \approx \frac{2\mathcal{Z}_0}{\cos\theta_\mathrm{i}}\mathbf{b}\mathbf{b}^\mathrm{H} + \frac{\mathrm{i}\kappa_0\mathcal{Z}_0}{\pi}\sum_{\substack{rs\\(r,s)\neq(0,0)}}\frac{\mathbf{r}_{rs}\mathbf{r}_{rs}^\mathrm{H}}{\sqrt{r^2+\Lambda^2 s^2}}. \tag{C.8}$$

Noting that for $\kappa_0 \ll 1$ the contribution of the summation in Eq. (C.8) is small compared to the first summand (which does not depend on κ_0), the imaginary part of $\boldsymbol{\Xi}$ can be neglected in the low-frequency regime. Thus, as a low-frequency approximation, the radiation impedance matrix is calculated by considering only the plane wave mode of the surrounding fluid space:

$$\boldsymbol{\Xi} \approx \frac{2\mathcal{Z}_0}{\cos\theta_\mathrm{i}}\mathbf{b}\mathbf{b}^\mathrm{H}. \tag{C.9}$$

Consequently, the simplified form of $\mathbf{A}_\mathrm{rad}$ in Eq. (C.4) is given by

$$\mathbf{A}_\mathrm{rad} \approx \frac{2\mathcal{Z}_0\mathrm{i}\Omega}{\cos\theta_\mathrm{i}}\begin{bmatrix}\mathbf{b}\mathbf{b}^\mathrm{H} & \mathbf{0} & \mathbf{0}\\ \mathbf{0} & \mathbf{0} & \mathbf{0}\\ \mathbf{0} & \mathbf{0} & \mathbf{0}\end{bmatrix} = \frac{2\mathcal{Z}_0\mathrm{i}\Omega}{\cos\theta_\mathrm{i}}\mathbf{y}\mathbf{y}^\mathrm{H}, \tag{C.10}$$

which can be inserted into Eq. (C.4) to yield

$$\tilde{t}_{\theta_\mathrm{i}} \approx \frac{2\mathcal{Z}_0\mathrm{i}\Omega}{\cos\theta_\mathrm{i}}\mathbf{y}^\mathrm{H}\left(\mathbf{A}_\mathrm{vac} + \frac{2\mathcal{Z}_0\mathrm{i}\Omega}{\cos\theta_\mathrm{i}}\mathbf{y}\mathbf{y}^\mathrm{H}\right)^{-1}\mathbf{y}. \tag{C.11}$$

The inverse of the matrix sum in Eq. (C.11) is given by the Sherman–Morrison formula [28, 84]

$$\left(\mathbf{A}_\mathrm{vac} + \frac{2\mathcal{Z}_0\mathrm{i}\Omega}{\cos\theta_\mathrm{i}}\mathbf{y}\mathbf{y}^\mathrm{H}\right)^{-1} = \mathbf{A}_\mathrm{vac}^{-1} - \frac{\mathbf{A}_\mathrm{vac}^{-1}\mathbf{y}\mathbf{y}^\mathrm{H}\mathbf{A}_\mathrm{vac}^{-1}}{\frac{\cos\theta_\mathrm{i}}{2\mathcal{Z}_0\mathrm{i}\Omega} + \mathbf{y}^\mathrm{H}\mathbf{A}_\mathrm{vac}^{-1}\mathbf{y}} \tag{C.12}$$

and thus Eq. (C.11) can be simplified to

$$\tilde{t}_{\theta_\mathrm{i}} \approx \frac{1}{1+\frac{\cos\theta_\mathrm{i}}{2\mathcal{Z}_0\mathrm{i}\Omega}\frac{1}{\mathbf{y}^\mathrm{H}\mathbf{A}_\mathrm{vac}^{-1}\mathbf{y}}} = \frac{1}{1+\frac{\mathrm{i}\Omega\cos\theta_\mathrm{i}}{2\mathcal{Z}_0}\frac{1}{-\Omega^2\mathbf{b}^\mathrm{H}\widetilde{\mathbf{c}}_\mathrm{vac}}}, \tag{C.13}$$

where $\widetilde{\mathbf{c}}_\mathrm{vac}$ corresponds to the in vacuo solution of Eq. (2.56) with the radiation impedance matrix $\boldsymbol{\Xi}$ set to zero.

Comparing this expression to the transmission factor for an unbounded limp wall with surface mass density m'' (i.e. the commonly known mass-law relationship) [61]

$$\tilde{t}_{\theta_\mathrm{i}}^{(\mathrm{W})} = \frac{1}{1+\frac{\mathrm{i}\omega\cos\theta_\mathrm{i}}{2\mathcal{Z}_0}m''}, \tag{C.14}$$

it is revealed that the term $1/(-\Omega^2\mathbf{b}^\mathrm{H}\widetilde{\mathbf{c}}_\mathrm{vac})$ in Eq. (C.13) can be interpreted as a nondimensional effective surface mass density of the MAM μ''_eff with

$$\mu''_\mathrm{eff} = \frac{m''_\mathrm{eff}}{m''_\mathrm{m}} = \frac{1}{-\Omega^2\mathbf{b}^\mathrm{H}\widetilde{\mathbf{c}}_\mathrm{vac}} \tag{C.15}$$

and

$$\tilde{t}_{\theta_\mathrm{i}} \approx \frac{1}{1+\frac{\mathrm{i}\Omega\cos\theta_\mathrm{i}}{2\mathcal{Z}_0}\mu''_\mathrm{eff}}. \tag{2.70}$$

Eq. (C.15) can be further simplified by using the Taylor series representation of $\mathbf{b}$ as given in Eq. (2.38) around $\kappa_0 = 0$. For $\kappa_0 \ll 1$, retaining only the zero- and first-order terms in the Taylor series yields the decomposition $\mathbf{b} \approx \mathbf{b}_{0^\circ} + \mathbf{b}_\mathrm{dev}$. The elements of the vector $\mathbf{b}_{0^\circ}$,

$$b_{0^\circ,mn} = \frac{2}{mn\pi^2}\left[(-1)^m - 1\right]\left[(-1)^n - 1\right], \tag{C.16}$$

correspond to the elements of the modal excitation vector under normal incidence ($\theta_\mathrm{i} = 0^\circ$) and $\mathbf{b}_\mathrm{dev}$ is the first-order deviation from $\mathbf{b}_{0^\circ}$ with

$$b_{\mathrm{dev},mn} = \frac{-2\mathrm{i}}{mn\pi^2}\left\{\kappa_\xi(-1)^m\left[(-1)^n - 1\right] + \kappa_\eta(-1)^n\left[(-1)^m - 1\right]\right\}. \tag{C.17}$$

Comparing the two equal expressions on the right side of Eq. (C.13) reveals that $\mathbf{b}^{\mathrm{H}}\widetilde{\mathbf{c}}_{\mathrm{vac}} = \mathbf{y}^{\mathrm{H}}\mathbf{A}_{\mathrm{vac}}^{-1}\mathbf{y}$. The vector $\mathbf{y}$ can be decomposed in the same way as $\mathbf{b}$ to yield, as a first order approximation, $\mathbf{y} \approx \mathbf{y}_{0^\circ} + \mathbf{y}_{\mathrm{dev}}$, with $\mathbf{y}_{0^\circ}^{\mathrm{T}} = (\mathbf{b}_{0^\circ}^{\mathrm{T}}, \mathbf{0}^{\mathrm{T}}, \mathbf{0}^{\mathrm{T}})$ and $\mathbf{y}_{\mathrm{dev}}^{\mathrm{T}} = (\mathbf{b}_{\mathrm{dev}}^{\mathrm{T}}, \mathbf{0}^{\mathrm{T}}, \mathbf{0}^{\mathrm{T}})$. Thus, $\mathbf{b}^{\mathrm{H}}\widetilde{\mathbf{c}}_{\mathrm{vac}}$ in Eq. (C.15) is given by

$$\mathbf{b}^{\mathrm{H}}\widetilde{\mathbf{c}}_{\mathrm{vac}} = \mathbf{y}^{\mathrm{H}}\mathbf{A}_{\mathrm{vac}}^{-1}\mathbf{y} \approx \left(\mathbf{y}_{0^\circ}^{\mathrm{H}} + \mathbf{y}_{\mathrm{dev}}^{\mathrm{H}}\right)\mathbf{A}_{\mathrm{vac}}^{-1}\left(\mathbf{y}_{0^\circ} + \mathbf{y}_{\mathrm{dev}}\right). \tag{C.18}$$

When expanding the products in the equation above, the symmetry of $\mathbf{A}_{\mathrm{vac}}$ (see Eq. (C.2)) yields a symmetric inverse $\mathbf{A}_{\mathrm{vac}}^{-1}$ and thus the two middle summands of the expanded product cancel each other, i.e.

$$\mathbf{y}_{0^\circ}^{\mathrm{H}}\mathbf{A}_{\mathrm{vac}}^{-1}\mathbf{y}_{\mathrm{dev}} + \mathbf{y}_{\mathrm{dev}}^{\mathrm{H}}\mathbf{A}_{\mathrm{vac}}^{-1}\mathbf{y}_{0^\circ} = \mathbf{y}_{0^\circ}^{\mathrm{T}}\mathbf{A}_{\mathrm{vac}}^{-1}\mathbf{y}_{\mathrm{dev}} - \mathbf{y}_{0^\circ}^{\mathrm{T}}\mathbf{A}_{\mathrm{vac}}^{-1}\mathbf{y}_{\mathrm{dev}} = 0. \tag{C.19}$$

Consequently, Eq. (C.18) reduces to

$$\mathbf{b}^{\mathrm{H}}\widetilde{\mathbf{c}}_{\mathrm{vac}} \approx \mathbf{y}_{0^\circ}^{\mathrm{H}}\mathbf{A}_{\mathrm{vac}}^{-1}\mathbf{y}_{0^\circ} + \mathbf{y}_{\mathrm{dev}}^{\mathrm{H}}\mathbf{A}_{\mathrm{vac}}^{-1}\mathbf{y}_{\mathrm{dev}}. \tag{C.20}$$

Finally, it is worth noting that the elements of $\mathbf{y}_{\mathrm{dev}}$ depend on κ_ξ and κ_η (see Eq. (C.17)) and thus $\mathbf{y}_{\mathrm{dev}}$ is proportional to κ_0. Therefore, the second summand in Eq. (C.20) is $\mathcal{O}(\kappa_0^2)$ and, following the first-order approximations introduced above, can be neglected for $\kappa_0 \ll 1$. Consequently, only the first summand is left so that

$$\mathbf{b}^{\mathrm{H}}\widetilde{\mathbf{c}}_{\mathrm{vac}} \approx \mathbf{y}_{0^\circ}^{\mathrm{H}}\mathbf{A}_{\mathrm{vac}}^{-1}\mathbf{y}_{0^\circ} = \mathbf{b}_{0^\circ}^{\mathrm{T}}\widetilde{\mathbf{c}}_{0^\circ,\mathrm{vac}} \tag{C.21}$$

and the low-frequency approximate form of the effective surface mass density is finally given by

$$\mu''_{\mathrm{eff}} \approx \frac{1}{-\Omega^2\mathbf{b}_{0^\circ}^{\mathrm{T}}\widetilde{\mathbf{c}}_{0^\circ,\mathrm{vac}}}. \tag{2.71}$$

D. Flanking paths in the noise shield demonstrator measurement setup

Under the assumption of a statistical distribution of sound energy within the fuselage, the following room acoustics equation can be used to estimate the average SPL inside the cabin:

$$\langle L_P \rangle_{\text{cabin}} \approx L_{W_{\text{t,tot}}} - 10\,\text{lg}\,\frac{A_{\text{cabin}}}{1\ \text{m}^2} + 6\ \text{dB}, \tag{D.1}$$

where $L_{W_{\text{t,tot}}}$ is the total sound power level transmitted into the cabin and A_{cabin} is the equivalent absorption surface inside the cabin [61]. From Eq. (D.1) and the definition of the spatially averaged noise reduction in Eq. (4.2), it follows that the noise reduction difference $\Delta\langle \text{NR} \rangle$ between two noise shield configurations is given by

$$\Delta\langle \text{NR} \rangle = \langle L_P \rangle_{\text{cabin}}^{(\text{ref})} - \langle L_P \rangle_{\text{cabin}} \approx L_{W_{\text{t,tot}}}^{(\text{ref})} - L_{W_{\text{t,tot}}} = -\Delta L_{W_{\text{t,tot}}}, \tag{D.2}$$

where it has been presumed that the excitation field is the same for both noise shield configurations and the total transmitted sound power level difference is given by

$$\Delta L_{W_{\text{t,tot}}} = 10\,\text{lg}\left(\frac{W_{\text{t,tot}}}{W_{\text{t,tot}}^{(\text{ref})}}\right). \tag{D.3}$$

Taking into account potential flanking paths, the total transmitted sound power can be decomposed into two parts as $W_{\text{t,tot}} = W_{\text{t,shield}} + W_{\text{t,fsl}}$, in which $W_{\text{t,shield}}$ and $W_{\text{t,fsl}}$ are the sound power transmitted through the area covered by the noise shield and the fuselage around the noise shield, respectively. Fig. D.1(a) provides an illustration of the different parts that constitute $W_{\text{t,tot}}$. Using Eq. (1.1), the transmitted sound powers can be expressed in terms of transmission coefficients and

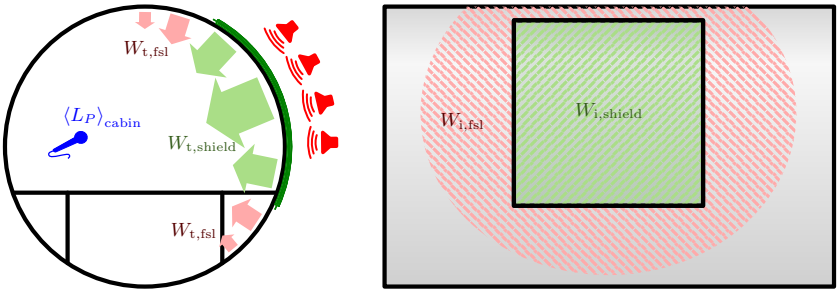

(a) Transmitted sound power. **(b)** Incident sound power.

Figure D.1: Illustration of the acoustic flanking paths around the noise shield on the fuselage.

incident sound powers and Eq. (D.3) subsequently becomes

$$\Delta L_{W_{\mathrm{t,tot}}} = 10 \lg \left(\frac{\tau W_{\mathrm{i,shield}} + \tau_{\mathrm{fsl}} W_{\mathrm{i,fsl}}}{\tau_{\mathrm{ref}} W_{\mathrm{i,shield}} + \tau_{\mathrm{fsl}} W_{\mathrm{i,fsl}}} \right). \tag{D.4}$$

As depicted in Fig. D.1(b), $W_{\mathrm{i,shield}}$ and $W_{\mathrm{i,fsl}}$ correspond to the incident sound power on the noise shield surface and the parts of the fuselage around the noise shield affected by the flanking sound paths, respectively. In Eq. (D.4) it has been assumed that the incident sound powers are equal for both noise shield configurations and that the sound transmission through the noise shield area and the surrounding fuselage area can be regarded as independent from each other. Thus, the structure-borne sound coupling between the noise shield structure and the fuselage is neglected in this case. By rearranging Eq. (D.4) and inserting it into Eq. (D.2), the following expression for the noise reduction difference is obtained:

$$\Delta \langle \mathrm{NR} \rangle \approx -10 \lg \left(\frac{Y_{\mathrm{fsl}} + \frac{\tau}{\tau_{\mathrm{ref}}}}{Y_{\mathrm{fsl}} + 1} \right), \tag{D.5}$$

with the dimensionless flanking parameter defined as $Y_{\mathrm{fsl}} = (\tau_{\mathrm{fsl}}/\tau_{\mathrm{ref}}) \cdot (W_{\mathrm{i,fsl}}/W_{\mathrm{i,shield}})$. The transmission coefficient ratio τ/τ_{ref} is related to the transmission loss difference $\Delta\mathrm{TL}$ via $\tau/\tau_{\mathrm{ref}} = 10^{-0.1\Delta\mathrm{TL}}$. Consequently, the relationship between $\Delta\langle\mathrm{NR}\rangle$ and $\Delta\mathrm{TL}$ including the influence of potential acoustic flanking paths around the noise shield is finally given by

$$\Delta\langle\mathrm{NR}\rangle \approx -10\,\mathrm{lg}\left(\frac{Y_{\mathrm{fsl}} + 10^{-0.1\Delta\mathrm{TL}}}{Y_{\mathrm{fsl}} + 1}\right). \tag{D.6}$$

This result indicates that if the flanking parameter is significantly smaller than unity and $\Delta\mathrm{TL}$ is not too large, Eq. (D.6) simplifies to $\Delta\langle\mathrm{NR}\rangle \approx \Delta\mathrm{TL}$. Thus, under these conditions, the noise reduction difference is a direct measure for the transmission loss difference between the two noise shield configurations. Since typically $\tau_{\mathrm{ref}} \lessapprox \tau_{\mathrm{fsl}}$, the condition $Y_{\mathrm{fsl}} \ll 1$ is only fulfilled when the sound power incident on the noise shield area $W_{\mathrm{i,shield}}$ is much greater than the sound power incident on the surrounding fuselage area $W_{\mathrm{i,fsl}}$. This can, for instance, be achieved by properly shielding the open side surfaces around the loudspeaker array. However, if $\Delta\mathrm{TL}$ is much greater than zero (e.g. at a MAM anti-resonance), the corresponding noise reduction difference is $\Delta\langle\mathrm{NR}\rangle \approx 10\,\mathrm{lg}(1 + 1/Y_{\mathrm{fsl}})$ (in the limit $\Delta\mathrm{TL} \to +\infty$). Therefore, the measured $\Delta\langle\mathrm{NR}\rangle$-value is capped at a maximum value which depends on the flanking parameter Y_{fsl} and is lower than the actual $\Delta\mathrm{TL}$ of the noise shields. This implies that even when the flanking incident sound power ratio $W_{\mathrm{i,fsl}}/W_{\mathrm{i,shield}}$ is comparatively low, the measured $\Delta\langle\mathrm{NR}\rangle$-value will always be lower than the actual $\Delta\mathrm{TL}$-value and this systematic error increases for larger $\Delta\mathrm{TL}$. If, on the other hand, $\Delta\mathrm{TL}$ is much smaller than zero (e.g. at a panel resonance), $\Delta\langle\mathrm{NR}\rangle \approx \Delta\mathrm{TL}$ (in the limit $\Delta\mathrm{TL} \to -\infty$) and the panel resonance is basically unaffected by the acoustic flanking paths.

In summary, this analysis shows that the noise reduction differ-

ence $\Delta\langle \mathrm{NR} \rangle$ is only under certain circumstances a direct measure for the transmission loss difference. The acoustic flanking paths introduce a systematic error which distorts the relationship between $\Delta\langle \mathrm{NR} \rangle$ and $\Delta\mathrm{TL}$ in such a way that negative $\Delta\mathrm{TL}$-values (i.e. transmission loss degradations) remain nearly unaffected. Positive $\Delta\mathrm{TL}$-values (i.e. transmission loss improvements), on the other hand, are capped at a certain maximum value.